UNIVERSITÀ DEGLI STUDI DI PALERMO

Dottorato di Ricerca in Scienze della Terra e del Mare

Dipartimento di Scienze della Terra e del Mare

Settore Scientifico Disciplinare

Redox estimates through trace elements partitioning: application on two Italian volcanoes, model comparison and overview on different geodynamic environments

Dottorando

Andrea Pellerito

Coordinatore

Prof. Marco Milazzo

Tutor

Prof. Paolo Censi

Co Tutor

Dr. Antonio Paonita

CICLO XXXIII

ANNO ACCADEMICO 2019/2020

Index

Abstract

Oxygen fugacity of Earth's mantle is one of the most debated issues of petrology. While is evident that the arc-related magmas are more oxidized than MORB and intraplate magmas, however, is not yet possible to produce a model that can uniquely determine this thermodynamic parameter for the depth of the Earth. Furthermore, there is not a clear cause that create this difference of redox conditions between volcanic products.

Recently, several experimental models based on the V partitioning between olivine and mafic melt were published and proposed as tools for investigating the redox state of mantle melts for different geodynamic environments. During this PhD we have applied different oxybarometers on natural products, including many V-fO_2 models, in order to compute the redox state of some volcanic products and compare the results obtained from different oxybarometers.

Here, we selected Mt. Etna and Ischia island in order to investigate the redox conditions of an intraplate and a subduction-related magmatism. Samples were selected from the most primitive eruptions from both volcanoes (FS eruption, for Mt. Etna and Vateliero Thepra for Ischia). Melt inclusions and relative host olivines major elements were analyzed using EMPA, while trace elements were measured using LA ICP-MS. Finally, we studied Hyblean xenoliths from literature data.

The chosen volcanic systems have been studied in the past, and our results are in good agreement with literature data. This evidence allows us to propose V-oxybarometers as strong tools for the redox computing. Moreover, the relationship between some trace element ratios and the computed redox state leads to support the hypothesis that address the cause of the different redox state of intraplate and arc primary magmas to contamination of the magmatic source. This hypothesis is in contrast with studies which address the different redox state due to magma evolution processes.

1 Introduction

The redox state of the Earth's mantle plays key roles in the magmatic processes by controlling the speciation and behaviour of multivalent elements during mantle processes [Rohrbach and Schmidt, 2011; Dasgupta et al., 2013; Stagno et al., 2013; Sifre et al., 2014], ore deposits formations [Mungall, 2002; Mungall et al., 2006; Ganino et al., 2008; Jenner et al., 2010; Zajacz et al., 2013] and when volcanic gases are driven from the mantle into the atmosphere [Holland, 2002; Edmonds, 2008; Gaillard et al., 2011; Iacono-Marziano et al., 2012a; De Moor et al., 2013; Gaillard and Scaillet, 2014; Moussallam et al., 2014; Yang et al., 2014, Gaillard et al., 2015]. Any modification of this parameter is expected to severely impact the cycles of elements such as carbon, sulfur, and oxygen [Gaillard et al., 2015, and references therein]. Oxygen fugacity (fO_2) is a thermodynamic parameter that measures the redox state, and fO_2 computation can be considered as one of the most complex issues of petrology [e.g. Carmichael, 1991; Frost, 1991; Evans, 2012].

Mantle derived magmas are mainly mid-ocean ridges basalts (MORB) and volcanic arcs basalts and is commonly considered that arc magmas are more oxidized than MORB (e.g. Christie et al., 1986; Carmichael, 1991). Many studies of the last decade tried to explain this difference in the average oxidation state of the mantle. The redox state of the portion of the Earth below the crust is strongly debated and large differences seem to exist in relation to the geodynamic context. The fO_2 of the deeper portions of Earth's mantle is computed from mantle xenoliths recovered from the continental lithospheric mantle, which suggest reduced conditions with increasing depth [e.g. Woodland et al., 2003; Yaxley et al., 2012; Stagno et al., 2013], due to high stability of Fe^{3+}-bearing garnet (skiagite) component with increasing depth. Computed redox state of continental lithosphere range between QFM-4.25 to QFM+1 with an average redox at QFM-0.7/-1 [Foley, 2011, and references therein], also achieved by quantitative studies of the active redox materials transferred during subduction [Lecuyer and Ricard, 1999; Foley, 2011; Evans, 2012], taking into account that oxygen-rich rocks must be introduced in the deep mantle to trigger deep redox heterogeneities.

On the other hand, it is not clear how 2 Ga years of subduction, melting, metasomatism, and other long-standing processes can have triggered large geochemical heterogeneities, as oxidation depletion or enrichment of the mantle [Gaillard et al, 2015]. The redox conditions in mantle portions characterized by active dynamics could then be very different from the above ones, and in the following, we resume studies and results for the main geodynamic conditions on Earth.

Several methods have been developed to estimate the redox conditions of igneous products and their sources. The first effective methods for redox estimates are the mineral oxybarometers. The mineral oxybarometers are mainly based on iron valence states (Fe^{2+} and Fe^{3+}), such as the Olivine-Opx-Spinel for asthenospheric products [e.g. Ballhaus, 1993; Ballhaus et al., 1990; Parkinson and Arculus, 1999; Evans et al., 2012] or Garnet-Olivine-Opx for garnet-bearing rocks, which originate at higher depths [Stagno et

al., 2013]. These mineral systems involve fO_2 in equilibrium of iron-bearing phases, such as the Eq.1 for Garnet-Olivine-Opx equilibrium:

Eq.1 $$2\ Fe_3Fe_2^{3+}Si_3O_{12} \rightleftarrows 4\ Fe_2SiO_4 + 2\ FeSiO_3 + O_2$$

in which the iron garnet (skiagite), according to a disproportion reaction, produces olivine (fayalite), opx (ferrosilite), and O_2. Previous to a precise determination of the ratio of Fe^{3+} to total Fe ($Fe^{3+}/\Sigma Fe$) in garnet, this equilibrium has been used to determine fO_2 and therefore the redox state of deep mantle xenoliths.

For fO_2 determination, other methods based on $Fe^{3+}/\Sigma Fe$ ratios were investigated. Melt inclusions hosted within olivine, considered as the entrapped primitive melt during olivine growth could record the redox state. $Fe^{3+}/\Sigma Fe$ can be obtained in these materials with precise analytical techniques such as XANES, [e.g. Brounce et al., 2014, 2015; Cottrell and Kelley, 2011; Kelley and Cottrell, 2009, 2012] and then used for redox determination.

Iron is not the only element with variable oxidation states and then redox-sensitive during mantle melting. Other minors and trace elements were investigated to be useful to effectively estimate the redox state of the magmatic source. Redox-controlled partitioning processes occur also on other metals, such as V. V oxidation state may vary from V^{2+} to V^{5+} [e.g. Canil, 1999; Gaetani and Grove, 1997], allowing V to be a great candidate for redox assessment. V behaviour during partitioning processes has been extensively studied and many published vanadium partitioning coefficients (D_V) models were obtained from petrological experiments. A lot of experiments, performed at different pressure and redox conditions [Canil, 1997, 1999; Canil and Fedortchouk, 2000; Davis et al., Laubier et al., 2014; Mallmann and O'Neill, 2009, 2013; Papike et al., 2013; Shishkina et al., 2018; Wang et al., 2019], were used to empirically linking V partitioning to fO_2. Many other theoretical and empirical correlations to obtain a fO_2 constrain, were recently published, such as Zn/Fe [Lee et al., 2010], V/Yb [Laubier et al., 2014].

In this study, olivine hosted melt inclusions (MIs) were selected from natural products of two different Italian volcanoes. MIs are small drops of silicate melt, entrapped in minerals during their formation in the depths of the magmatic systems. Formed inclusions are isolated by the hosting crystal that prevents degassing processes [Schiano, 2003]. Since primitive information of depth magma is commonly lost during the magma ascent in the volcanic systems, thus, the MIs hosted within olivine are the best tool to study the magma in its most primitive conditions. To better understand redox state over a wide region, and to compare different environments, the chosen volcanic systems were Mt. Etna and Ischia island. While Mt. Etna is a complex intraplate magmatic system characterized by different eruptive styles and various composition of erupted products, and in which magmatic redox condition are debated, Ischia island is a poorly studied subduction-related system. Besides, we coupled the investigation of xenolithes from Hyblean volcanism, southward Mt Etna, as these display clear mantle origin. We selected the most primitive eruptions for both volcanoes; FS eruption, a 4 ky ago product erupted

from Mt. Etna, and Vateliero eruption, which is one of the latest eruption of Ischia (6th and 4th centuries BC). In accurately selected olivine MIs, many oxybarometers were applied on these samples. Different V-oxybarometers [Mallmann and O'Neill, 2013; Shishkina et al., 2018; Wang et al., 2019], calibrated on different kind of experimental melts, were used to estimate redox state of the samples. The Zn/Fe and FeTiMM oxybarometers [Lee et al., 2010 and Arató et Audétat, 2017, respectively] were also applied.

The redox estimates obtained from the different models were compared with each other and with the previously published data. Our results show to be in agreement with the literature and reveal the oxidized character of both these volcanoes, although Ischia volcanism is even more oxidized with respect to Mt Etna. Moreover, a geochemical analysis of the trace elements, in particular of the relationship between fluid-mobile elements and fluid-immobile elements, shows that Etnean and Ischia mantle sources have been both oxidized by the contribution of metasomatic fluids, although these fluids acting in different geodynamical contexts seem to display clearly different signatures. Inferences and speculations about the origin and nature of the two metasomatisms are discussed.

2 Overview on the redox state of the mantle

2.1 MORB mantle

Although continental lithospheric mantle is suggested to be reduced (average redox at QFM-0.7/-1), this redox model may not apply, for many observations, to the convective mantle which generates MORB melts. The first reason is given by kimberlitic magmas. Kimberlite is highly oxidized and CO_2 rich magmas, which are generated deep in the mantle and during migration through overlying cratons, picking up diamonds. This implies that there are regions in the mantle, deeper then continental lithospheric mantle, more oxidized than the overlying part [Yaxley et al., 2017; Dasgupta, 2018]. Furthermore, carbonate inclusions occur within deep mantle diamonds [Brenker et al., 2007; Stagno et al., 2015] and garnet inclusions in diamonds from the mantle transition zone are more oxidized than predicted by the Fe-controlled fO_2 profile inferred from redox models of continental lithospheric mantle constrained by mantle xenoliths [Kiseeva et al., 2018]. Moreover, deeply generated komatiites have a similar redox state to MORB [Gaillard et al., 2015, and references therein]. Last but not least, recent evidence from CO_2 and trace element enrichment observed in undegassed oceanic basalts [Eguchi et al., 2018], shows the important contribution from the recycled crust on the redox state. In this scenario, in which the carbonate-diamond transition is taken into account, the *f*O2 of the peridotitic mantle should be in the carbonate stability field, which is higher compared to eclogite/pyroxenite continental lithosphere [Luth, 1993] (Fig. 1). The resulting redox state of MORB-parent mantle is significantly oxidized compared to the continental lithospheric mantle, which ranges between QFM and QFM+1 [Evans et al., 2012].

Fig. 1. Pressure vs computed fO_2 for the continental lithospheric mantle xenoliths and the convective mantle (MORB source). DCDG/D is the graphite/diamond transition in eclogite/pyroxenite rocks [Luth, 1993]. EMOG/D is the graphite/diamond transition in peridotite. [Eguchi et al., 2018]

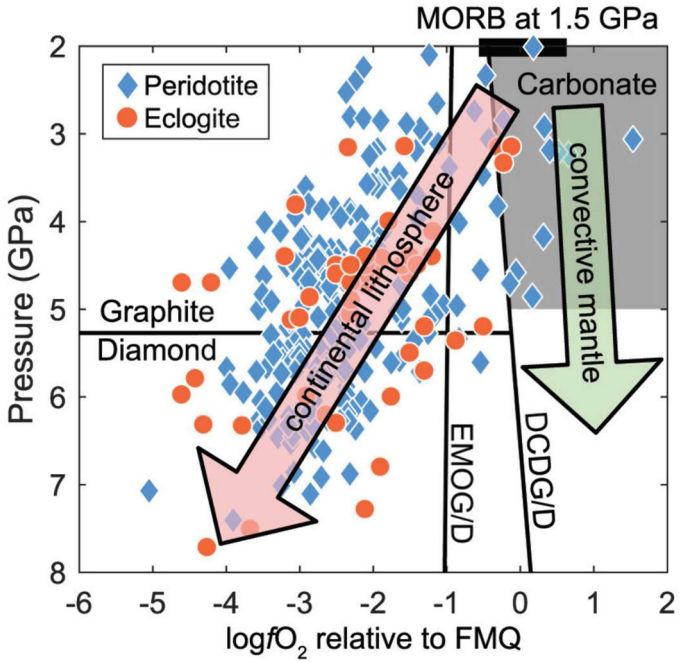

2.2 Arc mantle

While it is clear that the mantle redox heterogeneity makes it difficult to associate a specific redox state to a geodynamic environment, it is accepted that arc-magmas are more oxidized mantle products than MORB. Calculated fO_2 of arc basalts is between QFM+2 and QFM+4, where high-K arc samples show a higher average oxidation state (QFM+ 2.9 ± 0.7) than lower K arc samples (QFM+2.1 ± 0.6). But many studies arguing about the nature of the redox conditions of the source of these products.

Some study proposes a primary oxidized mantle. The spinel-olivine oxybarometer [Ballhaus et al., 1991] applied to primitive olivine (Fo>85 mol %) hosted spinel pair in basalts from volcanic arcs show that sub-arc mantle is 1-4 log units more oxidized than the MORB source [Evans et al., 2012]. This oxidation features can be supported by oxidizing processes which occur in the mantle. The oxidized nature of the mantle may come from peculiar melting conditions in the mantle wedge [e.g. Ballhaus, 1993; Ballhaus and Frost, 1994; Brandon and Draper, 1996; Parkinson and Arculus, 1999]. The ocean crust is hydrothermally altered in a process known as “seafloor weathering” and the hydrated ocean crust is also considered the main source of fluids during subduction dehydration processes. These H_2O-dominated fluids can lower the solidus of the overlying mantle wedge, which then can melt to produce basaltic primary arc magmas. The fluxes of volatile-rich fluids from the subducted slab control the oxidized signature due to this crustal fluid assimilation [Parkinson and Arculus, 1999; Kelley and Cottrell, 2009; Lee et al., 2010].

Other processes to take into account is the deep burial of serpentinite and eclogite, which increase the mantle fO_2 by increasing the $Fe3+/\Sigma Fe_{tot}$ ratio because ocean floor serpentine shows a $Fe3+/\Sigma Fe_{tot}$ ratio much more elevated than the average mantle value [O'Neill et al., 1993; Cottrell and Kelley, 2011; Stagno et al., 2013]. Based on modern subduction rates [Li and Lee, 2006] and assuming an average degree of serpentinization of the oceanic lithosphere [Schmidt and Poli, 1998; Li and Lee, 2006] the average amount of Fe_2O_3 buried in the mantle due to the serpentinite subduction range between 5 to 20 × 10^{14} g/year. Dehydrated eclogites also show high $Fe3+/\Sigma Fe_{tot}$, resulting in an annual flux of Fe_2O_3 between 6 to 11 × 10^{14} g/year [Lecuyer and Ricard, 1999]. Taking into account that part of the buried Fe^{3+} in subduction zones is returned via arc-volcanoes, and considering that 20 × 10^{14} g/year gram of Fe_2O_3 is buried into the deep mantle, fO_2 should have significantly increased from the primordial reduced mantle (ca from QFM−3 to QFM) [Gaillard et al., 2015, and reference therein]. Subduction is then an oxygen source for the deep mantle, in a process that is counteracted by the paired sulphides subduction, which sulfur is oxidized into SO_2 and SO_3 upon dehydration and melting. Sulfur oxidation leads to an oxygen loss from the deep mantle [Alt et al., 2012; Debret et al., 2014], which can cause a lowering from 50% to 30% of $Fe3+/\Sigma Fe_{tot}$ ratio, as reported in chemical analyses on exhumed serpentinites [Padron-Navarta et al., 2011]. In summary, the overall result of sulfur subduction is an oxygen source for the deep mantle [Evans et al., 2012; Gaillard et al., 2015].

On the contrary, many studies support a different hypothesis on the arc mantle redox state. Garnet-bearing and plagioclase-free xenoliths from the trachy-andesitic volcanic centre on the margin of Colorado Plateau in Arizona shows unique characteristics [Erdman et al., 2016; Tang et al., 2018]. This rock with Mg# ranging from 0.5 to 0.82, which plagioclase absence makes an ideal product for Eu systematics, was interpreted as representing a cumulate from primitive arc magmas. Eu occurs in two different valent states, Eu^{2+} and Eu^{3+}, and their ratio is sensitive to fO_2. The geochemical behaviour of both Eu^{2+} and Eu^{3+} can be well constrained throughout magmatic differentiation and it can be a robust oxybarometer in plagioclase-free rocks [Burnham et al., 2015]. Eu anomalies are expressed as Eu/Eu*, where Eu* represents the hypothetical concentration of Eu if it behaved only like Eu^{3+}. Eu/Eu* allows us to calculate the Eu valence state and to place an upper bound on the fO_2 of magma. For primitive magmas, Eu/Eu* should be 1 [Tang et al., 2017]. Cpx and garnet commonly show increasing positive anomalies with decreasing Mg#, consistent with Eu^{2+} is more incompatible than Eu^{3+}. Eu anomalies of the cpx and garnets, within the most primitive arc cumulates, imply QFM-1 ±1 and QFM-1 ±0.5 respectively, identical to within error that inferred from MORB. These observations suggest that the oxidation state of the sub-arc mantle may not be significantly different from the MORB mantle and that the oxidized signature of arc magmas may be acquired during ascent and differentiation.

This hypothesis is supported by other studies on the peculiar iron depletion of arc-lavas. Iron depletion has been attributed to early Fe_3O_4 fractionation, but this process would be suppressed in reduced conditions [Berndt et al., 2004] and lavas should follow the iron enrichment path of tholeiitic series. An intracrustal process may then deplete Fe and oxidize the residual melt. Immature arcs are predominantly tholeiitic (with Fe enrichment) whereas continental arcs are calk-alkaline, and this shows a correlation with crustal thickness, which is evident in FeO_T-MgO plot of global arcs (Fig. 2).

Fig. 2. FeO_T vs MgO systematics in the arc and mid-ocean ridge (MOR) magmas. Tholeiitic differentiation is represented by the MOR series. Arc samples are divided into three categories based on the thickness range of the above crust. Arc magmas composition range from tholeiitic to calc-alkaline [Tang et al., 2018].

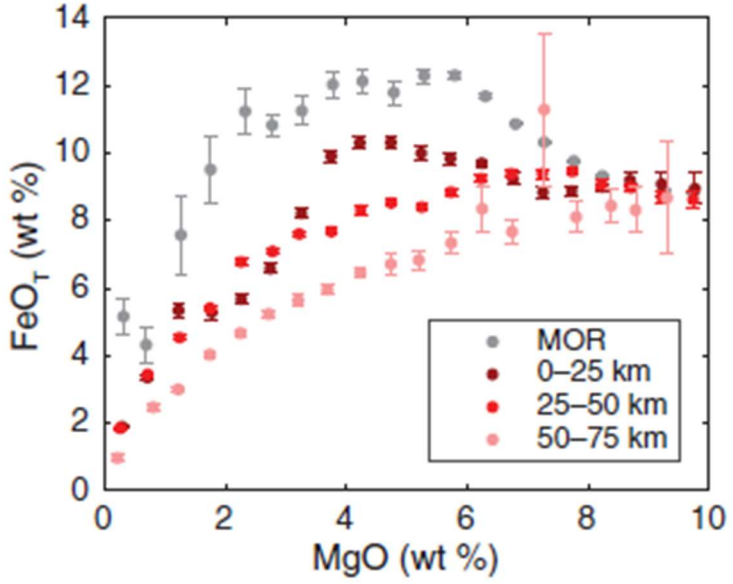

If crystallization processes are a pressure-depending trend, the crustal thickness controls the differentiation, therefore it can influence the magmatic evolution of the redox state by increasing the $Fe^{3+}/\Sigma Fe$ ratio [Tang et al., 2018]. Performed pMELTS models, simulating crystal fractionation of a hydrous basaltic melt at pressures between 0.2 to 2.0 GPa, corresponding to the common thickness of tholeiitic island arc (near 20 km) to calc-alkaline continental arcs (50-80km), respectively, shows how at low-pressure Fe is poorly compatible in olivine and cpx, and strongly incompatible in plg, thus crystallization leads to iron enrichment. At higher pressure, crystallization of garnet is the most efficient processes which remove iron from the system (Fig. 21a). The garnet crystals fractionation can increase the oxidation state during cumulates forming by removing up to 50% of initial Fe [Alonso-Perez et al., 2009] and drive the Fe depletion characterizing calc-alkaline series differentiation [Green, 1972; Green and Ringwood, 1968]. The effect of garnet fractionation control iron depletion of arc magmas and it correlates with Dy/Yb ratios. During Fe-bearing crystals crystallization, while oxides do not change this ratio, garnet crystallization incorporates Yb, thus raising the ratio [Rudnick et al., 1986]. Amphiboles crystallization, on the other hand, would low Dy/Yb coupled with iron depletion [Davidson et al., 2007] (Fig. 3b). Since garnets have an extremely low Fe^{3+}/FeO_T, when garnet abundance removes over 40% of the total Fe, the magma can be progressively oxidized from QFM-1 to at least QFM+1, consistent with Eu/Eu* data [Tang et al., 2018].

Fig. 3. Iron depletion in arc magmas can be constrained from FeO_T/MgO ratio in magmas. a) pMELTS simulation of hydrous basalt crystal fractionation which reports the percentage of initial Fe removed by crystal fractionation. At high-pressure garnet crystallization is leads to remove the most of iron b) the iron depletion is plotted against $[Dy/Yb]_N$, where the subscript N means chondrite-normalized. It shows that iron depletion in arc magmas is related to garnet fractionation, which increases the Dy/Yb ratio. If iron depletion would be caused by oxides or amphiboles fractionation, these would lead to different trends. [Tang et al., 2018]

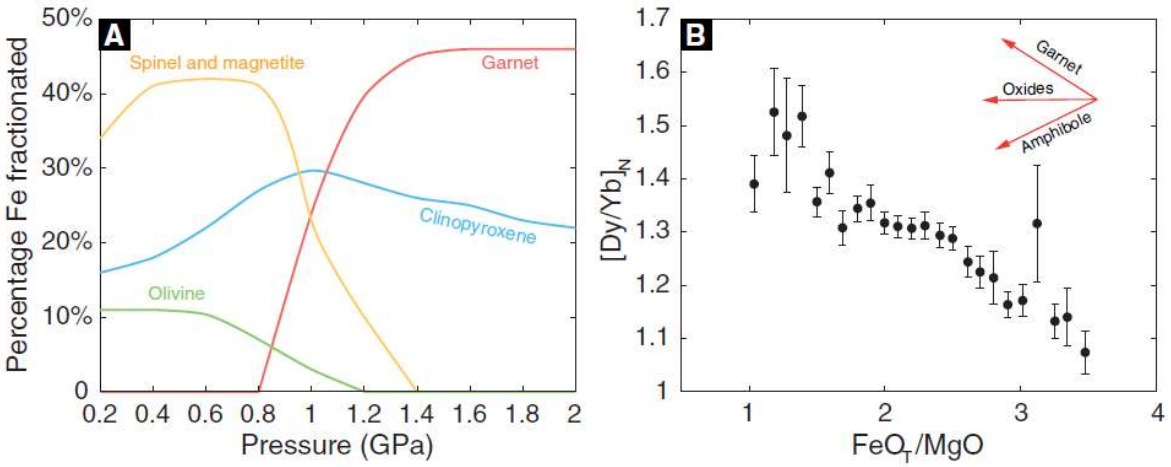

Broadly speaking, garnet fractionation is possible at high-pressure conditions, leading to simultaneous Fe depletion and oxidation of residual melts, resulting to produce the commonly calc-alkaline lavas associated with the thickened crust. Magnetite saturation occurs only after the magma is significantly oxidized from the garnet fractionation

process; thus, magnetite fractionation cannot be considered the main process of Fe depletion of arc magmas. Coupled garnet and magnetite fractionation, can finally work to increase redox state of residual melts above QFM+1.On the other hand, Fe^{3+} depleted garnets of cumulates can go back in the mantle due to their high densities, so as to produce a progressive crustal growth leads to a flux of reduced materials into the mantle [Jagoutz et al., 2013]. The oxidized continental crust results in a gravity-driven redox filter, which may have influenced Earth's redox evolution by limiting the output of ferrous Fe and sulphides [Tang et al., 2018].

Other studies explain the oxidized redox feature of arc magmas, suggesting that it can be acquired during magma ascent to the surface due to differentiation and degassing processes [e.g. Lee et al., 2010, 2012]. The possibility of secondary oxidization processes is supported from many geochemical approaches based on redox-sensitive ratios, such as Zn/Fe, V/Sc, D_V, and Cu systematic in basalts [Mallmann and O'Neill, 2009; Lee et al, 2010, 2012; Wang et al., 2019], which leads to considering that primary arc products are not significantly more oxidized than other basalts from the mid-ocean ridge or intraplate magmatism.

Therefore, the direct information of redox state of the mantle wedge melting region is unknown due to the inaccessibility of "primordial" mantle wedge xenoliths, which even if ever exhumed, are often serpentinized or altered from other processes.

In contrast to the hypothesis of similar redox condition for MORB and arc mantle, an even more opposite hypothesis is supported by recent studies, which describe a reduced arc mantle.

Yushigou harzburgite is an unusual fresh harzburgite, well distinguished from the serpentinized oceanic lithospheric mantle, and in spatial association with arc volcanic and subduction zone complexes [Song et al., 2009]. Petrological and geochemical observations allow us to consider this harzburgite as a remnant of a fossil mantle wedge, exhumed during the Caledonian Qilian Orogeny continental collision. Different types of fluid inclusions within this harzburgite were interpreted as resulting from within-crystal redistribution to sub-solidus deformation [Song and Su, 1998] In situ analyzed fluid inclusions by laser Raman micro-spectroscopy [Burke, 2001], show strong peaks of liquid CH_4 as the dominated phase in all the round inclusions with high liquid/vapour ratios, methane and graphite in tubular fluid inclusions and methane and minor graphite within vapour dominated fluid [Song et al., 2009]. No oxidized forms of fluids, such as CO_2, CO, or SO_2, have been detected in any of these fluid inclusions from the harzburgite studied samples. Carbon isotope range from -12.5‰ to -29.5‰, which is far too negative to be asthenospheric values, but consistent with sediment origin. Data interpretation suggest that Yushigou harzburgite is a residue of high-degree melting in a mantle wedge environment in which this depleted residue recorded fluids from subducting oceanic lithosphere fluid [Song et al., 2009].

2.3 Intraplate mantle

The redox state of intraplate magmatism is generally considered as intermediate between the most reduced MORB and the most oxidized arc magmatism (Fig. 4a) [Evans et al., 2012]. But, as shown in Fig. 4a and Fig. 4b, in some cases OIB fO_2 can be high, overlapping the redox range of arc products. To better explore the reasons for this high redox state for intraplate magmatism, the French Massif Central (FMC) is an important example of oxidized intraplate magmatism. FMC represents a current intraplate volcanism region, with a higher oxygen fugacity than average intraplate continental lithosphere [Martin et al., 2017]. This higher oxidation may be caused by small-scale metasomatic processes, such as volatile-rich melt migration in the mantle, which can modify the chemistry of the surrounding mantle. Therefore, the average fO_2 of the mantle can substantially increase in highly metasomatized mantle regions. In order to constrain the oxidation origin below FMC, olivine-opx-spinel equilibrium models [Bryndzia et al., 1990; Ballhaus et al., 1991; Sack and Ghiorso, 1991] and XANES analyses on cpx, were applied on lherzolite/harzburgite xenoliths within FMC products, containing olivine, opx, cpx, spinels, and occasionally phlogopite, apatite, amphibole, and sulfide. Melt inclusions observed in xenoliths contain between 4% to 8% K_2O (wt.%), indicating that they formed deeper where phlogopite was present. Thermobarometry indicates that the temperature of the metasomatic melt was about 1115 °C while the surrounding mantle temperature was 950-1060 °C. Oliv-opx-spinel oxybarometer gives a high oxidation state, up to QFM+1.6, on harzburgite samples and metasomatized samples give. This high oxidation state is linked with the K_2O, H_2O, and CO_2 contents in the FMC magmas, which derive from potassium and carbon-rich sediments. Volatile-rich fluid metasomatized the mantle wedge, crystallizing phlogopite, amphibole, and carbonates and rising the fO_2.

The presence of volatiles in the intraplate mantle, worldwide distributed, can be related to the occurrence of ancient subduction processes and subsequent mantle metasomatism. Melting of the preserved metasomatized lithospheric mantle at intraplate conditions produce volatile-rich magmas, that have the potential to increase the upper lithospheric mantle fO_2 to very high values [Martin et al., 2017]. Moreover, the oxidative capacity of metasomatic events observed in a variety of settings (intraplate to subduction regions) may well be connected to sulphate-rich fluids, including in the mantle wedge [Gaillard et al., 2015].

The redox state assessment can be also performed by MnO systematic, due to MnO behaviour which is very similar to FeO. Mn-bearing minerals (tephroite Mn_2SiO_4 and hausmannite Mn_3O_4) occurs at significantly higher fO_2 than for natural systems, thus Mn^{2+}/Fe^{2+} ratios increase in olivine with increasing fO_2. Therefore, olivine from more oxidized magmas should display higher MnO/FeO ratios than those from magmas that formed at reduced conditions. MnO/FeO ratio of olivines versus the redox state for MORB and OIB is shown in Fig. 22b. MORB and arc olivines show a clear correlation to redox, while OIB olivine is not on the trend and this feature may be related to the mantle source mineralogy [Sobolev et al., 2007; Evans et al., 2012, and reference therein].

Fig. 4. a) Oxidation state of basalts versus Fo content of olivine within basalts. The calculation performed using Ballhaus et al., 1991, oxybarometer. Black circle: MORB; triangles: boninite; squares: OIB; white circle: low-K arc magmas; grey circles: high-K arc magmas. b) Average Mn/Fo ratio of olivine sample versus average calculated redox state. [Evans et al., 2012]

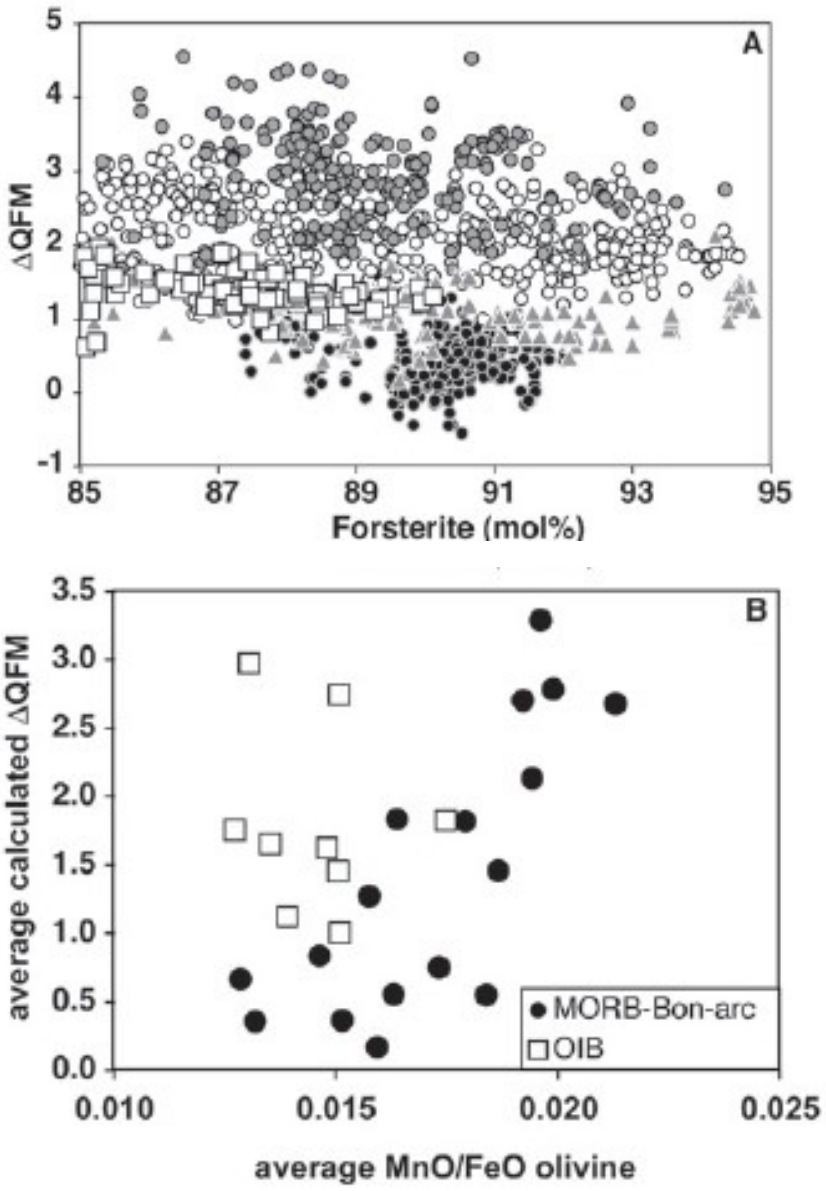

3 Redox estimation models

The redox state of a system, measured by fO_2, is an important thermodynamic parameter. It allows to balance redox reactions and calculate the valence state speciation of redox-sensitive elements, such as Fe [Kilinc et al., 1983; Kress and Carmichael, 1991; Moretti, 2005] and V [Canil, 1997, 2002; Shearer et al., 2006; Mallmann and O'Neill, 2009], and many species in volcanic gases (i.e. H_2S and SO_2) [Wood et al 1990]. The fO_2 estimation is one of the most complex issues of petrology. Its thermodynamic calculation involves complex balances and equilibrium reactions and we must always take into account that natural systems are subjected to constant changes and theoretical equilibrium is hardly achieved. As concerns its experimental measurement in natural samples, a lot of scientific literature aims to produce calibrated methods, to constrain the redox state of MIs and rocks paragenesis. The following methods are those we applied during this Ph.D. study.

3.1 Mallmann and O'Neill, (2013) (MON13)

The MON13 oxybarometer is based on V partitioning between olivine and silicate melt. This oxybarometer was calibrated on several mixtures of basaltic compositions for a large range of redox conditions between four log_{10} units above and below the QFM oxygen buffer. Three starting compositions and several derived compositions were used. The first composition used, named DFA, was based on the intersection of the forsterite primary crystallization volume with the 1400°C isotherm in the subsystem Mg_2SiO_4-$Mg_2Si_2O_6$-$CaMgSi_2O_6$ [Evans et al., 2008]. From DFA, seven daughter compositions were produced by adding variable amounts of Al_2O_3, and the other seven compositions were produced by adding variable amounts of fayalite (Fe_2SiO_4). The second main composition was based on that of mid-ocean ridge basalts. Daughter compositions were produced by adding variable amounts of ferric olivine, from Fo_{100} to Fo_{40}. The third starting composition was based on the komatiite flow from Alexo (Canada). This last composition allowed us to investigate the olivine-melt partitioning in a high temperature system. The experiments were carried out in different pressure conditions, to assess the effect of pressure on the trace element partitioning between olivine and melt. Oxygen fugacity was set by the graphite-carbon dioxide (GCO) oxygen buffer, according to the reaction $C+O_2=CO_2$.

The experimental charges were analyzed by electron microprobe and LA ICP-MS, respectively for major and trace elements. The results indicate that V becomes progressively more incompatible in olivine with increasing redox state, which was imposed by experimental oxygen fugacity. After performing stepwise regressions, including major elements composition of melt as parameters, authors obtained the model shown in Eq.2.

Eq.2 $$\Delta QFM = -7.7 - \left(\frac{log_{10} D_V^{\frac{ol}{melt}}}{0.2639}\right) - \left\{\frac{\begin{matrix}822-3328\cdot\left(1-Mg_{\#}^{ol}\right)^2+532\ \cdot X_{KO_{0.5}}^{melt} \\ +746\cdot\left(X_{CaO}^{melt}+X_{NaO_{0.5}}^{melt}\right)-325\ \cdot\left(X_{SiO_2}^{melt}+X_{AlO_{1.5}}^{melt}\right)\end{matrix}}{0.2639\cdot T}\right\}$$

Where T is the temperature (K), $Mg_{\#}^{ol}$ is the molar fraction of MgO referred to MgO-FeO in the olivine, and X_i^{melt} is the molar fraction of the *i*-oxide in the melt. T can be obtained from literature or calculated.

Fig. 5. The effect of oxygen fugacity on the partitioning of V between olivine and silicate melt for MON13 experiments. Moreover, many previous published experiments are plotted in the figure [Mallmann and O' Neill, 2013].

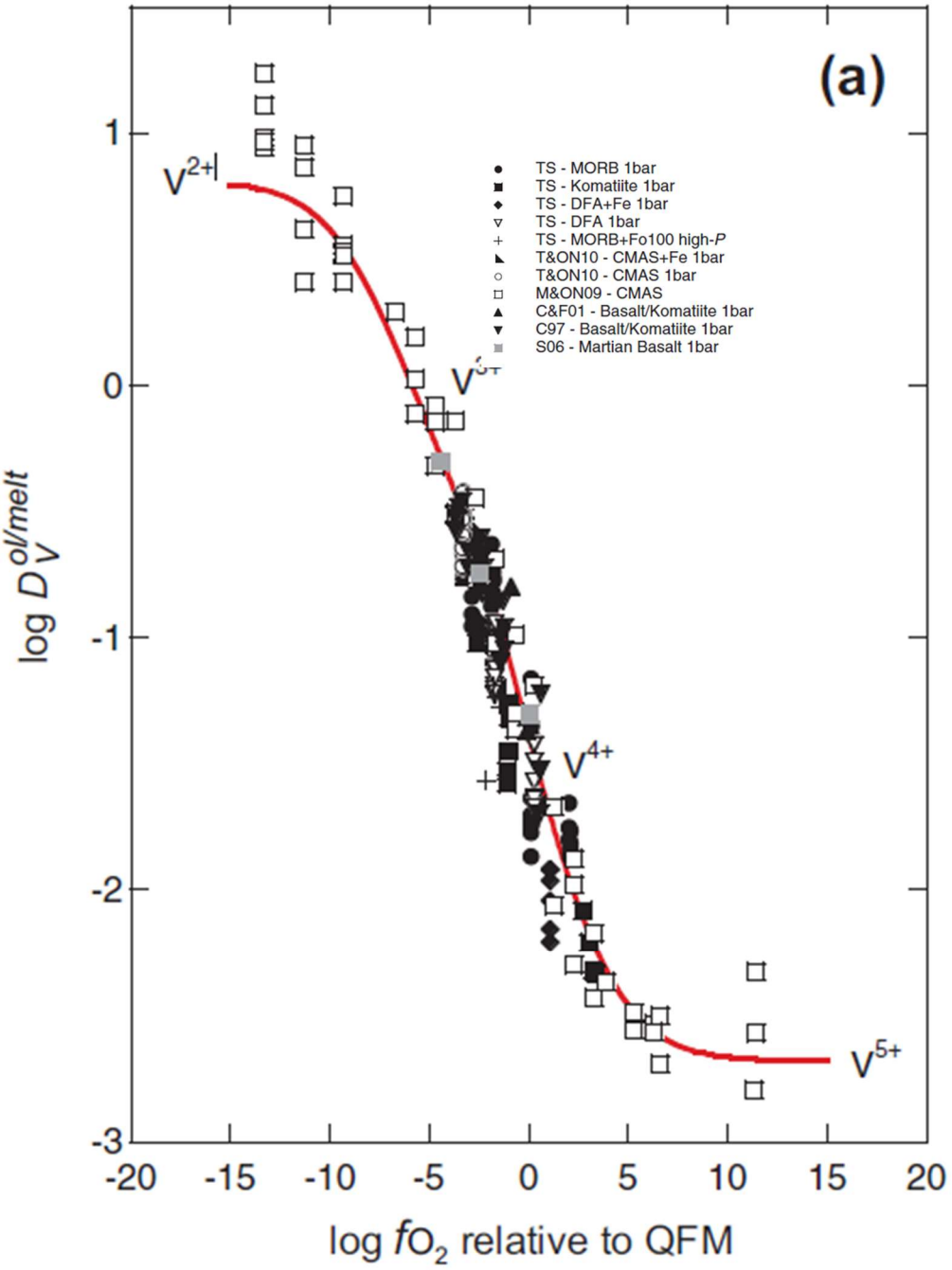

3.2. Wang et al., (2019) (WANG19)

WANG19 model was produced to determine the V, Ti, and Sc partition coefficients between the melt phase and the host mineral for arc basalts. The experiments, performed by piston-cylinder apparatus, were performed at typical arc P-T-H_2O conditions and variable fO_2. Three starting materials were produced from synthetic high MgO basalt and synthetic peridotite. The synthetic basalt was prepared by mixing major oxide and alkali-carbonates and doping the mixture with the first-row transition elements, REEs, LILE, and Cs. The synthetic peridotite was produced by a synthesized glass equal to MgO-subtracted KLB-1 peridotite and adding MgO into the Mg-free glass. The three samples are mixtures of the high MgO basalt and KLB-1 peridotite compositions at ratios of 1:0, 4.7:1, and 2.5:1. fO_2 was set by using gold-palladium alloy capsules with variable iron content, which produced variable fO_2 values during experiments. Iron-free alloys were used to produce oxidized conditions, while iron-bearing alloy capsules were used to produce reduced conditions and also minimize the Fe-loss at reduced conditions. The experimental products were analyzed by electron microprobe for major elements and by LA ICP-MS for trace elements.

Fig. 6. Experiment results from Wang et al., (2019) plotted with other literature data.

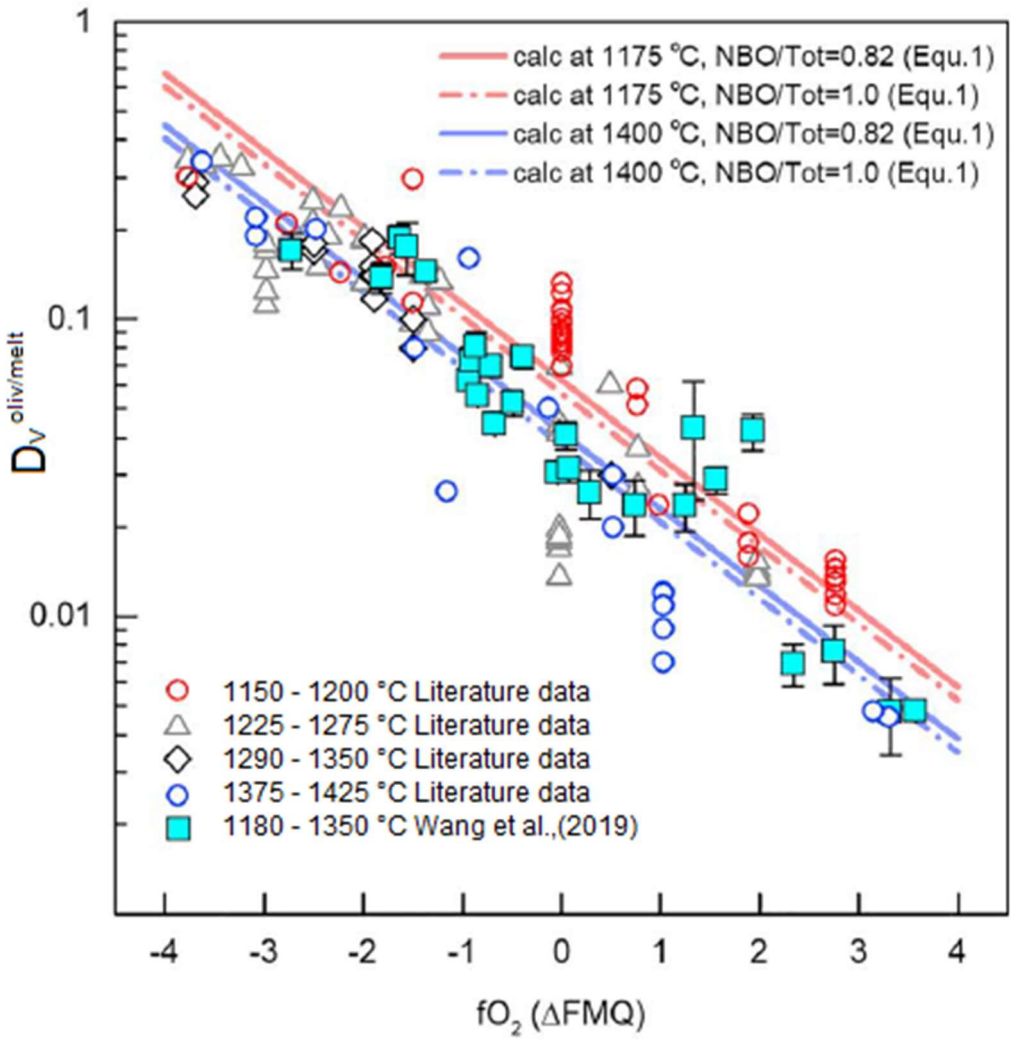

The obtained model, shown in Eq.3, takes into account the temperature T (K) and NBO. NBO is non-bridging oxygen and NBO/Tot refers to a melt polymerization degree [Mysen, 2014] defined by Eq.4.

Eq.3

$$log\left(D_V^{\frac{oliv}{melt}}\right) = -2.30(\pm 0.28) - 0.258(\pm 0.006)\Delta QFM + \frac{1871(\pm 398)}{T} - 0.24(\pm 0.03)\frac{NBO}{Tot}$$

Eq.4

$$NBO/_{Tot} = (4X_T - 2X_O)/_{X_T}$$

where X_T and X_O respectively are the atomic proportions of tetrahedrally coordinated cations and oxygen.

3.3 Shishkina et al., (2018) (SHI18)

The proposed oxybarometer applies to the hydrous island-arc magmas at relatively low temperatures. Redox model was derived from crystallization experiments performed with two different samples from subduction-related Mutnovsky volcano in the Southern Kamchatka:

- a high-Al, low K basalt (sample N72), namely the most primitive composition of the Mutnovsky volcano.
- the lava of the latest Mutnovsky volcano activity.

The rocks were powdered and melted in a platinum crucible, then quenched. The produced glass was crushed into small pieces and melted again with subsequent quenching to glass. Experiments were performed in Au capsule (T < 1050 °C) or $Au_{80}Pd_{20}$ (higher temperature experiments), in both water-undersaturated and water-saturated conditions, with a variable amount of silver oxalate to produce CO_2. The redox conditions were controlled by using different Ar-H_2 mixture with water and carbon dioxide proportion within the capsules.

Major element concentration in glassy melt-inclusion and mineral phases of experimental products was determined with the electron microprobe, while the concentration of V in glasses and olivine was measured by using LA ICP-MS. Water concentration within melt inclusions was estimated by secondary ion mass spectrometry (SIMS) and Fourier-transform infrared spectroscopy (FTIR).

The estimated partition coefficients for Mutnovsky basalt shows a strong negative correlation with ΔQFM, consistent with previously published results and olivine-spinel equilibrium. The correlation for these experiments can be fitted by the following equation.

Eq.6 $$\Delta QFM = -3.26^{+0.47}_{-0.52} \log D_V^{Oliv/melt} - 3.73^{+0.75}_{-0.85}$$

Fig. 7. Experiments results from Shishkina et al., (2018) plotted with other literature data.

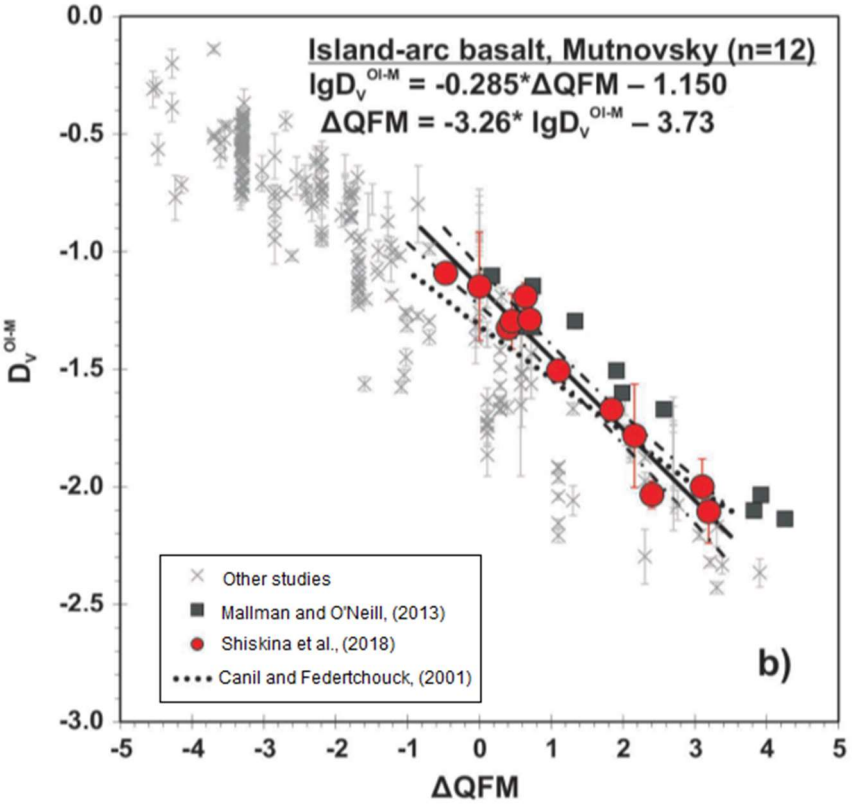

3.4 Lee et al., (2010)

Zn/Fe_T is proposed as a redox tracer of magma source. Over the magmatic source fO_2 range, Fe occurs in two valence states, whereas Zn occurs only as Zn^{2+}. Since Zn^{2+} and Fe^{2+} behaviour is similar (Zn^{2+} and Fe^{2+} ionic radius is respectively 0.74 Å and 0.70 Å) Zn/Fe^{2+} ratio is not fractionated significantly between olivine, orthopyroxene, and basaltic melt [Le Roux et al., 2010]. At low fO_2, which means low Fe^{3+}/Fe_T (≈0.1), peridotite melting and olivine crystallization do not modify Zn/Fe_T ratio, explaining why MORBs and peridotites have identical Zn/Fe_T ratio. At high fO_2, and then high Fe^{3+}/Fe_T, Zn/Fe_T is expected to fractionate due to Fe^{3+} incompatibilities in olivine and orthopyroxene respect to Zn^{2+}. Due to these considerations, the authors derived the following equation which allows determining the Fe^{3+}/Fe_T ratio:

Eq.7 $$\frac{Fe^{3+}}{Fe_T} \approx 1 - \frac{\left(Zn/Fe_T\right)_{melt}}{\left(Zn/Fe_T\right)_{peridotite}}$$

Where Zn/Fe_T in peridotites can be taken as a constant ($9\pm1\cdot10^{-4}$) [Le Roux et al., 2010]. Obtained Fe^{3+}/Fe_T can subsequently be converted into $\log(fO_2)$, using the equations of Kress and Carmichael, 1991.

3.5 Arató et Audétat (2017)

The oxybarometer FeTiMM is based on the partitioning of Fe and Ti between magnetite and silicate melt. The first set of 50 experiments were conducted in the system magnetite-H_2O-rhyolite melt at various fO_2 ranges, temperatures, pressures, magnetite composition, and ASI (defined as the molar Al_2O_3/ (Na_2O + K_2O + CaO) ratio). The result, shown in Fig. 8, shows that the Fe-Ti exchange coefficient between magnetite and silicate melt, defined in Eq.8, prevalently strongly depends on fO_2, with the negligible effect of temperature. The second set of 59 experiments was focused on the ilmenite-saturated system. To account for the large range of melt compositions it was necessary to include MgO in the melt compositional parameter. The developed model that allows us to calculate fO_2 is shown in Eq.9.

Eq.8 $$D_{Fe-Ti}^{mgt/melt} = D_{FeO_{Tot}}^{mgt/melt} / D_{TiO_2}^{mgt/melt}$$

Eq. 9 $$\Delta QFM = \frac{\log\left(D_{FeO_{Tot}}^{\frac{mgt}{melt}} / D_{TiO_2}^{\frac{mgt}{melt}}\right) + 0.137 \cdot AMCNK + 0.102)/(}{(0.288 \cdot AMCNK + 0.054)}$$

Where AMCNK is the molar Al_2O_3/ (Na_2O + K_2O + CaO + MgO) ratio.

The main advantage of FeTiMM oxybarometer is that it can be applied to magmas that do not contain ilmenite, which is true for many igneous rocks of mafic to felsic composition, particularly for those that are alkali-rich [Arató et Audétat, 2017].

Fig. 8. Experimental results of the FeTiMM oxybarometer [Arató et Audétat, 2017].

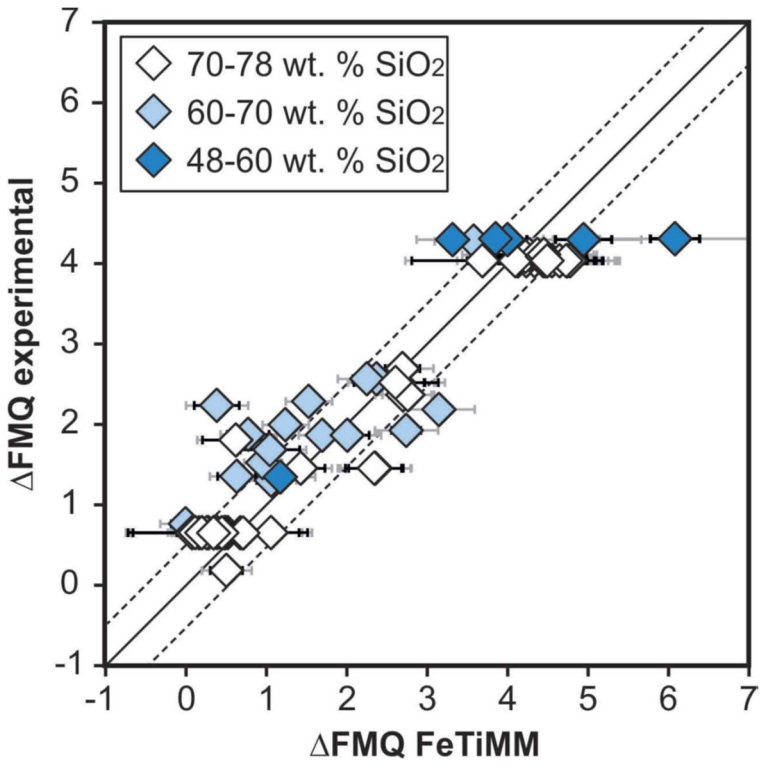

3.6 Olivine-Spinel-Orthopyroxene oxybarometry

The traditional method to compute the fO_2 of the magmatic system consists in several coupled mineral equilibria in the system olivine, spinel and orthopyroxene.

The following link:

http://melts.ofm-research.org/CORBA_CTserver/Olv_Spn_Opx/index.php

is an available online free tool, from the site of MELTS software. It is a software package to thermodynamic modeling of phase equilibria in magmatic systems. MELTS is based upon the work of Ghiorso and Sack, 1995, and Asimow and Ghiorso, 1998, and it is one of the most used software for petrological studies.

The specified tool allows us to calculate T and $\log_{10}$ (fO_2) for magmatic systems. The input is the oxide composition (wt%) of olivine, spinel, and orthopyroxene. Calculations are based upon thermodynamic models described in Sack and Ghiorso, 1989, 1991a ,1991b, 1994a, 1994b, 1994c.

4 Geological Background

4.1 Mt. Etna

Mt. Etna is one of the most active volcanoes in Europe, with a base diameter of 40 km, a height of 3340 m a.s.l., and covers an area of 1260 km^2. It is an Italian composite stratovolcano, located near to the Ionic coast of Sicily, with more than 500 ka of geological history. The basaltic volcanism of Etna is developed in an unusual geodynamic context, on the structural domain of the Gela–Catania Foredeep on the front of the Apennines–Maghrebian Chain that overlaps the undeformed African continental plate margin, the Hyblean Foreland [Lentini 1982; Ben Avraham and Grasso, 1990]. Eruptive activity began during middle Pleistocene, settled atop of the early middle Pleistocene marly-clays of the Gela-Catania Foredeep [Di Stefano and Branca, 2002] and the pre-historical evolution of Etnean volcanism can be divided into four phases [e.g. Branca et al., 2004a, 2004b, 2008, 2011, and references therein]:

1) Basal Tholeiitic Supersynthem (500-320 ky BP): Volcanic products are preserved in a restricted area between Acicastello and Acitrezza villages coasts. The main products consist of tholeiitic shallow subvolcanic bodies, pillow lavas, and hyaloclastic breccias [e.g. Branca et al., 2008; Tanguy et al., 1997, Corsaro and Cristofolini, 1997, 2000]. Lasted products are subaerial lava flows (330 ky BP) exposed near the Simeto river [Corsaro and Pompilio, 2004a]. There is an extended lava plateau between the towns of Adrano and Paternò, generated by fissure-type eruptions whose vents are covered by the younger volcanic activities. The eruptive fissure is bordered by alternated pyroclastic deposit of densely black scoriaceous lapilli and bombs layer and stratified ash layer. Pyroclastic deposit also contains sedimentary lithics of the Pleistocene marly-clay and alluvial pebbles. An isolated neck of tholeiitic lavas [Tangui, 1978] is located near Motta S. Anastasia town, about 4 km south-east of the lava plateau. This neck is intruded in the marine Pleistocene sediments, and it show a well-developed columnar joint. Along the wall of the neck, is preserved a pyroclastic deposit of scoriaceous lapilli and bread-crust bombs.
   Tholeiitic magmas are considered derived from the Hyblean magmatic source, which migrated to the north [Corsaro and Pompilio, 2004a; Correale et al., 2014, and references therein]

2) Timpe Supersynthem (220-110 ky BP): About 200 ky ago most of the activity was located along the eastern coast. The volcanic products related to this phase are exposed along the Ionian coast [Branca et al., 2008]. The mainly products are massive superposition of several lava flows, dipping SSW and SW generated by fissure-type eruptions. The base of the succession is formed by porphyritic lava flows from tholeiitic to transitional affinity [Tanguy et al., 1997] containing large

mafic crystals and nodules. During this phase, there is a chemical transition from tholeiitic to Na-alkaline affinity lavas [Corsaro and Pompilio, 2004, and references therein]. The top of these products is uncoformably covered by a volcaniclastic deposits, up to 60 m thick, mainly formed of debris flow and alluvial deposits. During the Timpe phase scattered monogenic centres erupted also on the south periphery of Mt. Etna. The remnants of these eruptions are limited outcrops of deep-weathered and eroded massive lava flows, 5-10 m thick. They were generated by fissure-type eruptions and a large proximal scoria deposit, about 800 m long, 500 m wide, and 100 m high, is preserved at Paternò town. The top of the volcanics products of this phase is marked by an erosional unconformity represented by debris flow and alluvial deposits along the Ionian cost and isolated lava relicts smoothed on the top and deeply eroded from drainage pattern.

3) Valle del Bove Supersynthem (110-65 ky BP): This phase is characterized by a westward shift of activity and eruption centralization, whose lead to the construction of several volcanic buildings: Tarderia (106 ky BP), Rocche (102 ky BP), Trifoglietto (100 ky BP) [De Beni et al., 2011]. This last volcano ended its activity with a Plinian eruption. Later buildings developed on the sides of collapsed Trifoglietto: Mt. Cerasa, Giannicola, Salifizio, and Cuvigghiuni.

4) Stratovolcano Supersynthem (last 65 ky): In this phase the volcanic activity moves again, shifting to the west and building a large stratovolcano. This phase can be represented by two main buildings, the Ellittico volcano (57-15 ky BP [De Beni et al., 2011]) and the Mongibello volcano (last 15 ky). The first one was characterized by the alternation of effusive and explosive activities, which ended its cycle with four plianian eruptions. The last Plinian eruption generated Biancavilla-Montalto ignimbrite [De Rita et al., 1991; Coltelli et al., 2000] and determined the building collapse. The formed caldera has a diameter greater than 4 km. Subsequent eruptions (effusive and highly explosives) filled the Ellittico caldera and built the Mongibello volcano. Mongibello is mainly characterized by effusive activity, with sporadic intense explosions. Around 6 ky BP, a large gravitative collapse of the eastern flank of the Mongibello building has created a large depression named Valle del Bove, which exposed a large part of the inner structure of the Mongibello and the oldest Ellittico.

The recent activity of Mt. Etna is related to the phase of current Mongibello. Volcanic activities can occur both the summit crater (“central eruptions”) and along with fractures which often opened on the volcanic flanks (“flank eruptions”). Central eruptions are located in the summit area, where the morphology varies over time. Actual craters are the “North East Crater” (NEC, the highest tip of Mt. Etna, 3350 m), the “Voragine” (1945), “Bocca Nuova” (1968). The “South East Crater” (SEC, 1971) was completely overshadowed by a new one, called “New South East Crater” (NSEC) during several

paroxysmal events from 2011 to 2013 [e.g. Behncke et al., 2014]. Flank eruptions are very frequent, as witnessed by 338 monogenetic cones of different ages on the volcano slopes [Armienti et al., 2004], usually located along with the main volcano-tectonic structures. Chemical compositions of flank lavas are similar to those that erupted in the summit area. Besides the described activities, there are particular eruptions named “Eccentric” [Rittmann, 1965] or “Deep Dyke Fed” [Corsaro et al., 2009]. These eruptions are characterized by moderately to highly explosive style eruptions, which bypass the region of the central conduit [Corsaro et al., 2009, and references therein]. These eruptions are located further away from the volcanic building and produce the most primitive magmas of Mt. Etna. Eccentric eruptions are Mt Maletto and Mt. Spagnolo eruptions (15–5 ky BP) [Armienti et al., 1988; Kamenetsky and Clocchiatti, 1996; Correale et al., 2014; Corsaro and Métrich, 2016], FS Eruption (~4 ky BP), [Coltelli et al., 2005; Kamenetsky et al., 2007] Montagnola (1763), [Miraglia, 2002; Corsaro et al., 2009; Correale et al., 2014] Mts. De Fiore (1974), [Corsaro et al., 2009; Correale et al., 2014] 2001 and 2002/2003 eruptions [Métrich et al., 2004; Spilliaert et al., 2006a, 2006b; Corsaro and Métrich, 2016].

Fig. 9. Slope map of Mt. Etna [Favalli et al., 1999], modelled on DEM.

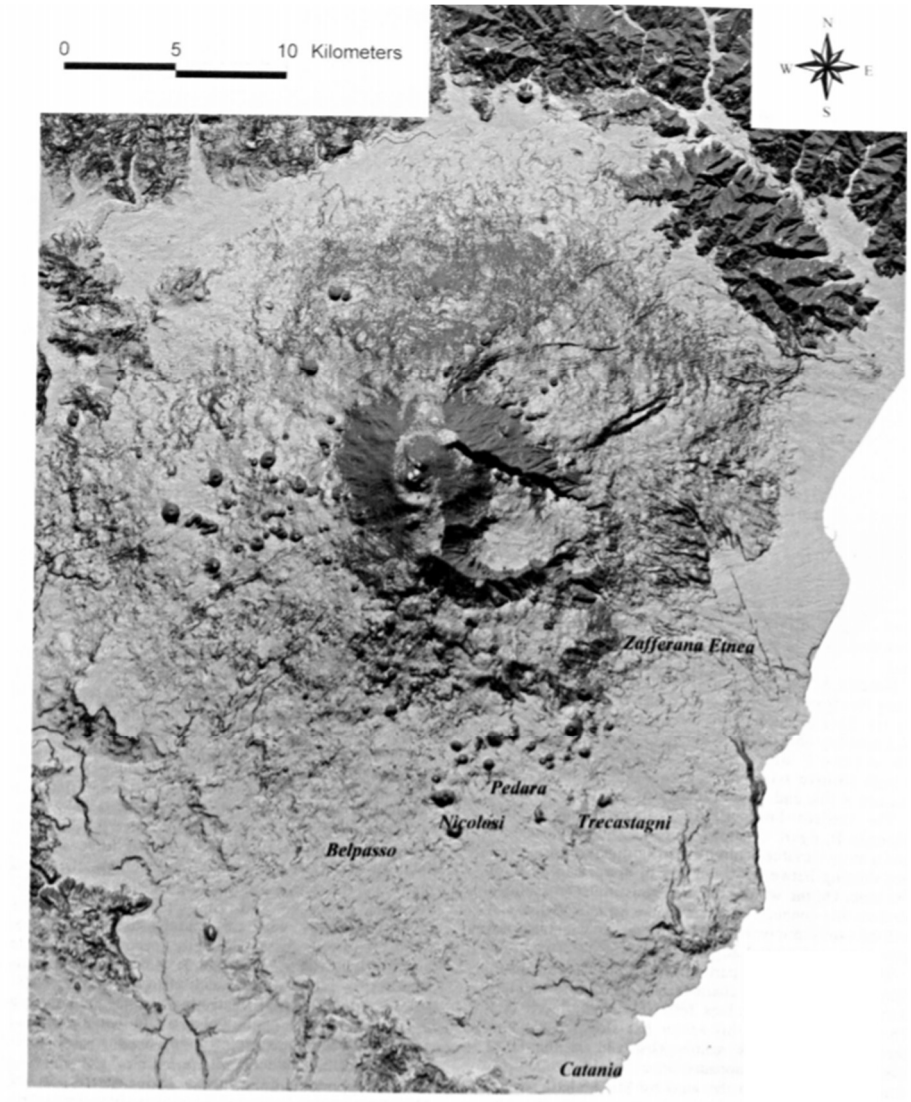

4.2 Ischia Island

Located at the North-western corner of the Gulf of Naples (South Italy) Ischia Island is the emerged part of a large volcanic build which rises from the sea level to the top of the Monte Epomeo (788m), formed in the graben of the Campanian Plain, along the Tyrrhenian margin of the Apennines [e.g. Orsi et al., 2003; Peccerillo, 2005], which, since the Miocene, has been involved in extensional processes related to the eastward migration of the Apennines concerning a progressive eastward retreat of the Ionian slab [Jolivet et al., 2009, and references therein]. Ischia is one of the four Neapolitan volcanoes NE-SW aligned with Procida and Campi Flegrei, it is resurgent caldera as Campi Flegrei [e.g. Orsi et al., 1991], while Somma-Vesuvius is a stratovolcano [e.g. Santacroce et al., 2008] and Procida is a monogenetic volcanic field [e.g. De Astis et al., 2004]. A complex interplay among tectonism, volcanism, erosion, and sedimentation characterized the history of the island [Orsi et al., 1991, 1992, 1996b; Brown et al., 2008; Sbrana et al., 2009, and references therein].

Fig. 10. Structural sketch map of the Campanian Plain and surrounding Apennines, modified after Orsi et al. (2003).

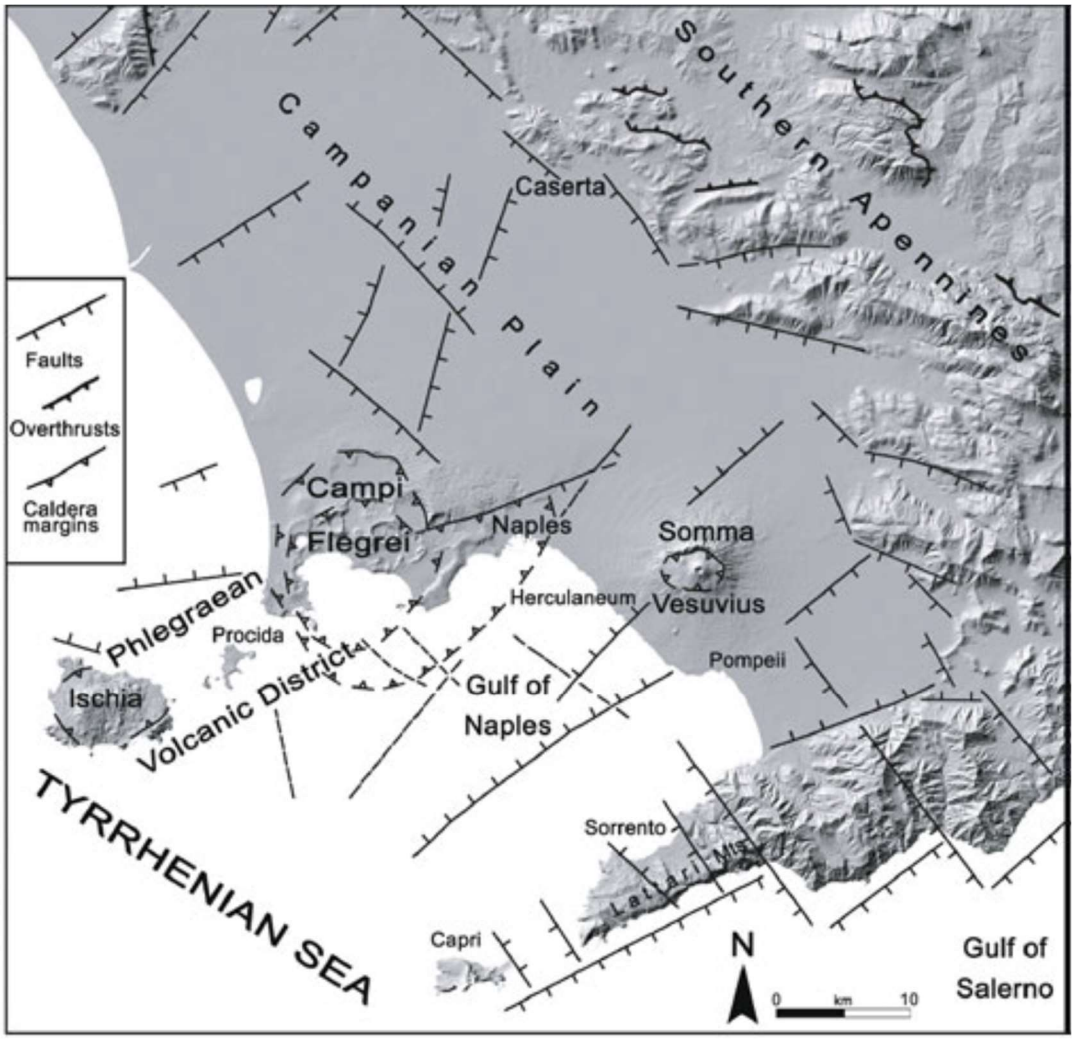

Fig. 11. Geological sketch map of Ischia, modified after Orsi et al. (2003).

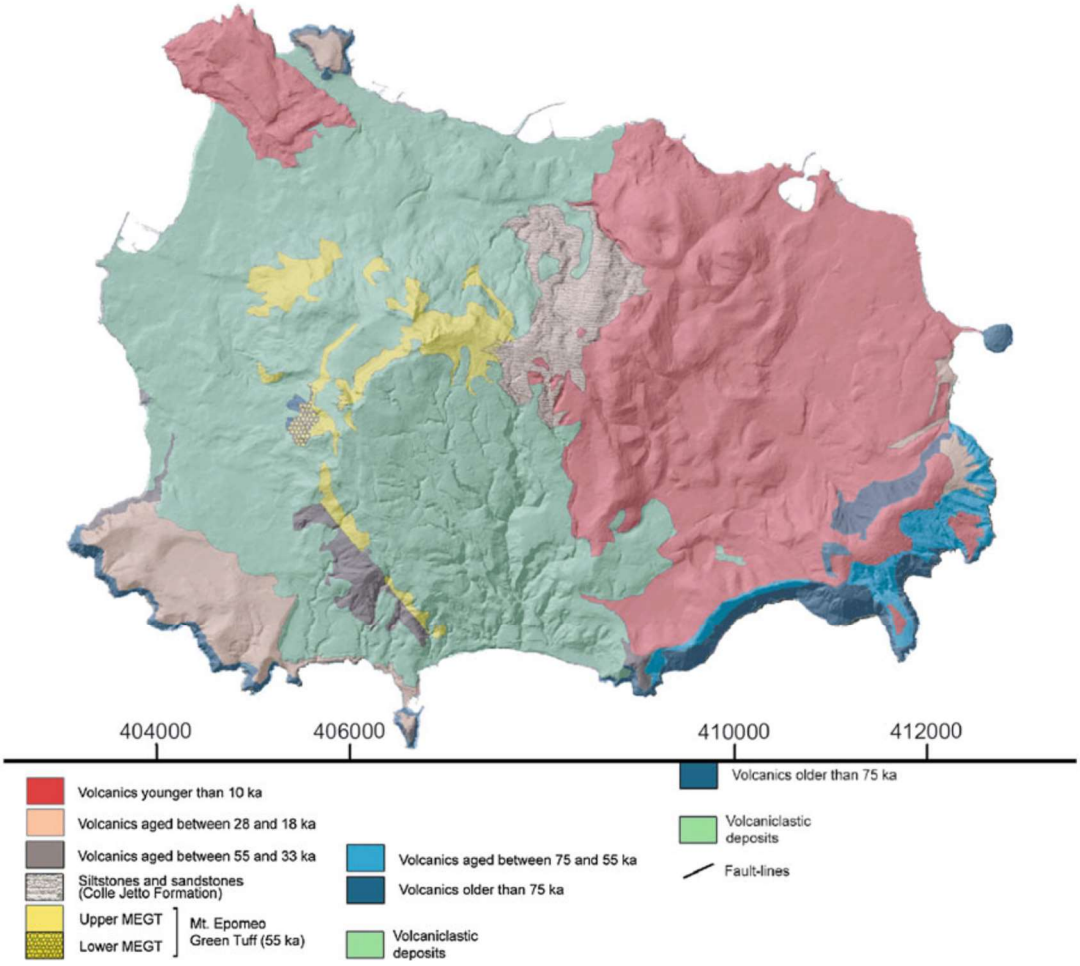

The history of Ischia volcanism can be distinguished in six evolutive phases identified on the basis of volcano-tectonic events [Sbrana et al., 2018, and references therein]:

1) Phase 1 (>150-73 ka ago): The building of Ischia volcanic field occurs in this first phase. The oldest rocks are pyroclastic units interbedded with palesols, dated 150 ka [Vezzoli, 1988]. These rocks are remains of an ancient volcanic build located in the SE corner of the island. Most of the ancient activity produced monogenic tuff cones, lava domes, spatter cones, lava flow, but also rarely Plinian deposits occur. An explosive paroxysm is recorded in the volcanic succession around 100 ka ago, which form L'Elefante and Spiaggia d'Agnone units. This volcanism lasted until 73 ka ago, is mainly represented by effusive trachytic and phonolitic lavas, which generated small lava domes. Intermitted explosive activity generated small alkali-trachytic pyroclastic deposits.

2) Phase 2 (73-55 ka ago): Ischia caldera-forming phase started Since 73 ka ago. It is an intense period of explosive activity characterized by Plinian or sub-Plinian eruptions. Main explosive products are the pumice of Pignatello formation,

the ignimbrite plateau formed by the deposits of Pizzone and Frassitelli, which had its climax with the caldera-forming eruption Monte Epomeo Green Tuff (MEGT) event at 55 ka [Brown et al., 2008].

3) Phase 3 (55-33 ky): The first post-caldera period began after the trachyte caldera-forming MEGT eruption. The beginning of resurgence occurred around 45 ka ago with the Citara tuff cone located in the western offshore area after about 11 ky of volcanic stasis. In the same period, the super-eruption in the Campi Flegrei volcanic field known as the Campanian Ignimbrite occurred [Marianelli et al., 2006]; deposits of this event are interlayered in the ischian succession. The MEGT caldera depression was then invaded by the seawater and tuff was emplaced in this depression in both marine and subaerial environments. Phreatomagmatic and magmatic explosions of trachytic to alkali-trachytic products occurred along the western coastline of the island up to 33 ka.

4) Phase 4 (29-18 ka ago): The second period started after a repose of 8 ka, with the shoshonitic eruption of Grotta di Terra, along the south-eastern coastline. Phreatomagmatic and magmatic explosive eruptions emitted alkali-trachytic magmas, while effusive eruptions generated trachytic lava flows. This volcanism persisted until 18 ka.

5) Phase 5 (10 – 5 ka): This period was mainly characterized by effusive events of trachytic, and subordinately latitic, magmas through lava flows and domes extrusion. Many of the eruptive vents were located in the eastern depression of Monte Epomeo, although a few vents occurred in the NW corner of the island. The phase was closed by a phreatoplinian eruption of Piano Liguori (5.6 ka ago), which produced a tick ashy layer that covered all the south-eastern relief of the island. The source area of this eruption, possibly subsided or collapsed after the eruption. During this phase, several debris avalanches and landslide deposits were emplaced due to sector collapse of the flanks of the Mount Epomeo resurgent block.

6) Phase 6 (3.7 ka ago - 1302 A.D.): In the recent past of Ischia the Molara, Vateliero and Cava Nocelle eruptions followed each other at short time intervals between the 6th and 4th centuries BC. The Vateliero, Molara and Cava Nocelle eruption centres are aligned along NE-SW faults with regional importance, which divided the structural relief of Monte di Vezzi from the Ischia graben and Mount Epomeo horst. The scoriae of the Molara, Vateliero and Cava Nocelle centers cover in discordance both the ashes of the Piano Liguori Formation as well as the Cantariello pumices and the Rosato landslide deposits. According to Buchner, 1975, the scoriae of Vateliero center overlie a paleosol with Roman pottery of the IInd and IIIrd century A.D. The volcanic activities of these volcanic centers most probably were not contemporaneous. The Vateliero centre is the southernmost

one and is represented by a crater with a diameter of 250m and a depth of 50 m. Bread-crust shaped bomb and massive lava blocks mantle the pre-existing morphology and not make a cone. The Molara centre is a 250m and 20m deep crater, bordered in the western side by 40m high black and reddish air-fall scoriae rampart. A lava flow of 2500m^2 partially occupies the floor of the crater. The Cava Nocelle centre consists of a crater of 200m diameter, occupied by a modest lava flow, and bordered by reddish scoriae deposits [Buchner, 1975]. Other small craters of smaller dimension are scattered around the three main volcanic centres. Two phreatic craters of 150m and 60m respectively, are particularly recognizable at the east of the Vateliero crater. A partially eroded crater can be observed between those of Molara and Cava Nocelle. A circular-shaped depression with a diameter of 70m located north of Molara crater may be interpreted as an explosion crater

Ischia volcanic rocks composition embrace many kinds of evolution degree. The least evolved magmas erupted during the second period post-MEGT, represented by shoshonitic dike at Grotta di Terra, and over the past 3 ky eruptions.

4.3 Hyblean Plateau

Hyblean Plateau is geographically identified with the southeast corner of Sicily (Fig. 4), in a complex geodynamic framework. This area is characterized by the collisions between the European and African plates [e.g. Barberi et al., 1974]. The Hyblean Plateau represent the undeformed foreland of the northern portion of Pelagian Block, in continuity with the African plate. The Plateau is in contact with the Apennine-Maghrebian Chain through the Gela foredeep in the NW, while the eastern border is sharply joined to the Ionian Basin by the Malta Escarpment.

This area has been characterized by several episodes of magmatism which starting from the Triassic and lasting until the Quaternary [e.g. Carbone and Lentini, 1981; Rocchi et al., 1998]. The oldest magmatic products were detected near Siracusa, via drill holes, in a Triassic layer [e.g. Cristofolini, 1966], while the oldest eruptive rocks that reach the surface, are Cretaceous alkali basalts which are located in the eastern part of the area (Capo Passero, Siracusa, and Augusta) [e.g. Amore et al., 1988]. Here, the 12 km thick sedimentary sequence of Meso-Cenozoic deep-water carbonate deposits and the Neogene-Quaternary clastic sequences is interrupted by several volcanic layers, produced from the numerous eruptions [Bianchi et al., 1987]. The subsequent activity restarted about 50 My later with alkaline lavas, during Miocene, in the central-northern area of Hyblean Plateau [e.g. Bianchi et al., 1987]. The last eruptive episode, during Plio-Pleistocene, was characterized by tholeiitic basalts to OIB-like lava flow, and minor nephelinites [e.g. Beccaluva et al., 1998].

Some diatreme volcanism events during the Miocene age and some Quaternary basanitic-nephelinitic lavas of Hyblean Plateau brought to the surface many mantle-derived xenoliths, manly spinel-peridotites, and some pyroxenites, which have been

widely investigated by many authors [e.g. Correale et al., 2012, Bianchini et al., 2010, Perinelli et al., 2008]. Some of this mantle xenoliths from diatremes exhibit a primitive character, due to the relatively low eruptive temperature and high ascent rate of these products. Thus, Hyblean xenoliths allow providing unique information on the upper-mantle composition and the processes which may modify it.

Fig. 12. Map of Hyblean Plateau. [Perinelli et al., 2008]. The diatreme of Valle Guffari is shown in this sketch. It is the provenance of most of the mantle xenoliths.

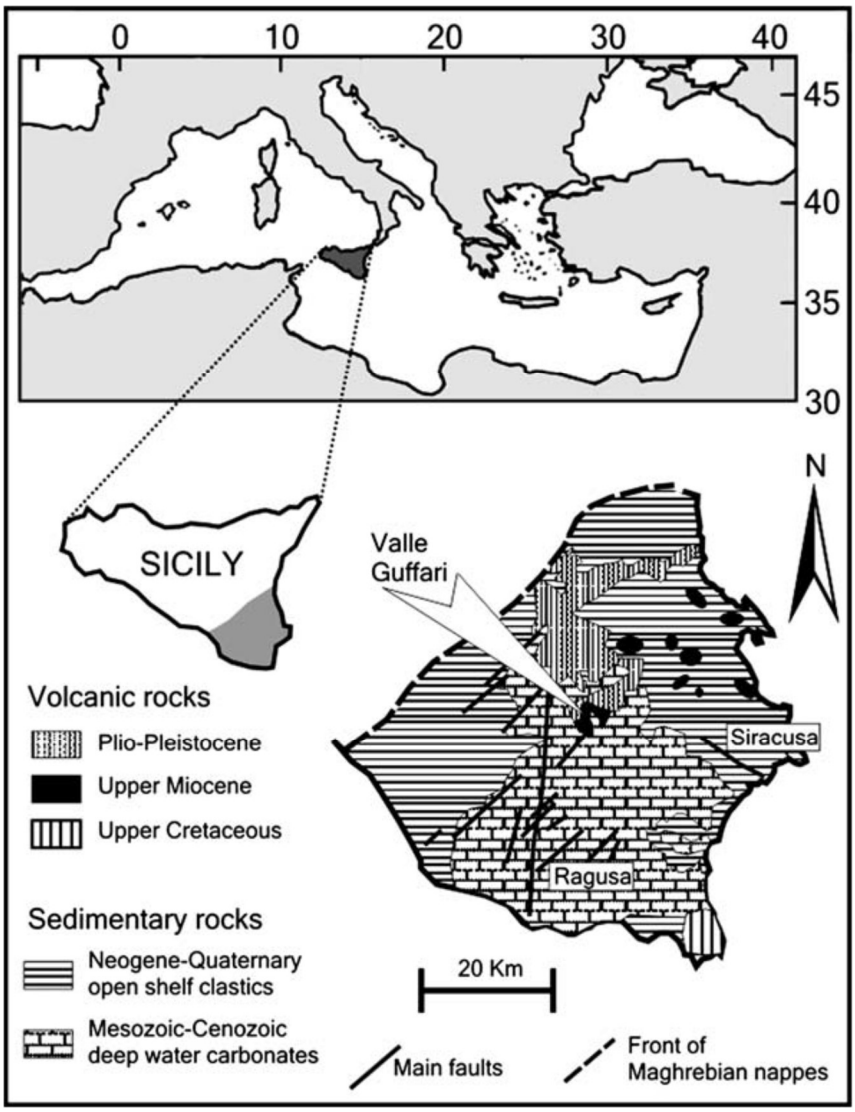

5 Samples selection and analytical methods

5.1 Etna and Vateliero samples selection and preparation

The selection of the volcanic sites to be investigated has been determined on two main criteria. First, the sites must have belonged to different geodynamic environments, to determine the mantle redox variability over different settings; and second, primitive products must have erupted and available in the history of the volcano.

The site of Mt. Etna has been selected as representative of intraplate magmatism and for the abundance of primitive products in its eruptive record. We selected the FS eruption. It is a fall stratified (whose acronym names the product) tephra dated 3960 ± 60 BP (^{14}C age) [Coltelli et al., 2000], resulting from a pyroclastic fall out of 0.183 km^3 which covered the eastern flank of Mount Etna [Coltelli et al.,2005, and references therein]. The deposit dimensions indicate that the height of the eruption column reached 18-20 km, and thus had high explosive sub-Plinian energy [e.g. Coltelli et al., 2005]. The erupted products are highly vesiculated (30-60 vol%) scoria lapilli containing euhedral olivine (Fo_{90-92}), then clinopyroxene ($Wo_{42-43}En_{44-47}Fs_{4-6}$) and low content of Cr spinel [e.g. Kamenetsky et al., 2007; Correale et al., 2014]. The rocks are rich in Mg, representing the most primitive magma of Mount Etna, the least modified from the source of Etnean magmatism which reached the surface [e.g. Coltelli et al., 2005].

The second chosen site is Ischia island, as representative of subduction-related magmatism. Most of the products that erupted in Ischia are intermediate to evolved, but the last eruption of Ischia, Cava Nocelle, and Vateliero tephra are primitive basalts. Vateliero tephra was chosen as the best to investigate, due to the abundance of bigger-size olivine compared to Cava Nocelle olivine, and a large number of melt inclusions. This product shows large chemical heterogeneity between primitive olivine (Fo_{85-90}) and more evolved crystals (Fo_{76-83}) that will be discussed later.

A third site is the Hyblean Plateau. The mantle xenoliths from the diatreme of Valle Guffari are representative of the mantle beneath the southeast of Sicily. We tried to investigate these xenoliths for many reasons: they are known products directly derived from mantle by diatreme craters [Perinelli et al., 2008] thus well representative of mantle conditions; clear relationship exist between the oldest Hyblean mantle and the recent Etnean mantle [e.g. Correale et al., 2012]; and then to test V-redox models on mantle xenoliths olivine.

At Instituto Nazionale di Geofisica e Vulcanologia (INGV), Sezione di Palermo, the tephra samples from Mt. Etna and Ischia island were disrupted using a rock mill. The products were sifted with a succession of sieves with decrescent size, 2 mm, 1 mm, 0.5 mm. For Mt. Etna there is a high number of crystals with a size greater than 1 mm, therefore the chosen sample was that of size >1 mm. For Ischia 0.5 mm size samples were chosen, due to a lower granulometry of the olivine crystals. The olivine samples of selected granulometry were manually separated from the other crystals and the glassy matrix using an optical microscope.

The MIs were found by using a polarizing microscope. Olivine hosting melt inclusions were treated with lapping, to surfacing the MIs, and then polished one by one using abrasive paper with a variable granulometry from 1200 to 12000 mesh (12 µm to 1 µm), to smooth them the best as possible. Finally, olivine samples were mounted in epoxy resin.

Fig. 13. Large MIs within olivine of Vateliero tephra, photos taken at transmission polarized microscope.

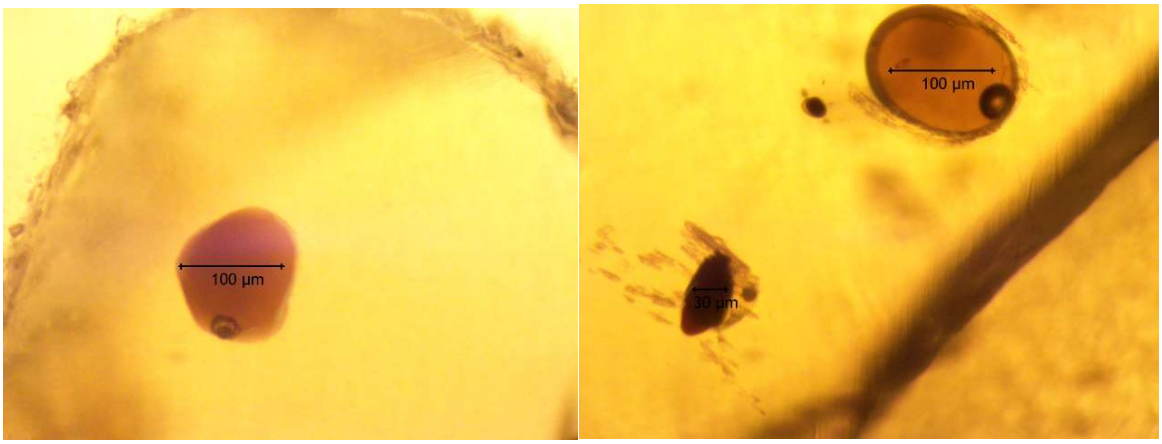

5.1.1 Scanning electron microscope (SEM)

Host olivine and relative MI were observed by scanning electron microscope (SEM) at the Institut des sciences de la Terre d'Orléans (ISTO), France. All samples were first washed in acetone and ethanol solutions and then coated with a carbon film to increase the surface conductivity. Images were acquired with a Zeiss Merlin Compact, using 15 keV electron beam energy. SEM observations were necessary to have a semi-quantitative spectrum and to check the smoothest areas of MIs, to choose the best points for subsequent electron microprobe analysis.

Fig. 14. SEM images of a round-shape MI hosted within olivine.

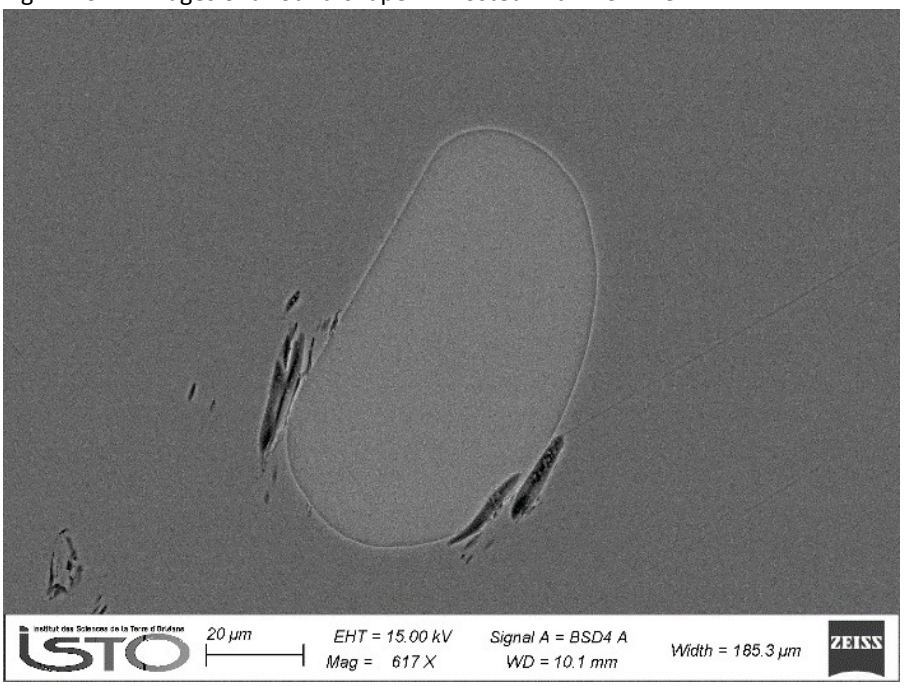

5.1.2 Electron probe microanalyzer (EMPA)

Polished sections from Mt. Etna and Ischia of olivine and MIs were examined by Electron Probe Microanalyzer (EMPA) at the ISTO. Major elements concentration of samples was determined using the following parameters:

- Defocused beam of 6 µm size
- Beam energy of 15keV
- Current intensities of 6 nA
- Counting time of 10 seconds for all measured element excepting for S. Counting time of 60 seconds for S.

For Etna olivine, measured oxides were SiO_2, TiO_2, Al_2O_3, FeO, MnO, MgO, CaO, Na_2O, K_2O, and SO_2, while for Ischia olivine the same oxides except for SO_2, and also P_2O_5, Cr_2O_3, and NiO. Natural minerals were used as internal standards during the analyses. Etna MIs were investigated for the same elements of the hosting olivine, while Ischia MIs were investigated for the same elements of hosting olivine, except for Cr_2O_3 and NiO, and also SO_2 was measured. Mn is usually slightly above the detection limit of the instrument, and in many samples, it is not properly resolved.

Analyzed elements were calibrated on natural minerals and oxides, which were used as internal standards during the analysis:

- Na and Si on albite
- K on orthoclase
- Ca on anhydrite
- P on apatite
- Other elements on relative oxides.

Fig. 15. a) Scanning electron microscope and b) electron microprobe at the ISTO. These two instruments were used for observation and analysis of major elements of the olivine and hosted MIs.

5.1.3 Laser ablation inductively coupled plasma-mass spectrometry

Trace elements concentrations were determined by Laser Ablation Inductively Coupled Plasma-Mass Spectrometry (LA ICP-MS) at INGV. It is a technique for the analysis of solid materials for a wide range of elements at ppm levels at variable spatial resolution.

The fluoride laser beam ablates the sample, and a He flux is used as a gas carrier for aerosol transport from the ablation cell to the ICP-MS, where the sample is vaporized, atomized, and ionized by a torch. The analyses were conducted under these parameters:

- He flows of 769 ml/min
- Beam energy of 26 kV
- Laser Fluency (F) of 14 J/cm^2
- Beam size of 60 µm for olivine, 32 µm for MIs.

Used standard materials were:

- National Institute of Standards and Technology (NIST) 612 for MIs.
- NIST 614 for olivine
- Basalt Columbia River (BCR) 2

5.2 Hyblean xenoliths: literature data

The Hyblean spinel peridotite xenoliths collected and analyzed in Correale et al., 2012 were investigated to collect olivine samples and find some MIs. Due to the nature of the olivine, not even one MI was found, excluding the possibility of investigating Hyblean xenoliths as FS and Vateliero products. Since minerals analyses of these xenoliths are available in the literature, we decided to use the chemical analyses published in Perinelli et al., 2008. We have chosen this published study to make a comparison between published redox data and those computed from our work.

6 Results

6.1 Whole rocks composition

Major element composition of studied tephra is reported in Table 1.

As concerns FS the reported bulk composition is that from Correale et al., 2014. FS samples are picro-basalts with a SiO_2 average content of 45.05 wt.%, MgO of 17.58 wt.%, and low alkali content (Na_2O+K_2O = 1.36 wt.%).

The reported Vateliero bulk composition is that from Peccerillo, 2005. Vateliero tephra can be classified as a basaltic-trachyandesite [Le Bas et al., 1986], with an SiO_2 average content of 53.36% wt.%, MgO of 3.82% and a high alkali content (Na_2O+K_2O = 8.67 wt.%).

Table 1. Major elements in the studied rocks. Mg# = 100 · Mg/(Mg+Fe_{tot})

	FS (wt.%)	VAT (wt.%)
SiO_2	45.05	53.36
TiO_2	0.83	1.07
Al_2O_3	9.32	17.32
Fe_2O_3	10.25	6.94
MnO	0.16	0.13
MgO	17.58	3.82
CaO	11.02	7.12
Na_2O	1.12	3.94
K_2O	0.51	4.73
P_2O_5	0.21	0.33
Total	98.72	98.76
Mg#	77.3	35.50
CaO/Al_2O_3	1.18	0.41

6.2 Petrography and mineral composition

6.2.1 FS tephra

FS groundmass is glassy, highly vesiculated (>50 vol.%), and almost aphyric (~10 vol.%). Phenocrysts are represented by three minerals: highly magnesian euhedral olivine, up to 1 mm in size, with Forsterite amount which ranges between 89-91 (Fo_{89-91}) (Table 2), subhedral crystals between 0.5-2 mm length clinopyroxene with mineralogical composition $Wo_{42-43}En_{44-47}Fs_{4-6}$, and rare microphenocrysts of Cr-spinel (Cr_2O_3 = 38-52 wt.%) which are often hosted within olivine phenocrysts.

Almost all trace elements are poorly concentrated in olivine (Appendix. Table A1.1), except for few olivine compatible elements such as Ni, which range from 679 to 1490 ppm, and poorly compatible elements such as Co, (85.18 to 106.41 ppm) and Cr (85.98 to

394.96 ppm). V, that is an incompatible element, shows a homogeneous low concentration (between 1.68 and 2.48 ppm).

6.2.2 Vateliero tephra

This rock is a not-welded pyroclastic material, in which there are mineral phenocrysts of olivine, clinopyroxene, Cr-spinel, magnetite, and rarely apatite. Olivine phenocrysts (Table 2), show a forsterite content variable from 76 up to 90 (Fo_{76-90}), in which two distinct groups can be recognized (as suggested by D'Antonio et al., 2013): Mg-rich olivine with Fo content ranging from 85 to 90 mol %, and Mg-poor olivine with Fo from 76 to 83 mol %. The phenocrysts are generally homogeneous in their chemical composition. Cr-spinel, magnetite, and apatite microphenocrysts are commonly hosted within olivine phenocrysts.

Olivine trace elements are usually poorly concentrated (Appendix Table A1.2). Ni and Cr concentration are variable from 372.98 to 1734.08 ppm, and from 1.57 to 269.31 ppm respectively. These elements are more concentrated in primitive olivine with higher Mg# and decrease according to Mg# (Fig. 16). V concentration range between 2.93 and 7.35 ppm and it is higher in evolved olivine then in the most primitive crystals.

Fig. 16. Ni and Cr concentration vs Mg# of Vateliero olivine. These two elements concentration is strongly related to the Mg# of the mineral, clearly showing the two groups of olivine as described by D'Antonio et al., 2013.

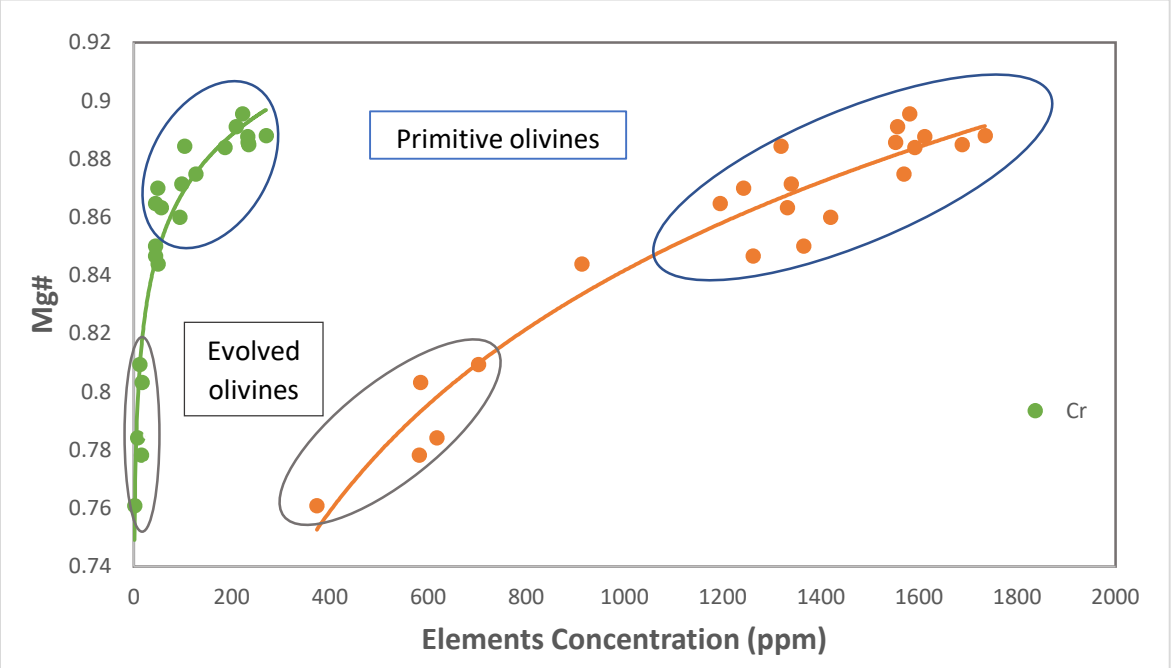

Table 2. Olivine major elements chemical compositions expressed as wt%; b.d.l = below detection limit.

	FS 01 Oliv	FS 02 Oliv	FS 03 Oliv	FS 04 Oliv	FS 05 Oliv	FS 06 Oliv	FS 08 Oliv	FS 11 Oliv	FS 12 Oliv
SiO_2	41.03	40.46	40.85	40.63	40.41	40.61	40.80	39.54	40.18
TiO_2	0.078	0.007	0.017	b.d.l.	b.d.l.	0.014	0.021	0.078	0.007
Al_2O_3	0.02	0.03	0.02	0.03	0.03	0.03	0.02	0.02	0.02

FeO	9.54	9.57	9.55	9.63	9.55	9.41	9.86	9.65	9.57
MnO	0.252	0.198	0.059	0.177	0.156	0.179	0.091	0.083	0.083
MgO	48.80	49.43	49.23	49.27	49.52	49.50	48.93	50.33	49.87
CaO	0.25	0.24	0.24	0.24	0.27	0.22	0.21	0.26	0.22
Na_2O	0.014	0.017	0.012	0.010	0.015	0.012	0.033	0.018	0.012
K_2O	0.003	0.034	0.016	0.004	0.020	0.015	0.017	0.015	0.000
Mg#	0.901	0.902	0.902	0.901	0.902	0.904	0.898	0.903	0.903
	FS 13 Oliv	FS 14 Oliv	FS 16 Oliv	FS 17 Oliv	FS 18 Oliv	FS 19 Oliv	FS 22 Oliv	FS 24 Oliv	FS 25 Oliv
SiO_2	40.14	41.41	42.27	40.10	41.13	41.42	40.95	41.22	40.84
TiO_2	0.007	b.d.l.	0.018	0.020	b.d.l.	0.039	0.034	0.014	0.012
Al_2O_3	0.01	0.03	0.04	0.08	0.02	0.04	0.04	0.01	0.01
FeO	9.41	9.91	9.92	9.69	9.97	9.51	9.98	9.85	9.34
MnO	0.107	0.142	0.146	0.173	0.139	0.184	0.116	0.132	0.121
MgO	50.06	48.19	47.28	49.66	48.46	48.53	48.62	48.49	49.38
CaO	0.23	0.29	0.27	0.22	0.25	0.24	0.23	0.25	0.25
Na_2O	0.014	0.034	0.007	0.016	0.015	0.015	0.011	0.010	0.017
K_2O	0.002	0.000	0.049	0.034	0.019	0.016	0.010	0.014	0.012
Mg#	0.905	0.897	0.895	0.901	0.896	0.901	0.897	0.898	0.904
	FS 26 Oliv	FS 28 Oliv	VAT 01 Oliv	VAT 02 Oliv	VAT 03A Oliv	VAT 03 Oliv	VAT 04 Oliv	VAT 05 Oliv	VAT 06 Oliv
SiO_2	40.81	40.69	39.32	40.98	38.50	39.58	38.09	39.76	38.32
TiO_2	0.006	0.056	0.040	0.044	0.030	0.029	0.024	0.038	0.039
Al_2O_3	0.03	0.03	0.07	0.01	0.06	0.05	0.04	0.05	0.02
FeO	9.29	9.61	11.16	10.93	11.15	10.93	21.94	11.20	10.86
MnO	0.158	0.108	0.141	0.156	0.244	0.248	0.289	0.280	0.244
MgO	49.47	49.22	48.62	47.24	49.53	48.66	39.20	48.09	49.90
CaO	0.23	0.25	0.31	0.31	0.32	0.35	0.28	0.25	0.29
Na_2O	0.014	0.004	0.025	0.018	0.009	0.016	0.013	0.006	0.025
K_2O	0.000	0.022	0.016	0.015	0.014	0.004	0.015	0.018	0.009
Mg#	0.905	0.901	0.89	0.89	0.89	0.89	0.76	0.88	0.89
	VAT 07A Oliv	VAT 07B Oliv	VAT 08 Oliv	VAT 09 Oliv	VAT 10 Oliv	VAT 11 Oliv	VAT 12 Oliv	VAT 13 Oliv	VAT 14 Oliv
SiO_2	39.13	39.73	40.10	40.29	38.11	40.25	39.10	37.97	38.70
TiO_2	0.035	0.115	0.015	0.002	b.d.l.	0.012	0.083	0.011	0.029
Al_2O_3	0.04	0.03	0.01	0.06	0.03	0.03	0.02	0.02	0.04
FeO	20.23	19.59	11.98	12.98	18.06	12.26	10.33	15.20	13.51
MnO	0.262	0.239	0.275	0.221	0.327	0.183	0.226	0.226	0.201
MgO	39.86	39.97	47.05	46.02	43.05	46.68	49.75	46.14	47.08
CaO	0.26	0.27	0.35	0.33	0.27	0.30	0.32	0.32	0.30
Na_2O	0.020	0.021	0.015	0.004	0.035	0.016	0.027	0.025	0.015
K_2O	0.032	0.003	0.005	0.012	0.016	0.037	0.000	0.009	0.028
Mg#	0.78	0.78	0.87	0.86	0.81	0.87	0.90	0.84	0.86
	VAT 15 Oliv	VAT 16 Oliv	VAT 17 Oliv	VAT 18 Oliv	VAT 19 Oliv	VAT 21 Oliv			
SiO_2	38.54	39.51	39.82	40.63	39.98	41.25			
TiO_2	b.d.l.	0.043	0.020	0.005	0.012	0.016			

Al_2O_3	0.03	0.03	0.05	0.03	0.04	0.03
FeO	18.44	12.45	14.17	11.09	12.94	14.13
MnO	0.290	0.201	0.216	0.157	0.228	0.203
MgO	42.25	47.24	45.14	47.45	46.43	43.84
CaO	0.28	0.28	0.31	0.33	0.26	0.32
Na_2O	0.028	0.026	0.004	0.005	0.004	0.024
K_2O	0.006	0.007	0.008	0.021	0.006	0.009
Mg#	0.80	0.87	0.85	0.88	0.86	0.85

6.3 Melt Inclusions

More than 100 olivines were observed for Vateliero, and up to 250 for FS, with the aim to select MIs suitable for our study. Only the least evolved and visibly not crystallized MIs were chosen. Moreover, it was necessary to select those of sufficient size for LA ICP-MS analyses (>30µm size). About thirty samples for each tephra were collected, vary in size from 30 to 250 µm.

Fig. 17. Shrinkage bubbles within Melt Inclusions contained in FS olivine. They are formed as a consequence of a different thermal expansion coefficient between the melt silicate phase, and the host olivine crystal. In the case of such large bubbles, the formation of a gas phase exsolved by melt is also considered.

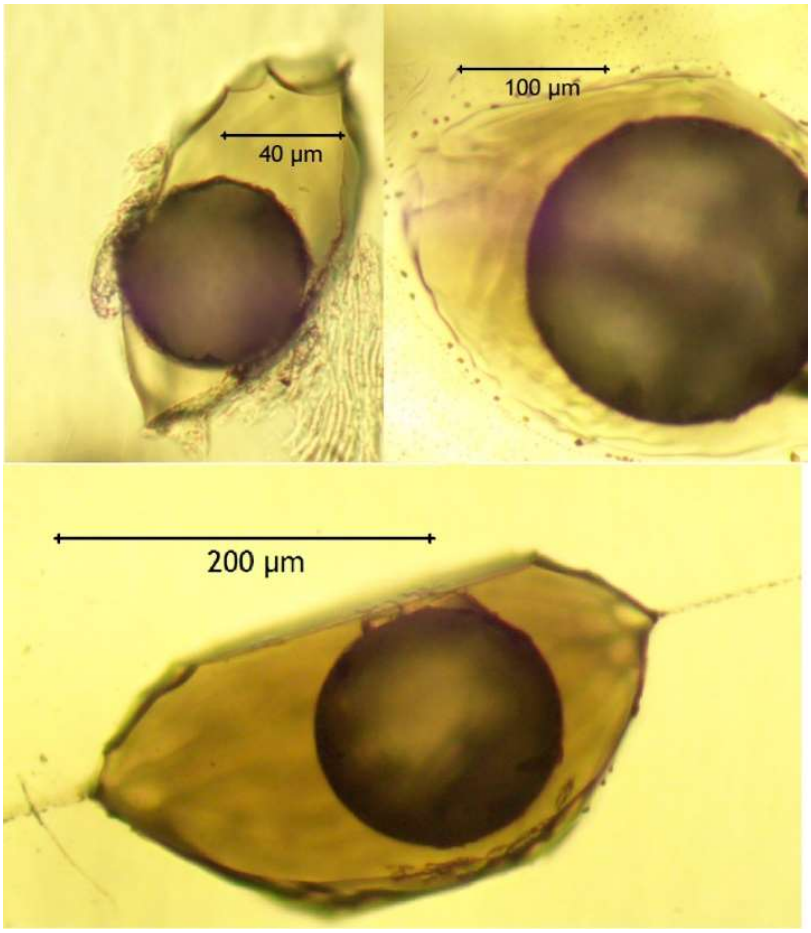

Many shrinkage bubbles of variable sizes are contained within MIs. During cooling the difference in the thermal expansion coefficient between the silicate melt and the hosting olivine leads to the formation of these peculiar bubbles. For many MIs from FS, entrapped bubbles volumes are high (Fig. 17), and could imply volatile degassing before quenching.

After trapping of the inclusion, the cooling phenomena produce the crystallization of an olivine border on the rim of the inclusion. The consequence is a change of the MI chemistry and MI evolving as a progressive olivine crystallization. Furthermore, due to the evolution of the melt, the olivine rim is progressively enriched in FeO and depleted in MgO, resulting in a compositional gradient within the rim. The compositional gradient causes a secondary re-equilibration of the in the inclusion with its host. The processes defined as "Fe loss" [Danyushevsky et al., (2000)], consist in the rapid Fe diffusion out from the melt, due to the gradient re-equilibration, while a fast cooling can preserve from this phenomenon and avoids the Fe-loss. Recalculation of the previous chemical composition, to eliminate the effect of the post-entrapment crystallization, was obtained assuming olivine-liquid equilibrium partitioning of FeO and MgO between host olivine and liquid. A crystal-melt distribution coefficient $K_D[(FeO/MgO)_{Oliv}/(FeO/MgO)_{melt}] = 0.26$ was used [Di Carlo et al., 2006]. The computed post entrapment crystallization range from 3% to 14% for FS samples, and between 3% to 12% for Vateliero samples.

In some inclusions, very small crystals of oxide minerals are observed (Fig. 18). For FS olivines they could not be characterized due to their small sizes. For MIs from VAT, many analyzed oxides revealed to be Cr-spinel and rare magnetite. Since V is strongly partitioned in oxide minerals, only oxide-free MIs were used to compute V partitioning.

Fig. 18. a) Oxide mineral within an FS melt inclusion. b) Two large oxide within a Vateliero melt inclusion. These images were obtained from SEM at the Institut des Sciences de la Terre d'Orléans.

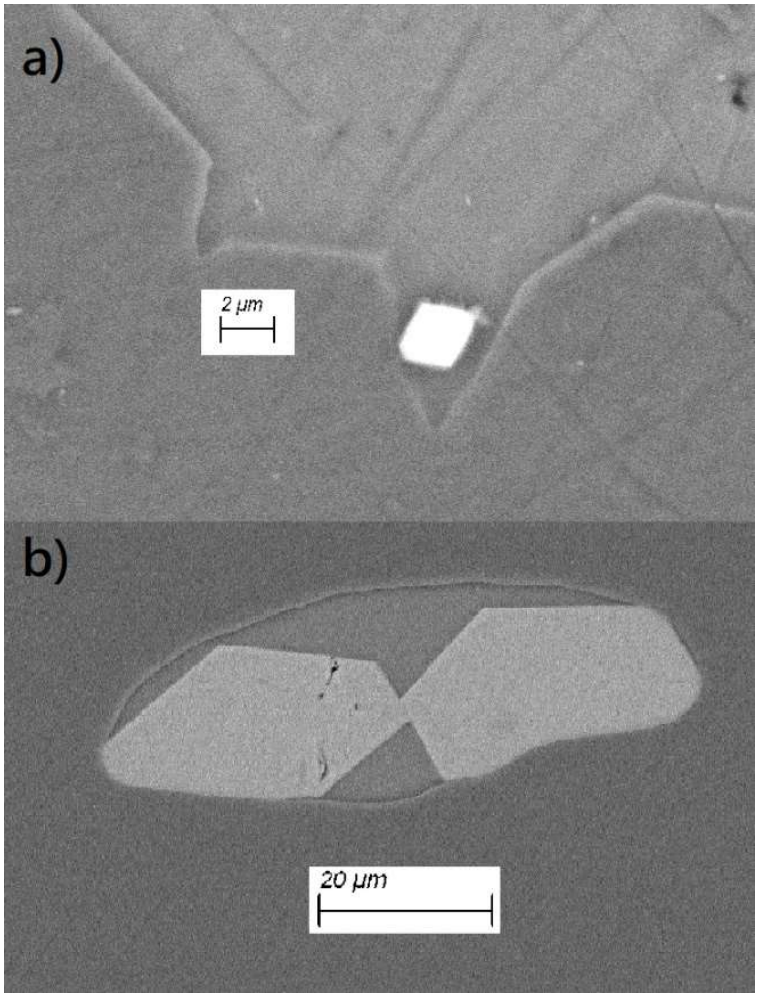

6.3.1 Major elements characterization

Chemical composition for FS and Vateliero MIs, after post-entrapment correction are reported in Table 3. Fig. 19, shows the plot of the MIs in the Total alkali vs silica (TAS) diagram, which classifies the melts entrapped in the FS olivine as basalt, with a low alkali content, similarly to the bulk rock. These products belong to the sub-alkaline series. Vateliero MIs are less primitive than FS, and they belong to the alkaline series and classify as trachy-basalt. Classification diagram for alkaline rock (Fig. 20a) [Ewart, 1982], characterize Vateliero MIs as an absarokite, a primitive shoshonite. The different nature of the two products does not allow K_2O use as a differentiation index between them.

Fig. 19. Total alkali vs silica (TAS) diagram [Le Bas et al., 1986] showing the composition of the studied melt inclusions. The purple line divides the alkaline (above) from sub-alkaline (below) products. FS MIs are sub-alkaline basalt; Vateliero MIs are almost all Trachybasalts.

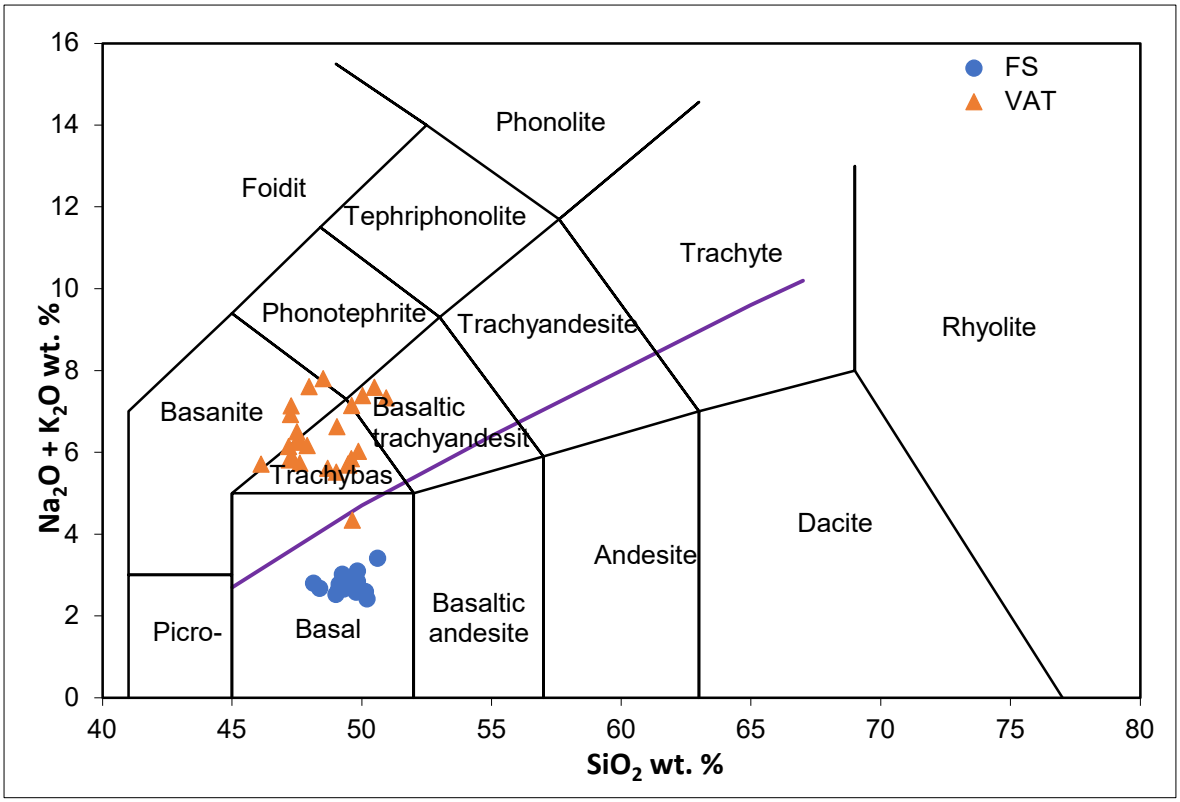

Melt inclusions show a narrow variability for FS eruption, in which MgO concentrations range between 11.11 and 13.21 wt%. These products are among the most-primitive materials that have been erupted at Mt. Etna, and also show the lowest Na_2O, K_2O, and SiO_2 contents [Kamenetsky et al., 2007]. In contrast, there is a large variability in the MgO content for Vateliero, which ranges between 4.28 and 9.48 wt%, and this variation is reflected in the Mg# of related host olivine. Olivines with lower forsterite number host less primitive melts as evident in Fig. 20b.

Fig. 20. a) Classification plot K_2O vs SiO_2 [Ewart. 1982]. Classification of alkaline products shows that MIs of Vateliero belong to absarokite composition, a primitive shoshonite. b) most primitive olivine hosts the most primitive MIs; this is shown by the clear correlation between MgO content of MIs and Mg# of relatives host olivine.

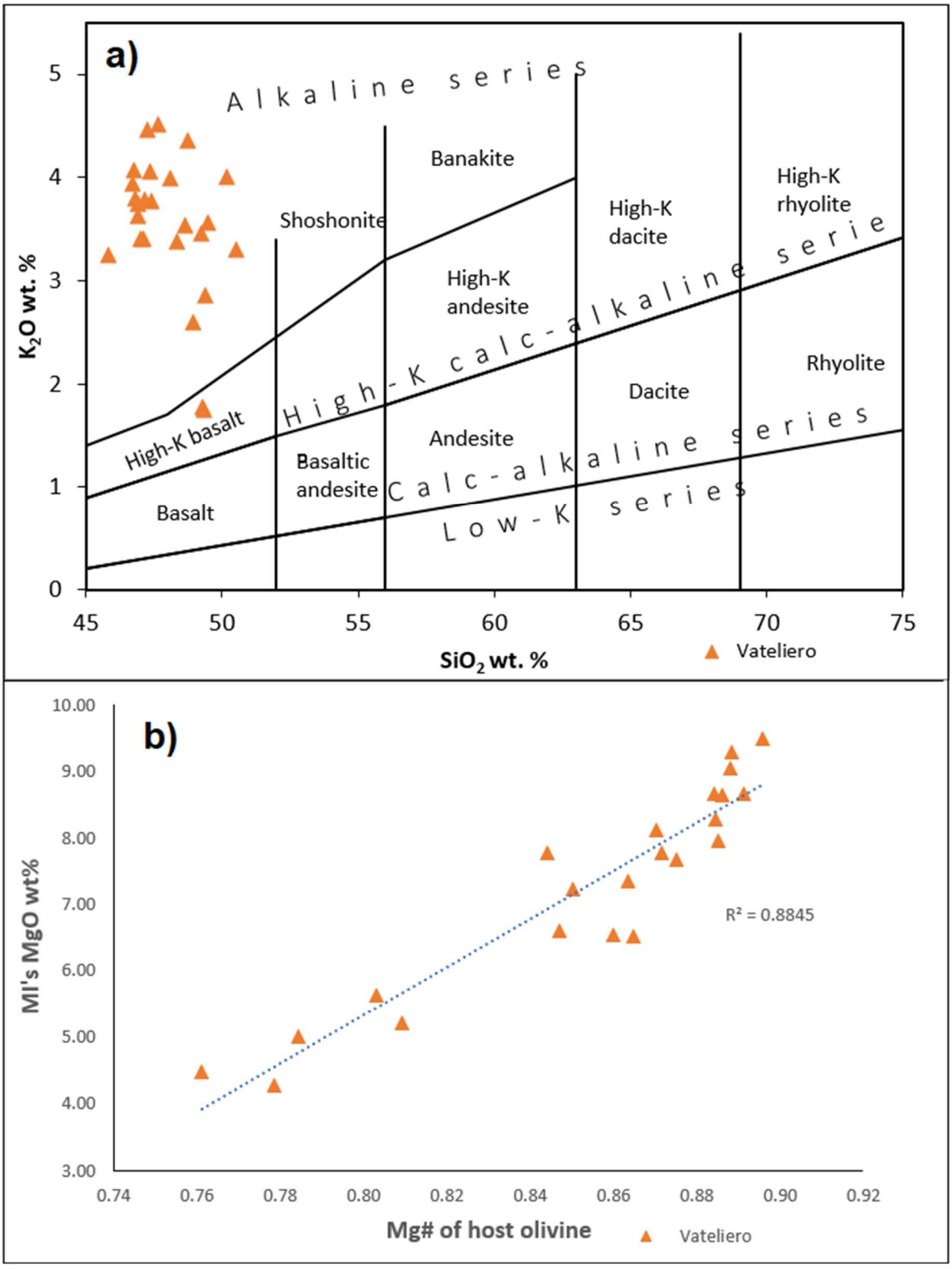

Tab. 3. Major elements composition for studied MIs expressed as wt%. Mg# = 100 · Mg/(Mg+Fe_{tot}); These compositions are corrected for post entrapment crystallization (as described in Appendix, paragraph A2).

	FS 01 melt	FS 02 melt	FS 03 melt	FS 04 melt	FS 05 melt	FS 06 melt	FS 08 melt	FS 11 melt	FS 12 melt
SiO_2	49.09	49.82	49.77	49.30	49.73	50.12	50.60	49.24	49.44
TiO_2	1.08	1.06	1.12	0.88	0.94	0.81	1.07	0.98	0.95
Al_2O_3	10.45	10.90	10.18	10.48	10.74	10.79	11.54	10.58	10.44
FeO	9.28	8.90	9.06	9.15	8.80	8.61	8.62	8.83	8.78
MnO	0.178	0.254	0.092	0.162	0.208	0.178	0.165	0.219	0.193
MgO	12.26	12.03	12.31	12.09	11.84	11.68	11.11	12.09	12.02
CaO	15.02	13.93	14.90	15.28	15.09	15.22	13.49	15.05	15.39
Na_2O	1.58	2.36	1.67	1.89	1.81	1.82	2.41	1.80	1.86
K_2O	1.07	0.74	0.92	0.77	0.84	0.78	1.00	1.22	0.93
Mg#	0.70	0.71	0.71	0.70	0.71	0.71	0.70	0.71	0.71
	FS 13 melt	FS 14 melt	FS 16 melt	FS 17 melt	FS 18 melt	FS 19 melt	FS 22 melt	FS 24 melt	FS 25 melt
SiO_2	49.11	49.75	50.19	48.99	50.04	49.81	49.57	48.36	48.13
TiO_2	0.86	0.86	0.91	0.91	0.99	0.94	1.08	0.96	0.98
Al_2O_3	10.77	11.18	10.71	10.28	10.86	11.25	10.62	10.89	10.26
FeO	8.96	9.01	9.11	9.30	9.01	8.91	9.29	9.49	9.55
MnO	0.120	0.111	0.233	0.180	0.147	0.220	0.194	0.223	0.133
MgO	12.52	11.57	11.27	12.47	11.48	11.89	11.66	12.15	13.21
CaO	14.88	14.76	15.17	15.36	14.89	14.13	14.89	15.25	14.93
Na_2O	1.75	1.67	1.61	1.81	1.76	1.66	1.81	1.63	1.76
K_2O	1.03	1.09	0.81	0.71	0.84	1.19	0.88	1.05	1.04
Mg#	0.71	0.70	0.69	0.70	0.69	0.70	0.69	0.70	0.71
	FS 26 melt	FS 28 melt	VAT 01 melt	VAT 02A melt	VAT 02B melt	VAT 03A melt	VAT 03B melt	VAT 04 melt	VAT 05 melt
SiO_2	49.68	49.30	47.11	48.67	48.35	47.14	46.81	50.56	48.92
TiO_2	1.15	0.95	1.50	1.07	1.27	1.35	1.16	1.74	1.48
Al_2O_3	11.06	11.13	15.34	16.03	16.29	14.53	15.30	16.94	15.43
FeO	8.73	9.06	7.57	7.12	6.87	7.86	7.92	9.34	7.27
MnO	0.144	0.291	0.157	0.123	0.174	0.130	0.134	0.173	0.116
MgO	12.17	12.13	8.63	7.95	7.61	9.06	9.30	4.48	8.28
CaO	14.34	14.27	13.00	12.88	13.20	13.05	12.52	8.77	11.76
Na_2O	1.95	1.93	2.28	1.93	2.21	2.43	2.29	3.98	3.05
K_2O	0.78	0.93	3.40	3.54	3.37	3.78	3.80	3.30	2.60
Mg#	0.71	0.70	0.67	0.67	0.66	0.67	0.68	0.46	0.67
	VAT 06 melt	VAT 07A melt	VAT 07B melt	VAT 08 melt	VAT 09 melt	VAT 10 melt	VAT 11 melt	VAT 12 melt	VAT 13 melt
SiO_2	48.72	47.68	47.28	49.32	47.44	49.47	49.40	47.36	45.84
TiO_2	1.11	1.93	1.89	1.13	1.46	1.88	1.48	1.02	1.41
Al_2O_3	14.67	18.32	17.48	15.71	16.53	17.15	15.65	14.74	16.87

FeO	7.28	8.34	9.61	7.60	8.09	8.52	7.80	7.54	9.70
MnO	0.160	0.115	0.146	0.156	0.142	0.113	0.106	0.150	0.103
MgO	8.67	4.28	5.00	7.67	7.36	5.19	7.76	9.48	7.76
CaO	12.18	9.98	9.68	13.48	11.96	9.29	10.92	12.91	12.08
Na_2O	2.23	3.15	3.04	2.57	2.34	3.75	3.12	2.15	2.43
K_2O	4.36	4.51	4.46	1.75	3.77	3.56	2.85	4.06	3.25
Mg#	0.68	0.48	0.48	0.64	0.62	0.52	0.64	0.69	0.59
	VAT 14A melt	VAT 15A melt	VAT 15B melt	VAT 16A melt	VAT 16B melt	VAT 17 melt	VAT 18 melt	VAT 19 melt	VAT 21 melt
SiO_2	48.10	46.77	46.72	49.30	46.89	46.98	46.90	50.15	49.26
TiO_2	1.26	1.62	1.73	1.41	1.21	1.24	1.37	1.82	1.13
Al_2O_3	16.72	17.70	17.43	17.32	16.01	16.51	15.58	16.99	16.69
FeO	7.34	9.52	9.64	7.54	8.53	8.82	7.84	7.13	8.25
MnO	0.117	0.158	0.208	0.125	0.117	0.230	0.178	0.110	0.145
MgO	6.52	5.63	5.60	7.42	8.12	7.23	8.67	6.51	6.60
CaO	12.27	10.74	10.46	10.84	12.73	12.47	12.79	9.09	11.47
Na_2O	2.76	2.78	3.10	3.89	2.14	2.38	2.09	3.53	2.35
K_2O	4.00	4.07	3.95	1.78	3.63	3.41	3.75	4.01	3.46
Mg#	0.61	0.51	0.51	0.64	0.63	0.59	0.66	0.62	0.59

6.3.2 Trace elements characterization

MIs trace elements concentration was determined using LA ICP-MS. MIs trace elements concentrations are many orders of magnitude higher than those in olivines, except for Ni, Cr, and Co. As for major elements composition, trace elements were corrected for post-entrapment crystallization. The calculation of corrected concentrations was obtained by applying a backward binary mixing calculation. Trace elements concentration of the host olivine were considered as the first end-member of the mixing, and the crystallized fraction for each melt was used to obtain the pristine MIs end-members. All corrected data are shown in Appendix Table A1.3 and Table A1.4.

V concentrations range between 236.43 and 283.45 ppm for FS MIs, and between 185.01 and 398.23 ppm for Vateliero MIs. The narrow concentration range for FS is related to the homogeneous compositions of MIs and relative host olivine. On the contrary, the largest concentration range of V in Vateliero MIs is given by the compositional gradient of these Mis due to their evolution, also reflected in the host olivine V content.

Rare earth elements (REE's) concentrations, normalized to chondrite REE values, show the typical pattern of mantle-derived products (Fig. 21). In order to exclude secondary processes of element fractionation due to hydrothermal complexation, the lanthanide tetrad effect [Bau, 1996; Irber, 1999; Niu, 2012] was computed to be negligible.

Fig. 21. FS and Vateliero MIs REE normalized to chondrite. These kinds of distribution patterns are common in primitive products. FS curves, which are below Vateliero curves, show that this melt is most primitive then Ischia melt.

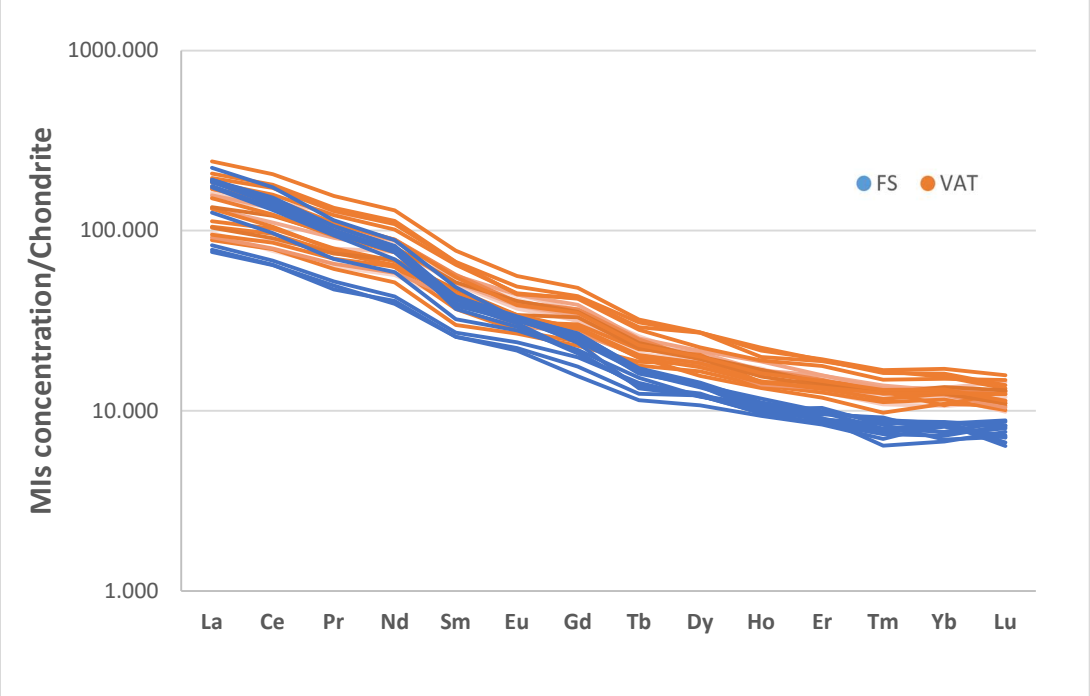

Elemental Y/Ho and Zr/Hf ratios confirm what the REE's patterns suggest. Y/Ho mean ratios are 25.6 ±1.7 and 26 ±1 for FS and Vateliero MIs respectively, while Zr/Hf mean ratios are 41.5 ±2.9 and 39.8 ±2.1 for FS and Vateliero Mis respectively. These trace elements ratios for MIs (Fig. 22) fall in the CHARAC FIELD (CHArge-and-Radius-Controlled behaviour [Bau, 1996]), therefore it allows to considered MIs unaltered from secondary processes.

Fig. 22. Y/Ho vs Zr/Hf for MIs. The CHARAC FIELD is the ratio range in which samples are not involved in secondary alteration processes. This data allows us to consider the studied MIs as unaltered.

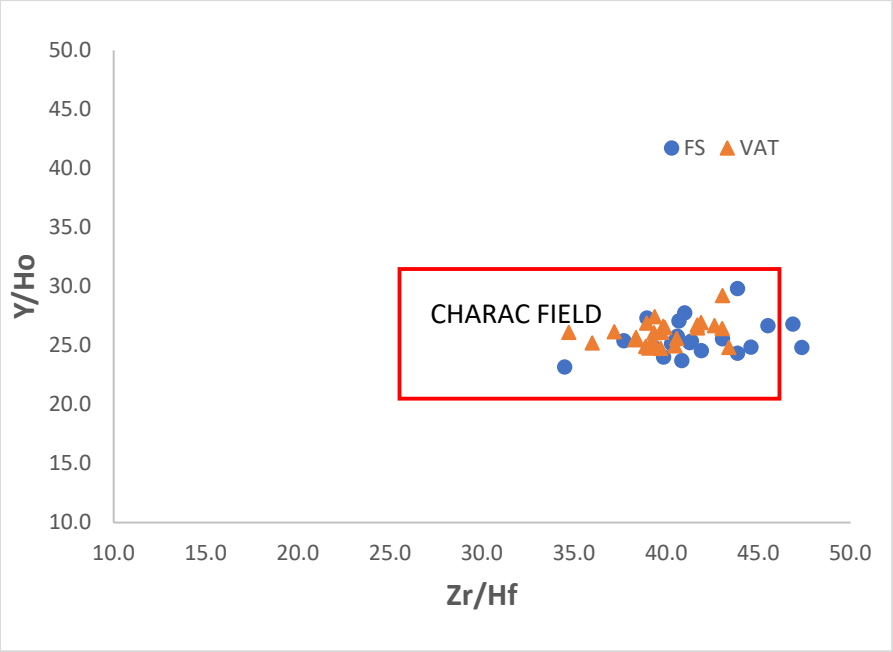

6.4 f_{O2} estimates

Oxygen fugacities for Mt. Etna and Ischia products were computed by using the methods previously described. While for Mt. Etna and Ischia we found many MIs where the methods involving melt composition could be applied, on the contrary, no Mis were found in olivine samples from Hyblean xenoliths. Due to MIs absence, redox state related to the ancient Hyblean mantle was computed based on mineral equilibria in the xenoliths, by using the free tool for mineral oxybarometer from the MELTS site.

6.4.1 Mt. Etna and Ischia f_{O2}

The redox estimates, computed from the D_V models, are shown in Table 4 for Mt. Etna and Ischia. Temperature and pressure, required for the redox models, were the following ones: for FS, a temperature of 1533 K was obtained by published data [Coltelli et al., 2005; Kamenetsky et al., 2007; Gennaro et al., 2019], and average pressure value of 0.3 (±0.1) GPa was extracted from the literature H_2O-CO_2 saturation models [Gennaro et al., 2019]; for Ischia the average temperature of 1485 K was computed using the olivine-liquid equilibrium thermometer from Putirka, 2008. For this calculation, the used average pressure of 0.2 GPa was extracted from Moretti et al., 2013.

The weight of pressure and temperature in the two used models for redox estimation is relatively low. A pressure variation of ±0.3 GPa determines a computed temperature variation of ±60 K. Moreover, a temperature variation of ±100 K determines a redox variation of ±0.15 QFM, which is within the standard deviation of computed redox.

Computed average redox values (as ΔQFM) for the FS eruption, are 2.43 ±0.24, 3.44 ±0.26, and 3.12 ±0.21 respectively for MON13, WANG19, and SHI18; Vateliero products average redox is 1.53 ±0.22, 2.79 ±0.29, and 2.23 ±0.28 respectively for MON13, WANG19, and SHI18 estimation model. The three models were applied to both eruptions, to observe any differences. However, the MON13 D_V-fO_2 model, which is calibrated on sub-alkaline basalts, is the most suitable model to analyse intraplate magmatism such as Mt. Etna (average ΔQFM = 2.43 ±0.24), while WANG19 D_V-fO_2 model, which is calibrated on alkaline basalts, is the most appropriate to investigate on Ischia (average ΔQFM = 2.79 ±0.29). Those obtained results are coherent with the literature.

Excluding a few results, due to probable analytical problems, the redox standard deviation for both eruptions is significantly low and within the method error range. FS olivine and MIs are chemically homogeneous, consequently, the redox estimation was expected to be about precise. Vateliero olivine and hosted MIs, which show an evolution gradient, has a similar standard deviation of FS.

Table 4. Redox estimates for the magmatic source of FS and Vateliero eruptions obtained D_V models.

ID	$D_V^{oliv/melt}$	Host olivine Mg#	ΔQFM (MON13)	ΔQFM (WANG19)	ΔQFM (SHI18)
FS 01	6.69E-03	0.90	2.62	3.70	3.36
FS 02	8.51E-03	0.90	2.35	3.32	3.02
FS 03	7.81E-03	0.90	2.41	3.44	3.14
FS 04	7.34E-03	0.90	2.51	3.56	3.23
FS 05	6.57E-03	0.90	2.74	3.77	3.38
FS 06	6.62E-03	0.90	2.76	3.76	3.37
FS 08	8.17E-03	0.90	2.50	3.44	3.08
FS 22	9.25E-03	0.90	2.17	3.19	2.90
FS 24	7.49E-03	0.90	2.41	3.51	3.20
FS 26	1.05E-02	0.90	2.00	2.95	2.72
FS 28	8.96E-03	0.90	2.22	3.22	2.95
FS means			2.43 (±0.24)	3.44 (±0.26)	3.12 (±0.21)
VAT 01	1.19E-02	0.89	1.67	3.01	2.55
VAT 02A	1.19E-02	0.89	1.84	3.11	2.54
VAT 02B	1.25E-02	0.89	1.76	3.07	2.47
VAT 03A	1.19E-02	0.89	1.51	2.96	2.55
VAT 03B	1.53E-02	0.89	1.14	2.49	2.18
VAT 04	2.18E-02	0.76	1.49	2.50	1.68
VAT 05	1.87E-02	0.88	1.18	2.29	1.90
VAT 06	1.29E-02	0.89	1.43	2.86	2.43
VAT 07A	1.85E-02	0.78	1.46	2.82	1.92
VAT 07B	1.54E-02	0.78	1.64	2.99	2.18
VAT 08	1.74E-02	0.87	1.50	2.51	2.00
VAT 09	1.61E-02	0.86	1.32	2.64	2.12
VAT 11	2.00E-02	0.87	1.13	2.23	1.81
VAT 12	1.14E-02	0.90	1.55	2.97	2.60
VAT 13	1.33E-02	0.84	1.66	2.91	2.39
VAT 15A	1.35E-02	0.80	1.80	3.18	2.36
VAT 15B	1.44E-02	0.80	1.69	3.08	2.27
VAT 21	1.49E-02	0.85	1.86	2.65	2.23
VAT 16B	1.48E-02	0.87	1.77	2.79	2.47
VAT 17	1.25E-02	0.85	1.44	2.90	2.38
VAT 18	1.33E-02	0.88	1.06	3.05	1.74
VAT 19	2.10E-02	0.86	1.69	2.29	2.22
VAT means			1.53 (±0.24)	2.79 (±0.29)	2.23 (±0.28)

The f_{O2} estimation from Zn/Fe_T and FeTiMM oxybarometers [Lee et al., 2010; Arató and Audétat, 2017] show different and not reasonable results. The oxybarometer based on Zn/Fe_T ratio leads in fact to an extremely high oxidation state for FS. The average computed redox value for FS eruption is ΔQFM = 7 ±0.3, which is not realistic in a natural magmatic system. This oxybarometer does not lead to coherent redox estimates also for

the Vateliero eruption, where it achieves a reduced condition for Vateliero with respect to calculated value using all D_V models. Similarly, Zn/Fe_T ratio leads to an average redox value of QFM +0.8 ±0.6 for Vateliero, which is sharply lower than our previous estimations base on D_V and also lower with respect to literature data [>QFM+2 Moretti et al., 2013;], therefore it was not considered as reliable.

FeTiMM oxybarometer was applied on eleven Vateliero samples, in which oxides were found within MIs. It must be pointed out that analyzed oxides are mainly Cr-spinel and chromiferous-magnetite, therefore FeTiMM oxybarometer was not applied within the calibrated conditions described in Arató and Audétat, 2017. The computed average redox is attested to ΔQFM = 5.4 ±2.3, which is not realistic to a natural magmatic source. FeTiMM oxybarometer could not be applied to FS, due to the absence of oxides within analysable MIs.

6.4.2 f_{O2} of Hyblean magmatic source

As described above (chapter 5.2.) chemical composition of spinel peridotites have been taken from Perinelli et al., 2008. Hyblean spinel peridotites were investigated using a mineral oxybarometer tool from the MELTS website.

The computed redox state of the Hyblean magmatic source was based on eight samples (HYB14, HYB 21, HYB 23, HYB 24, HYB29, HYB34, HYB 36, HYB 40. [Perinelli et al., 2008]). Calculated average redox state reveals a reduced source, attested at ΔQFM = -0.96 ±0.82. This result falls within the common range of primitive mantle. Due to a more updated thermodynamic dataset in MELTS tool, our result is different from the calculated redox of Perinelli et al., 2008, which describes a more oxidized source at ΔQFM ≈ +1.

7 Discussion

Mt. Etna and Ischia volcanism belong to two different geodynamical environments, respectively intraplate and subduction-related magmatism. The calculation of the redox state for the two volcanic systems varies according to the used methodology.

As described in chapter 6.4.1, we computed ΔQFM = 2.4 ±0.24 and ΔQFM = 2.7 ±0.4 for Mt. Etna and Vateliero respectively. These results can be interpreted within the given geodynamical framework and literature data (Fig. 23). Our computed redox conditions for Mt. Etna agree with most of the previous data on this volcano. Redox values of Ischia fall within the large range described in Moretti et al., 2013. As expected for subduction-related magmatism, and according to previous literature, the redox state of Ischia is attested to high-oxidized values.

Since we used high Mg# products (Fo_{90} for almost all the FS samples, and Fo_{88-99} for the most primitive samples of Vateliero), it is possible to consider our samples primary melts produced by melting of the mantle source. Also, if assuming batch melting processes at solid-melt equilibrium, then the computed redox values of studied products can be regarded as those of the mantle source that generated FS and Vateliero lavas. In the case of Ischia, we also recall that the evolved olivines return the same redox conditions of the least evolved ones, suggesting that the magma fractionation did not modify the redox of the residual melts.

About Hyblean magmatism, we studied spinel peridotites from Perinelli et al., 2008. In this case, we have a direct value of mantle obtained by mineral-oxybarometers. We calculated an average redox state of ΔQFM = -0.96 ±0.82. This result falls within the common range of lithosphere mantle. The computed Hyblean xenoliths redox state is close to the average redox of common upper mantle (QFM -0.7/-1) [Foley, 2012], and fall within the range for subcontinental lithospheric mantle (QFM ±1) [Wood et al., 1990]. The large heterogeneity of Hyblean mantle [Scribano et al., 2008; Correale et al., 2012] can explain the high variability in the redox values. A metasomatic agent more oxidized than the host mantle, which provides heterogeneous oxidation of the mantle is suggest from Perinelli et al., 2008. In particular, two distinct metasomatic agents have been recognized: A silica alkaline melt similar to the host basalt of xenoliths, and a hawaiitic melt not related to the host basalt, found as glass veins within xenoliths [Perinelli et al., 2008]. This metasomatized melt also oxidized the upper mantle, increasing the fO_2 above QFM.

Literature micro-thermometric analyses on these xenoliths show entrapment pressure of fluid inclusions in the range of 0.75-0.95 GPa, corresponding to a depth of 27-35 km, which fall within the depth range where spinel peridotites would be stable [Sapienza et al., 2005]. Due to this evidence, we can place Hyblean xenoliths in the graph shown in Fig. 24. In this extended version of the graph from Eguchi et al., 2018, the Hyblean xenoliths fall close to the EMOG/D, the common feature of a peridotitic continental lithosphere.

Fig. 23. In this picture our redox estimates for Mt. Etna and Ischia island using D_V-fO_2 models, and of recalculated redox of Hyblean literature xenolith, using mineral-oxybarometer, are compared to estimations of previous studies [Carmichael et al., 1991; Kamenetsky and Clocchiatti, 1996; Parkinson and Arculus 1999; Lee et al., 2005; Perinelli et al., 2008; Evans et al., 2012; Moretti et al., 2013., Brounce et al., 2014; Mollo et al., 2015; Martin et al., 2017; Zhang et al., 2018].

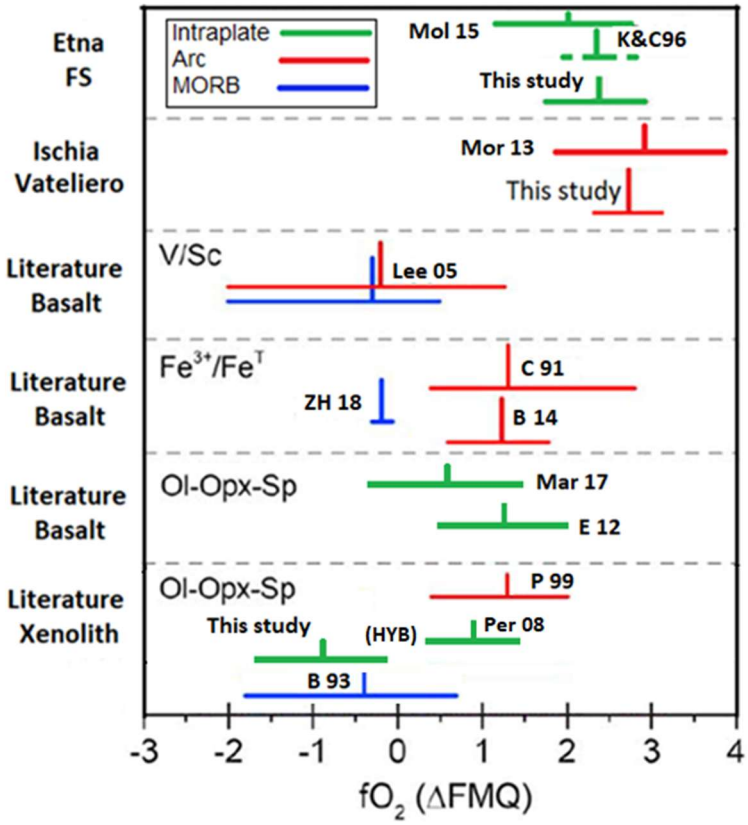

Fig. 24. Modified Fig. 19. Hyblean spinel peridotite xenoliths are positioned between the extended EMOG/D (graphite/diamond transition in peridotite) and DCDG/D (graphite/diamond transition in eclogite/pyroxenite rocks) lines.

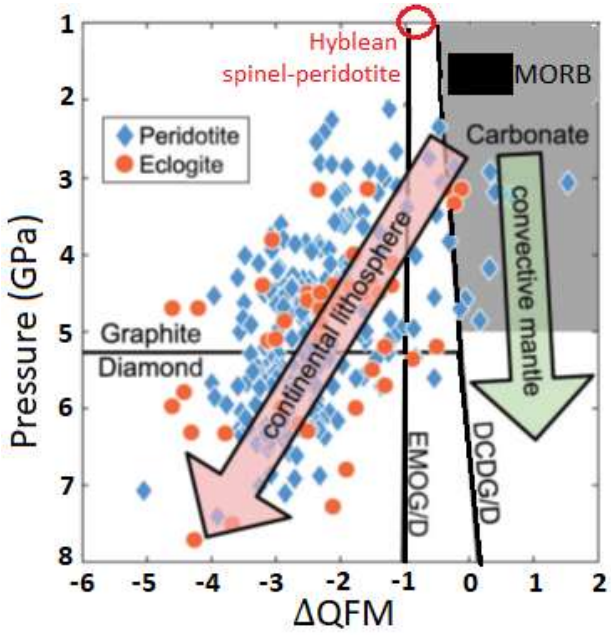

Metasomatic events are easily taken into account in the arc environment, such as Ischia, but as shown in literature, ancient subduction define a strong heterogeneity in the upper mantle [Gaillard et al., 2015], and also intraplate magmatic source can be affected by past metasomatic events which oxidized the upper mantle [Martin et al., 2017]. To consider the possibility of metasomatic events, a metasomatic fluid injection within the magmatic source was investigated. Trace elements ratios in melt inclusions, where a fluid-mobile element is related to a fluid-immobile element (such a Ba/La, or Rb/La), allows hypothesizing the presence of metasomatic fluid. These ratios clearly correlate with the redox state, as shown in Fig. 25. Specifically, lower Ba/La ratios are indicative of an insignificant to low input of fluids, on the contrary, higher Ba/La ratios are related to fluid injection and metasomatism. Mt. Etna calculated average Ba/La ratio is 12 ±1.8, which slightly overlap in the range where is assumed very low subduction inputs occurs [Brounce et al., 2014; Kelley and Cottrell, 2009], while greater and wide range ratio on Ischia products leads to speculate on higher fluid inputs.

Fig. 25. Ba/La vs computed redox state of all Etna and Ischia samples. Considering Ba/La as crustal fluids input proxy, it is allowed the hypothesis of fluids contamination, which determines the higher oxidation of the magmatic source respect to the common lithospheric mantle.

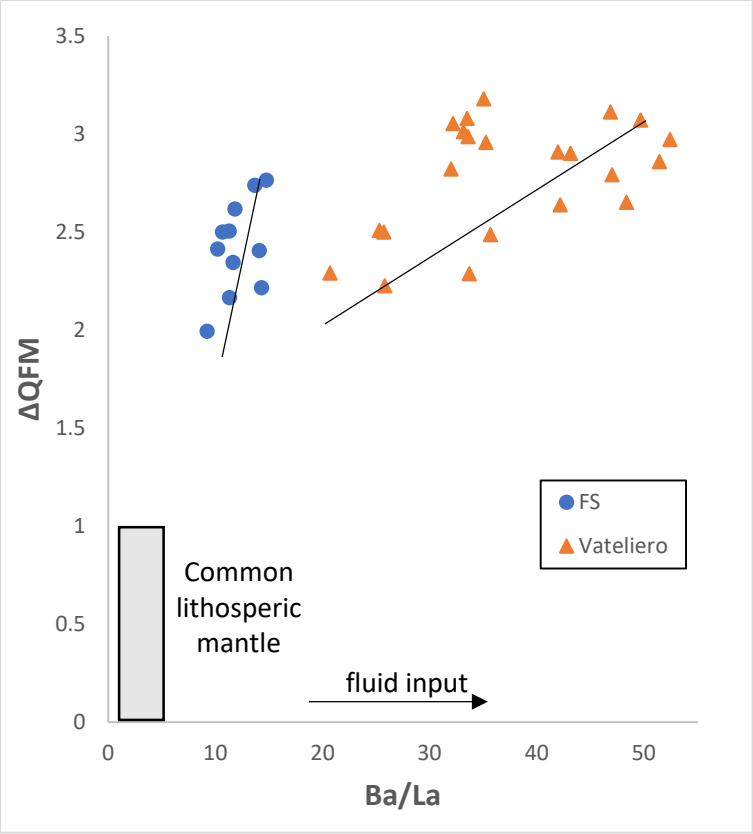

Before assuming that higher Ba/La ratios are indicatives of metasomatic fluids injection, it is necessary to better understand if this ratio can be affected by other processes, such as crystallization. In Fig. 26a is plotted La vs Sm, as a common crystallization proxy, which reveals that our sample shows a few degrees of crystallization. To understand how Ba/La ratios are affected by the crystallization process

and partial melting, calculated fractional crystallization and partial melting models are shown in Fig.26b (fractional crystallization and batch partial melting models furthers details are in Appendix A3). These curves show how crystallization strongly increase La/Sm ratios, while Ba/La is poorly modified from it, and partial melting slightly decrease Ba/La ratios and poorly modified La/Sm. Therefore, we can assume that Ba/La ratios variability in our samples, does not depends on these few degrees of crystallization or partial melting but it is only related to source features.

Fig. 26. a) Sm vs La concentration plot. For both Etna and Ischia samples, this alignment shows few degrees of crystallization processes. b) Crystallization and melting curves in La/Sa vs Ba/La plot. During the crystallization of mafic melts, the La/Sm ratio grown of several points, while Ba/La remains almost constant. The wide range of Ba/La for Ischia melts cannot be explained with crystallization processes, but with external fluids inputs.

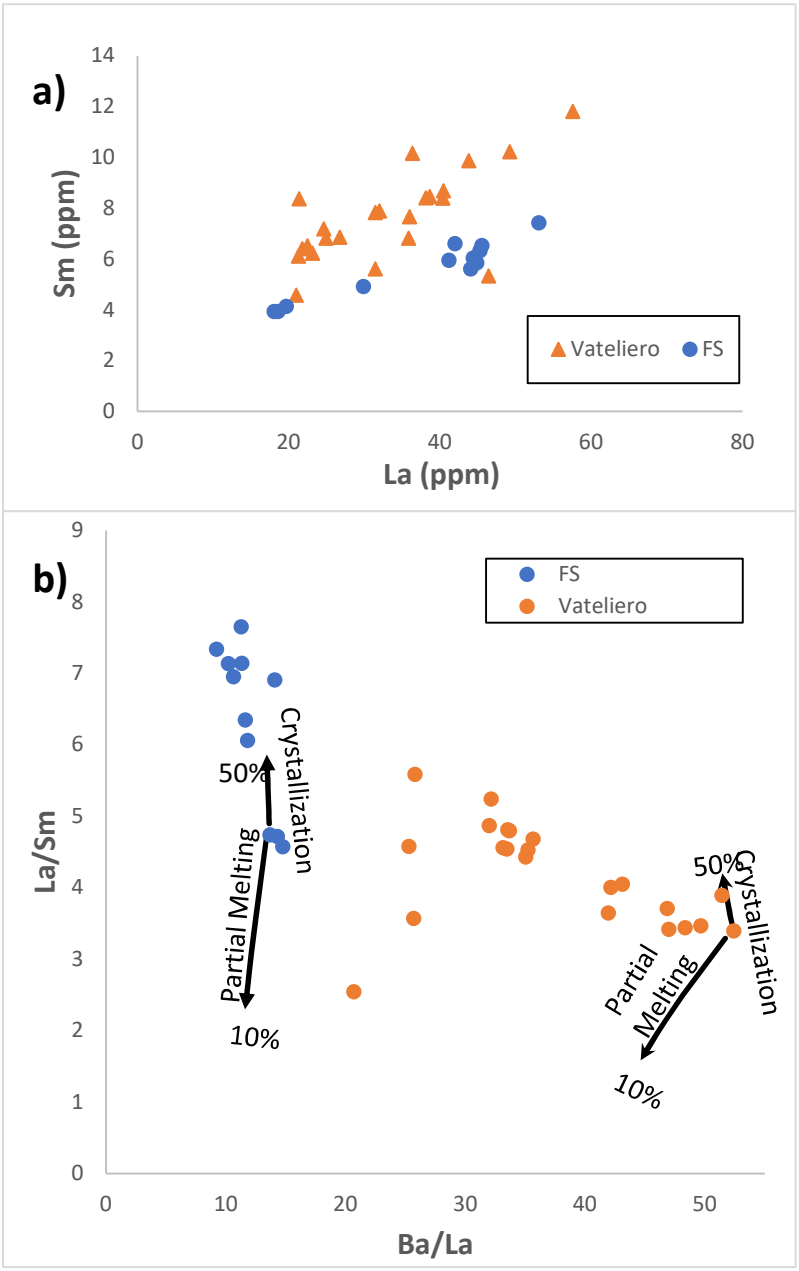

To estimate the metasomatic fluid input on the magmatic source, we assumed a binary mixing model of the uncontaminated mantle source with a metasomatic fluid.

The binary mixing equation (Eq.10) was used to model a theoretical Ba/La trend within samples at different fluid fraction (X_f) addition (Fig. 27). For the metasomatic fluid, we considered an H_2O-rich subduction component of oceanic crust with the contribution of fluids from sediments, with $[Ba]_f$ = 5000 ppm and $[La]_f$ = 90 ppm [Johnson et al., 2009]. The assumed pristine mantle end-member is the average depleted MORB mantle (DMM) with $[Ba]_{DMM}$ of 0.563 ppm and $[La]_{DMM}$ = 0.192 ppm [Workman et al., 2005].

Eq.10

$$\frac{[Ba]^{Samp.}}{[La]} = \frac{[Ba]_{DMM} \cdot (1 - X_f) + [Ba]_f \cdot X_f}{[La]_{DMM} \cdot (1 - X_f) + [La]_f \cdot X_f}$$

The Eq.10 was rearranged to compute the fluid fraction which must be added to the uncontaminated DMM, to obtain the Ba/La ratio in our samples:

$$([La]_{DMM} \cdot (1 - X_f) + [La]_f \cdot X_f) \frac{[Ba]^{Samp.}}{[La]} = [Ba]_{DMM} \cdot (1 - X_f) + [Ba]_f \cdot X_f$$

$$[La]_{DMM} \cdot \frac{[Ba]^{Samp.}}{[La]} - [La]_{DMM} \cdot X_f \cdot \frac{[Ba]^{Samp.}}{[La]} + [La]_f \cdot X_f \frac{[Ba]^{Samp.}}{[La]} = [Ba]_{DMM} - [Ba]_{DMM} \cdot X_f + [Ba]_f \cdot X_f$$

$$[Ba]_{DMM} \cdot X_f - [Ba]_f \cdot X_f - [La]_{DMM} \cdot X_f \cdot \frac{[Ba]^{Samp.}}{[La]} + [La]_f \cdot X_f \frac{[Ba]^{Samp.}}{[La]} = [Ba]_{DMM} - [La]_{DMM} \cdot \frac{[Ba]^{Samp.}}{[La]}$$

$$X_f \left([Ba]_{DMM} - [Ba]_f - [La]_{DMM} \cdot \frac{[Ba]^{Samp.}}{[La]} + [La]_f \cdot \frac{[Ba]^{Samp.}}{[La]} \right) = [Ba]_{DMM} - [La]_{DMM} \cdot \frac{[Ba]^{Samp.}}{[La]}$$

$$X_f = \frac{[Ba]_{DMM} - [La]_{DMM} \cdot \frac{[Ba]^{Samp.}}{[La]}}{[Ba]_{DMM} - [Ba]_f - [La]_{DMM} \cdot \frac{[Ba]^{Samp.}}{[La]} + [La]_f \cdot \frac{[Ba]^{Samp.}}{[La]}}$$

Calculated X_f %, for each sample are reported in Table 5. and shown in Fig. 26. The calculated fluid fraction which must be added to the intraplate Mt. Etna magmatic source is <0.1%, with an average of 0.04% and a low standard deviation (0.01%), while, for the arc magmatic source of Ischia the fluid fraction up to 0.73% (±0.79%).

The fluid fraction was also calculated using Rb/La. Excluding three samples from the Etna dataset (FS 01, FS 06, and FS 28), the resulting average 100%· X_f is 0.04% (±0.02%) for Etna, while the calculated average fraction fluid for Ischia is 0.3% (±0.6). For Ischia, this value is lower than calculated using Ba/La but always greater than one order of magnitude respect to Etna magmatic source. Ba/La vs Rb/La plot (Fig. 28) shows a great correlation between these ratios for both studied products. In the plot, Vateliero is aligned with FS, allowing to support the hypothesis that both magmas started from a similar mantle, DMM-like.

The presence of a metasomatic fluid in the Etna mantle has also been hypothesized by Correale et al., 2014. In this mentioned study, the authors shown inconsistencies given by Sr and Nd isotopic ratios heterogeneity. To investigate these inconsistencies, they evaluated the combined effects of metasomatism and mantle melting on magma geochemistry by simulating a mixing between the least-contaminated Etnean mantle source with variable amounts of a metasomatic aqueous fluid. The result of this investigation shows that FS melt is produced from a fluid-contaminated mantle.

As evident from Fig. 25, the added fluids had a different potential in modifying the redox conditions of the mantles. Etna and Ischia, in fact, fall along two different linear trends and the highest gradient of Etna linear trend, compared to that of Ischia (Fig. 25), prove that the fluids added to Etna mantle are more oxidizing than those added to Ischia mantle. This evidence can be explained by two opposite scenarios. In the first one, we assume two fluids with similar Ba/La ratio. Indeed, this is the assumed condition in the above estimations of the percentages of the added metasomatic fluids to mantle. In this case, the metasomatic fluids of Ischia and Mt Etna has to exhibit different contents in the major oxidizing species and/or multivalent cations, such as sulphate and ferric iron, making the two metasomatic fluids able to produce different oxidizing conditions at equal added fraction. On the contrary, in the second instance the two fluids had a similar redox-capacity, and then Ba/La ratio of the two fluids must be different from each other. However, these are the two borderline cases, but reality probably represents an intermediate case between the two described scenarios, in undefined percentages.

Table 5. Compute fluid fraction (as %) for each MIs. The average value shows that a very small fraction of fluids is needed in Etna melts, to produce the increase of Ba/La ratio, while more fluids are added in the mantle to produce Ischia magmas.

	X_f		X_f		X_f		X_f		X_f		X_f
FS 01	0.04	FS 08	0.04	VAT 01	0.29	VAT 05	0.11	VAT 11	0.16	VAT 17	1.08
FS 02	0.04	FS 22	0.04	VAT 02A	1.06	VAT 06	2.44	VAT 12	3.22	VAT 18	0.68
FS 03	0.06	FS 24	0.03	VAT 02B	1.65	VAT 07A	0.26	VAT 13	0.61	VAT 19	0.27
FS 04	0.04	FS 26	0.03	VAT 03A	0.34	VAT 07B	0.30	VAT 15A	0.33	VAT 21	0.30
FS 05	0.05	FS 28	0.06	VAT 03B	0.35	VAT 08	0.16	VAT 15B	0.29		
FS 06	0.06			VAT 04	0.16	VAT 09	0.62	VAT 16B	1.32		
Average FS	0.04 ±0.01			Average VAT	0.73 ±0.79						

Fig. 27. Mixing model between the DMM and the modelled crustal fluids. Calculated fluid fraction for Etna and Ischia are plotted on the curve. Ischia mantle source is the most contaminated from crustal fluid, as expected for arc mantle. We can also recognize very small contamination of the Etnean mantle; with an average fluid input of 0.04%, it is possible to oxidize the pristine DMM mantle to the actual.

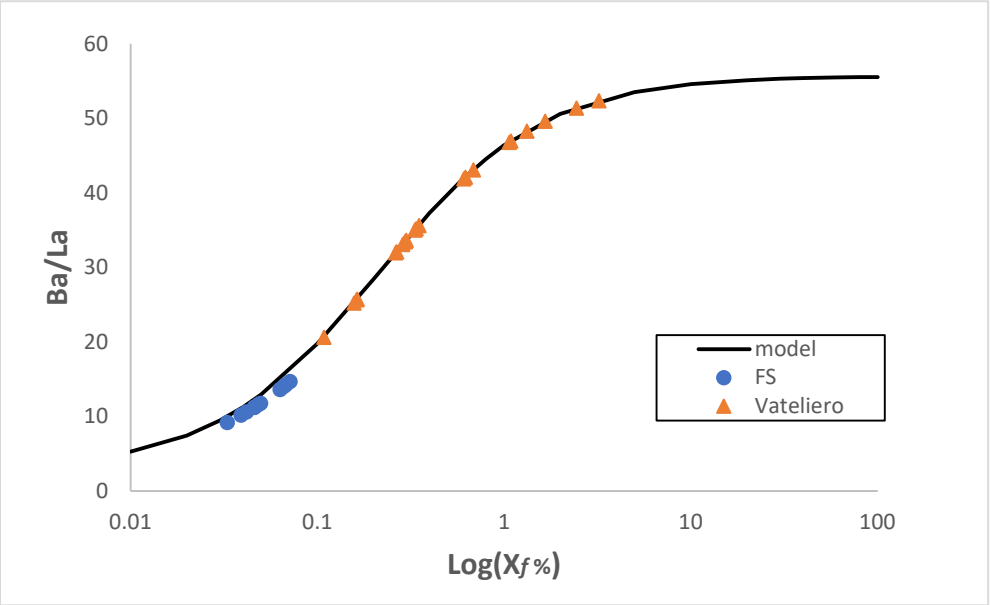

Fig. 28. Ba/La vs Rb/La on Etna and Ischia samples show a good correlation. The alignment allows to consider the two melts as produced from the same starting mantle, and the different final products are due to different input amounts of similar fluids.

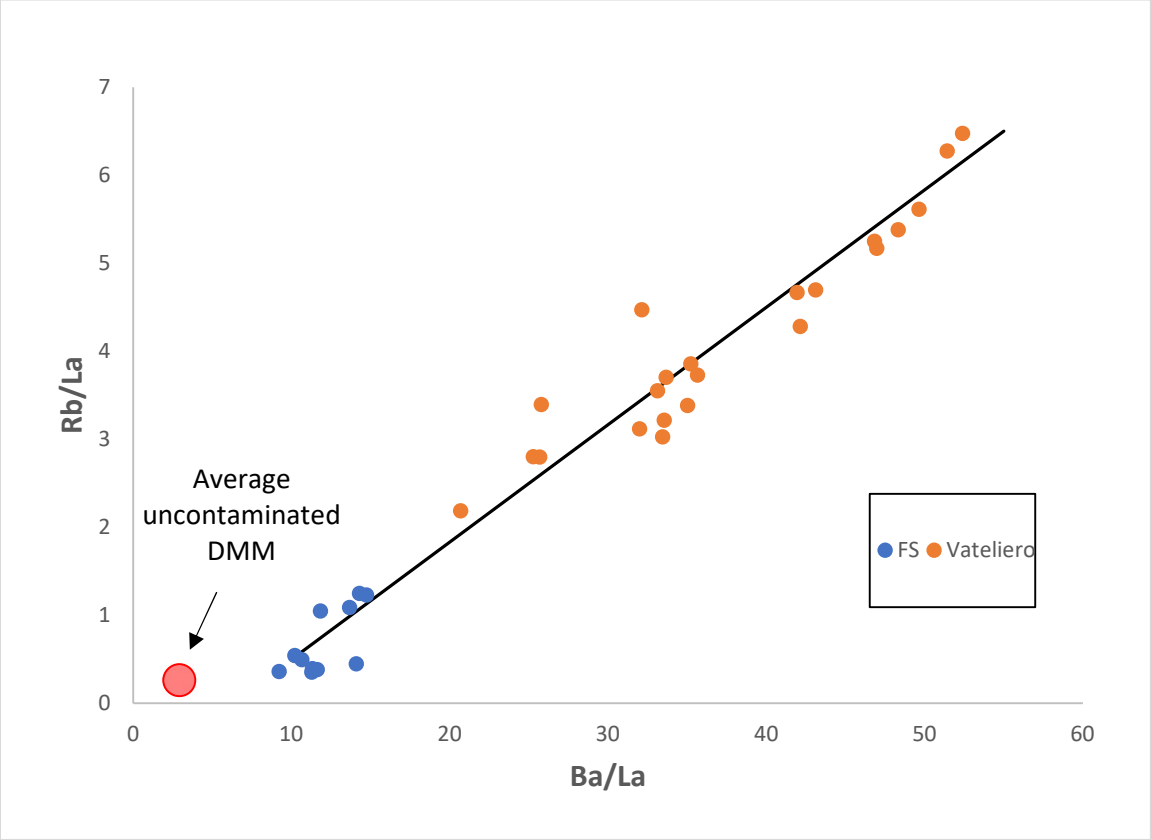

The plot of La/Sm vs Ba/Nd (Fig. 29) [Langmuir et al., 2006; Escrig et al., 2009] allows some further inferences regarding the characteristic of the fluid contamination of the studied products. The relationships between these two geochemical pairs highlight the different nature of the contaminants.

For Ischia there is a clear and marked tendency to a subduction-linked contamination. Moreover, this contamination can be mainly attributed to subducted sediments melt, and to a lesser extent to slab-fluids. On the other hand, Etna magmatic source shows a different kind of contamination. The highest La/Sm ratio and lower Ba/Nb ratio highlight a complex pattern where the contribution of Enriched mantle components together with subduction-related inputs give peculiar signatures to the local upper mantle.

Fig. 29. La/Sm vs Ba/Nd diagram from Escrig et al., 2009 with our Etna and Ischia MIs trace ratio plots. Higher Ba/Nb values are proxy for subduction materials input into the magmatic source, while high La/Sm with low Ba/Nd are indicatives of mantle enrichment.

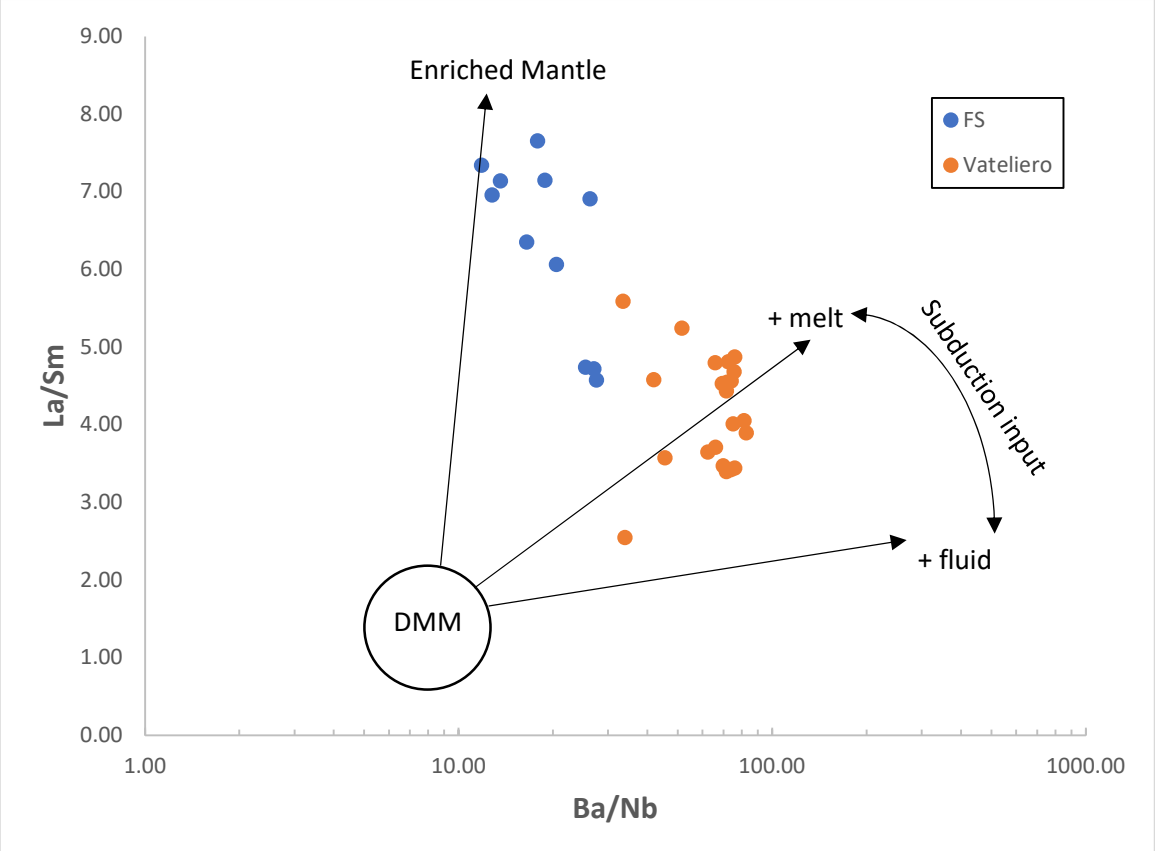

As a conclusion, it is clear that the intraplate and subduction-related volcanism share a similar pristine mantle source, before the beginning of mantle dynamics and contribution of subduction-related materials.

In the Mt. Etna case, we report an unusual highly oxidized system, as also reported by numerous studies [Métrich et al., 2009; Liotta et al., 2012; Gennaro et al., 2019]. In the hypothesis of the Hyblean mantle as the local mantle previous to the onset of the volcanism of Etna, metasomatic processes occurred that caused mantle oxidation above the Hyblean redox conditions, and also above the common intraplate mantle. In particular we support the hypothesis of few degree of fluid-driven metasomatism. The

involvement of a fluid metasomatizing phases has been suggested by several authors [e.g. Kamenetsky and Clocchiatti, 1996; Tonarini et al., 2001; Correale et al., 2014; Corsaro and Métrich, 2016], which address to a contribution of a crustal slab-derived component in the magmatic mantle source of the Etna activity in the last 15 ka. But even, it is plausible the hypotheses of mantle enrichment beneath Mt. Etna. Many studies support the enriched signature due to the mixing of HIMU end-member and a second mixed component of EM and DMM source [Schiavi et al.,2015], or also the HIMU-like Hyblean peridotite and a pyroxenite (DMM-like) [Correale et al., 2012]. All of these evidences that we know about Etna describes a truly complex systems, where it is not easy to define a unique mechanism for the production of its oxidized melts.

In the Ischia case, with the usual progress of the fluids and melts input from the slab in arc environment, the mantle suffered in fact changes in trace element composition and oxygen fugacity. Nevertheless, this process did not involve all the mantle source but it occurred patchily, with more affected portions and others less changed. This conclusion supports the hypothesis that mantle wedges affected by subduction-related fluids become really oxidized with respect to MORB mantles. Besides the effects due to magma evolution, we thus address to the different redox state of intraplate and arc primary magmas, and consequently their mantle source.

8 Conclusions

In order to improve the knowledge of the redox state of the Earth's mantle for different geodynamic settings, we have carried out a melt inclusion study, with the application of numerous oxybarometers.

Olivine hosted melt inclusions were accurately selected from Mt. Etna and Ischia most primitive products (FS and Vateliero respectively). Olivines and melt inclusions were characterized for their major elements and trace elements composition by electron microprobe, and LA ICP-MS. V-oxybarometer from Mallmann and O'Neill, 2013 and Wang et al., 2019 were those models that have determined the most coherent redox state for Mt. Etna and Ischia respectively in relation to previously available literature data and geodynamical context.

Here the principal remarks obtained from this research:

- The redox state of Hyblean magmatism was recalculated using mineral-oxybarometry on mantle xenoliths reported in literature. We used an olivine-orthopyroxene-Spinel online oxybarometer tool with updated thermodynamic parameter. We computed a redox ΔQFM = -0.96 ±0.82, which is coherent with a common lithospheric mantle.

- Vanadium oxybarometry is a robust tool for redox compute of magmatic products. In these cases, due to the great variations between the different geodynamic systems, it is important to use a strictly calibrated method for the type of product to be analyzed. These oxybarometers are almost insensitive to few degree of crystallization, and little temperature variation (a variation of about 50K show a redox variation smaller than the model error).

- The computed redox state for Mt. Etna, show an unusual highly oxidized system (ΔQFM = 2.4 ±0.24). If we consider the Hyblean mantle as the oldest mantle on which subsequent volcanism of Etna was based, some oxidation processes occurred. These processes rose the redox conditions above the Hyblean redox conditions, and also above the common intraplate mantle.

- The computed redox state for Ischia of ΔQFM = 2.7 ±0.4, fall within the range of common subduction-related environment. This oxidated system is well coherent with the input of slab-derived fluids, which are taken into account during subduction.

- While is generally accepted that arc basalts fO_2 is strongly correlated with fluid input, our study indicate that oxidation of mantle is intimately related to fluid input even in intraplate environments. We reported geochemical evidences of fluid input in the Etnean mantle. This can be oxidation process that rose the

redox state from a common lithospheric mantle up to the conditions we computed.

This work offers a global perspective on the heterogeneity of the oxidation state of mantle due to crustal fluid input, but do not exclude the presence of other processes.

We believe that our results could help on better understanding the complex and uncommon oxidated Etnean magmatic source.

This PhD work could be useful to estimate the redox state of petrological products with geochemical techniques, in particular when mineral-oxybarometry cannot be applied due to the absence of required mineral phases.

ACKNOWLEDGMENTS

Firstly, I would like to express my sincere gratitude to my tutors and co-tutor, Prof. Paolo Censi (Università degli Studi di Palermo), and Dr. Antonio Paonita (I.N.G.V. sez. Palermo), for their constant support, guidance, and precious advice over the three years of my doctorate.

I express my gratitude to Dr. Alessandra Correale (I.N.G.V. sez. Palermo), and Dr. Ilenia Arienzo (I.N.G.V. sez. Napoli Osservatorio Vesuviano) for providing the starting products, without which I would not have obtained the results presented in this thesis.

I am very grateful again to Dr. Alessandra Correale (I.N.G.V. sez. Palermo), and Dr. Emanuela Gennaro (Università degli Studi di Palermo), for their technical assistance during samples preparation, and who taught me the whole practical procedure.

I would like to thanks Dr. Giada Iacono-Marziano (I.S.T.O, Orléans) for personally hosted me, and the fundamental help for the SAM and EMPA analyzes. I also thank her and Dr. Marco Viccaro (Università di Catania) for their referee contribution; their indications have been useful to add important ideas and complete the thesis work.

I would like to thanks my lovely family and Roberta for their endless support.

References

Alonso-Perez R., Müntener O., Ulmer P. (2009). *Igneous garnet and amphibole fractionation in the roots of island arcs: Experimental constraints on andesitic liquids.* Contributions to Mineralogy and Petrology 157, 541–558.

Alt, J.C., Garrido, C.J., Shanks III, W.C., Turchyn, A., Padrón-Navarta, J.A., Sánchez-Vizcaíno, V.L., Gómez Pugnaire, M.T., Marchesi, C. (2012). *Recycling of water, carbon, and sulfur during subduction of serpentinites: a stable isotope study of Cerro del Almirez, Spain*. Earth and Planetary Science Letters 327, 50–60.

Amore, C., Carveni, P., Scribano, V., Sturiale, C. (1988). *Facies ed età del vulcanismo nella fascia sudorientale della Sicilia (Pachino-Capo Passero).* Bollettino della Societa Geologica Italiana 107, 3–4.

Arató, R., Audétat, A. (2017). *FeTiMM – A new oxybarometer for mafic to felsic magmas.* Geochemical Perspectives Letters 5, 19-23

Arculus, R.J. (1994). *Aspects of magma genesis in arcs*. Lithos 33, 189–208.

Armienti, P., Innocenti, F., Petrini, R., Pompilio, M., Villari, L. (1988). *Sub-aphyric alkali basalt from Mt Etna: inferences on the depth and composition of the source magma*. Rendiconti della Società Italiana di Mineralogia e Petrologia 43, 877-891.

Armienti P., Tonarini S., D'Orazio M., Innocenti F. (2004). *Genesis and Evolution of Mt Etna alkaline lavas: petrological and Sr-Nd-B isotope costraints*. Periodico di Mineralogia 73, 29-52.

Asimow, P.D., Ghiorso, M.S. (1998). *Algorithmic modifications extending MELTS to calculate subsolidus phase relations.* American Mineralogist 83, 9-10

Baker, D.R., Moretti, R. (2011). *Modelling the solubility of sulfur in magmas: A 50-years old geochemical challenge.* Reviews in Mineralogy and Geochemistry 73, 167-213.

Ballhaus, C., Berry, R.F., & Green, D.H. (1990). *Oxygen fugacity controls in the Earth`s upper mantle*. Nature 348, 4.

Ballhaus, C., Berry, R.F., and Green, D.H. (1991). *High-pressure experimental calibration of the olivine-ortho-pyroxene-spinel oxygen geobarometer. Implications for the oxidation state of the upper mantle.* Contributions to Mineralogy and Petrology 107, 27–40.

Ballhaus, C. (1993). *Redox States of Lithospheric and Asthenospheric Upper-Mantle*. Contributions to Mineralogy and Petrology 114, 331-348.

Ballhaus, C., Frost, B.R., (1994). *The generation of oxidised CO2-bearing basaltic melts from reduced CH4-bearing upper mantle sources.* Geochimica et Cosmochimica Acta 58, 4931–4940.

Barberi, F., Civetta, L., Gasparini, P., Innocenti, F., Scandone, R., Villari, L. (1974). *Evolution of a section of the Africa–Europa plate boundary: paleomagnetic and volcanologic evidence from Sicily.* Earth and Planetary Science Letters 22, 123–132.

Bau M. (1996). *Controls on the fractionation of isovalent trace elements in magmatic and aqueous systems: evidence from Y/Ho, Zr/Hf, and lanthanide tetrad effect.* Contributions to Mineralogy and Petrology 123, 323-333.

Beccaluva, L., Siena, F., Coltorti, M., Digrande, A., Lo Giudice, A., Macciotta, G., Tassinari, R., Vaccaro, C. (1998). *Nephelinitic to tholeiitic magma generation in a transtensional tectonic setting: an integrated model for the Iblean vulcanism, Sicily*. Journal of Petrology 39, 1547–1576

Ben Avraham Z, Grasso M (1990) *Collisional zone segmentation in Sicily and surrounding areas in the central Mediterranean.* Ann Tectonicae 4:131–139

Berndt J., Koepke J., Holtz F. (2004). *An experimental investigation of the influence of water and oxygen fugacity on differentiation of MORB at 200 MPa*. Journal of Petrology 46, 135–16.

Bianchi, F., Carbone, S., Grasso, M., Invernizzi, G., Lentini, F., Longaretti, G., Merlini, S., Mostardini, F. (1987). *Sicilia orientale: Profilo geologico Nebrodi-Iblei*. Memorie della Società Geologica Italiana 38, 429–458.

Bianchini, G., Yoshikawa, M., Sapienza, G.T. (2010). *Comparative study of ultramafic xenoliths and associated lavas from South-Eastern Sicily: nature of the lithospheric mantle and insights on magma genesis*. Mineralogy and Petrology 98, 111–121.

Branca S, Coltelli M, Groppelli G (2004a) *Geological evolution of Etna volcano*. Mt Etna Volcano Laboratory. AGU (Geophysical monograph series) 143:49–63

Branca S, Coltelli M, Del Carlo P, Groppelli G, Norini G, Pasquare´ G (2004b) *Stratigraphical approaches and tools in the geological mapping of Mt. Etna Volcano*. In: Pasquare` G, Venturini C (eds) Mapping geology in Italy. APATDipartimento Difesa del Suolo, Servizio Geologico d'Italia, S.EL.CA, Firenze, pp 145–156

Branca S., Coltelli M., De Beni E., Wijbrans J. (2008). *Geological evolution of Mount Etna volcano (Italy) from earliest products until the first central volcanism (between 500 and 100 ka ago) inferred from geochronological and stratigraphic data.* Int. J. Earth Sci. 97, 135-152.

Branca, S., Coltelli, M., Groppelli, G., (2011a). *Geological evolution of a complex basaltic*

stratovolcano: Mount Etna, Italy. Italian Journal of Geosciences 130, 306–317.

Brandon, A.D., Draper, D.S. (1996). *Constraints on the origin of the oxidation state of mantle overlying subduction zones: an example from Simcoe, Washington, USA*. Geochimica et Cosmochimica Acta 60, 1739–1749.

Brandon, A.D., Draper, D.S. (1998). *Reply to the comment by B.R. Frost and C. Ballhaus on ''Constraints on the origin of the oxidation state of mantle overlying subduction zones: an*

example from Simcoe, Washington, USA''. Geochimica et Cosmochimica Acta 62, 333–335.

Brenker, F.E., Vollmer, C., Vincze, L., Vekemans, B., Szymanski, A., Janssens, K., Szaloki, I., Nasdala, L., Joswig, W., Kaminsky, F. (2007). *Carbonates from the lower part of transition zone or even the lower mantle.* Earth and Planetary Science Letters 260, 1–9.

Brounce, M., Kelley, K.A., Cottrell, E., & Reagan, M.K. (2015). *Temporal evolution of mantle wedge oxygen fugacity during subduction initiation.* Geology, 43 (9), 775-778.

Brown R, Orsi G, de Vita S. (2008). *New insights into Late Pleistocene explosive volcanic activity and caldera formation on Ischia (southern Italy)*. Bulletin of Volcanology 70(5):583–603

Bryndzia, L.T., Wood, B.J., 1990. *Oxygen thermobarometry of abyssal spinel peridotites: the redox state and C–O–H volatile composition of the Earth's sub-oceanic upper mantle.* American Journal of Science 290, 1093–1116.

Buchner, G. (1975). *Eruzioni vulcaniche e fenomeni vulcano-tettonici di età preistorica e storica nell'isola di Ischia.* Eruptions volcanique, tremblemants de terre et vie des hommes dans la Campanie Antique. Pubbl. N.7. Napoli, Centre J. Bérard.

Burke E. A. J. (2001). *Raman microspectrometry of fluid inclusions*. Lithos 55, 139–158.

Burnham A. D., Berry A. J., Halse H. R., Schofield P. F., Cibin G., Mosselmans J. F. W. (2015). *The oxidation state of europium in silicate melts as a function of oxygen fugacity, composition and temperature.* Chemical Geology 411, 248–259

Canil, D., 1999. *Vanadium partitioning between orthopyroxene, spinel and silicate melt and the redox state of mantle source regions for primary magmas*. Geochimica and Cosmochimica Acta 63, 557–572.

Canil, D., O'Neill, H.S.C., Pearson, D.G., Rudnick, R.L., Mc-Donough, W.F., Carswell, D.A. (1994). *Ferric iron in mantle peridotites and mantle oxidation states*. Earth and Planetary Science Letters 123, 205–220.

Canil, D. (1997). *Vanadium partitioning and the oxidation state of Archaean komatiite magmas.* Nature 389, 842-845.

Canil, D., and Fedortchouk, Y. (2000). *Clinopyroxene-liquid partitioning for vanadium and the oxygen fugacity during formation of cratonic and oceanic mantle lithosphere*. Journal of Geophysical Research-Solid Earth 105, 26003-26016

Canil, D. (2002). *Vanadium in peridotites, mantle redox and tectonic environments: Archean to present.* Earth and Planetary Science Letters 195, 75-90

Carbone, S., Lentini, F. (1981). *Caratteri deposizionali delle vulcanite del Miocene superiore negli Iblei (Sicilia sud-orientale)*. Geologica Romana 20, 79–101.

Carmichael, I.S.E. (1991). *The redox states of basic and silicic magmas: a reflection of their source regions?* Contributions to Mineralogy and Petrology 106, 13.

Christie, D.M., Carmichael, I.S.E., & Langmuir, C.H. (1986). *Oxidation states of mid-ocean ridge basalt glasses*. Earth and Planetary Science Letters 79, 397-411.

Coltelli, M., Del Carlo, P., Vezzoli, L. (2000*). Stratigraphic constrains for explosive activity in the last 100 ka at Etna volcano, Italy*. International Journal of Earth Sciences 89, 665-677.

Coltelli M., Del Carlo, P., Pompilio M., Vezzoli, L., (2005). *Explosive eruption of a picrite: the 3930 BP subplinian eruption of Etna volcano (Italy)*. Geophys. Res. Lett. 32, L23307.

Correale, A., Paonita, A., Martelli, M., Rizzo, A., Rotolo, S.G., Corsaro, R.A., Di Renzo, V., (2014). *A two-component mantle source feeding Mt. Etna magmatism: insights from the geochemistry of primitive magmas.* Lithos 184, 243–258.

Correale, A., Martelli, M., Paonita, A., Rizzo, A., Brusca, L., Scribano, V. (2012). *New evidence of mantle heterogeneity beneath the Hyblean Plateau (southeast Sicily, Italy) as inferred from noble gases and geochemistry of ultramafic xenoliths.* Lithos 132-133, 70-81.

Corsaro, R.A., Pompilio, M., (2004a). *Dynamics of magmas at Mount Etna. Mount Etna: Volcano Laboratory*. Geophysical Monograph Series vol. 143, pp. 91–110

Corsaro, R.A., Métrich, N., Allard, P., Andronico, D., Miraglia, L., Fourmentraux, C., (2009). *The 1974 flank eruption of Mount Etna: an archetype for deep dike-fed eruptions at basaltic volcanoes and a milestone in Etna's recent history*. Journal Geophysical Research-Solid Earth 114, B07204.

Corsaro, R.A., Métrich, N. (2016). *Chemical heterogeneity of Mt. Etna magmas in the last 15 ka. Inferences on their mantle sources*. Lithos 252, 123–13.

Cottrell, E., & Kelley, K.A. (2011*). The oxidation state of Fe in MORB glasses and the oxygen fugacity of the upper* mantle. Earth and Planetary Science Letters 305, 270-282.

Cristofolini, R. (1966). *Le manifestazioni eruttive basiche del Trias superiore nel sottosuolo di Ragusa (Sicilia Sud Orientale)*. Periodico di Mineralogia 35, 1–28.

D'Antonio, M., Tonarini, S., Arienzo, I., Civetta, L., Dallai, L., Moretti, R., Orsi, G., Andria, M., Treccali, A. (2013). *Mantle and crustal processes in the magmatism of the Campania region: inferences from mineralogy, geochemistry, and Sr-Nd-O isotopes of young hybrid volcanics of the Ischia island (South Italy).* Contributions to Mineralogy and Petrology 165, 1173-1194.

Danyushevsky, L.V., Della-Pasqua, F.N., Sokolov, S., (2000). *Re-equilibration of melt inclusions trapped by magnesian olivine phenocrysts from subduction-related magmas: petrological implications.* Contributions to Mineralogy and Petrology 138, 68-83.

Dasgupta, R., Mallik, A., Tsuno, K., Withers, A.C., Hirth, G., Hirschmann, M.M. (2013). *Carbon-dioxide-rich silicate melt in the Earth's upper mantle*. Nature 493, 211-U222.

Dasgupta, R. (2018*). Volatile-bearing partial melts beneath oceans and continents–Where, how much, and of what compositions?* American Journal of Science 318, 141–165.

Davidson J., Turner S., Handley H., Macpherson C., Dosseto A. (2007). *Amphibole "sponge" in arc crust?.* Geology 35, 787–790.

Davis, F.A., & Cottrell, E. (2018). *Experimental investigation of basalt and peridotite oxybarometers: Implications for spinel thermodynamic models and Fe3+ compatibility during generation of upper mantle melts.* American Mineralogist 103, 1056-1067.

Debret, B., Andreani, M., Muñoz, M., Bolfan-Casanova, N., Carlut, J., Nicollet, C., Schwartz, S., Trcera, N. (2014). *Evolution of Fe redox state in serpentine during subduction*. Earth and Planetary Science Letters 400, 206–218.

De Astis, G., Pappalardo, L. & Piochi, M. (2004). *Procida volcanic history: new insights into the evolution of the Phlegraean Volcanic District (Campania region, Italy)*. Bulletin of Volcanology 56, 622^641.

De Beni, E., Branca, S., Coltelli, M., Groppelli, G., Wijbrans, J.R., (2011). *40Ar/39Ar isotopic dating of Etna volcanic succession*. Italian Journal of Geosciences 130, 292–305.

De Moor, J.M., Fischer, T.P., Sharp, Z.D., King, P.L., Wilke, M., Botcharnikov, R.E., Cottrell, E., Zelenski, M., Marty, B., Klimm, K., Rivard, C., Ayalew, D., Ramirez, C., Kelley, K.A. (2013). *Sulfur degassing at Erta Ale (Ethiopia) and Masaya (Nicaragua) volcanoes: implications for degassing processes and oxygen fugacities of basaltic systems*. Geochem. Geophys. Geosyst. 14, 1525–2027.

De Rita, D., Frazzetta, G., Romano, R., (1991). *The Biancavilla-Montalto ignimbrite (Etna, Sicily)*. Bulletin of Volcanology 53, 121-131.

De Vita, S., Sansivero, F., Orsi, G., Marotta, E. & Piochi, M. (2010). *Volcanological and structural evolution of the Ischia resurgent caldera (Italy) over the past 10 k.y.* In: Groppelli, G. & Viereck-Goette, L. (eds) Stratigraphy and Geology of Volcanic Areas. Geological Society of America, Special Papers 464, 193-241.

Di Carlo, I., Pichavant, M., Rotolo, S., G., and Scaillet, B. (2006). *Experimental Crystallization of a High-K Arc Basalt: the Golden Pumice, Stromboli Volcano (Italy)*. Journal of Petrology 47, 1317-1343

Di Stefano A, Branca S. (2002). *Long-term uplift rate of the Etna volcano basament (southern Italy) based on biochronological data from Pleistocene sediments*. Terra Nova 14:61–68

Ding, S., Dasgupta, R., Tsuno, K. (2014). *Sulfur concentration of martian basalts at sulfide saturation at high pressures and temperatures – Implications for deep sulfur cycle on Mars.* Geochimica et Cosmochimica Acta 131, 227-246.

Edmonds, M. (2008). *New geochemical insights into volcanic degassing.* Philos. Trans. Math. Phys. Eng. Sci. 366, 4559–4579.

Eguchi., J, Dasgupta., R. (2018). *Redox state of the convective mantle from CO_2-trace element systematics of ocean basalts.* Geochemical Perspectives Letters 8, 17-21.

Erdman, M. E., Lee C.-T. A., Levander A., Jiang H. (2016). *Role of arc magmatism and lower crustal foundering in controlling elevation history of the Nevada plano and Colorado Plateau: A case study of pyroxenitic lower crust from central Arizona, USA*. Earth and Planetary Science Letters 439, 48–57.

Escrig, S., Besoz, A., Goldstein, S., Langmuir, C. H. (2009). *Mantle source variations beneath the Eastern Lau Spreading Center and the nature of subduction components in the Lau Basin-Tonga arc system.* Geochemistry Geophysics Geosystems 10, Q04014.

Evans, T.M., O'Neill, H. St.C. & Tuff, J. (2008). *The influence of melt composition on the partitioning of REEs, Y, Sc, Zr, and Al between forsterite and melt in the system CMAS.* Geochimica et Cosmochimica Acta 72, 5708-5721.

Evans, K.A. (2012). *The redox budget of subduction zones*. Earth-Science Reviews 113, 11-32.

Evans, K.A., Elburg, M.A., Kamenetsky, V.S. (2012). *Oxidation state of subarc mantle*. Geology 40, 783-786.

Ewart, Anthony (1982). *The mineralogy and petrology of Tertiary-Recent orogenic volcanic rocks: with special reference to the andesitic-basaltic compositional range.* Andesites: Orogenic Andesites and Related Rocks vol.7, 25-98.

Favalli, M., Innocenti, F., Pareschi, M.T., Pasquarè, G., Mazzarini, F., Branca, S., Cavarra, L., Tibaldi, A. (1999). *The DEM or Mt. Etna: geomorphological and structural implications.* Geodinamica Acta, 12:5, 279-290

Foley, S.F. (2011). *A reappraisal of redox melting in the Earth's mantle as a function of tectonic setting and time.* Journal of Petrology 52, 1363–1391.

Frost, B.R. (1991). *Introduction to oxygen fugacity and its petrological importance.* Reviews in Mineralogy and Geochemistry 25(1), 1-9.

Gaetani, G.A., Grove, T.L. (1997). *Partitioning of moderately siderophile elements among olivine, silicate melt and sulfide melts: Constraints on core formation on the Earth and Mars*. Geochimica et Cosmochimica Acta 32, 1057–1086.

Gaillard, F., Scaillet, B., Arndt, N.T. (2011). *Atmospheric oxygenation caused by a change in volcanic degassing pressure*. Nature 478, 229–232.

Gaillard, F., Scaillet, B. (2014). *A theoretical framework for volcanic degassing chemistry in a comparative planetology perspective and implications for planetary atmospheres.* Earth and Planetary Science Letters 403, 307–316.

Gaillard, F., Scaillet, B., Pichavant, M., Iacono-Marziano, G. (2015). *The redox geodynamics linking basalts and their mantle sources through space and time*. Chemical Geology 418, 217–233.

Ganino, C., Arndt, N.T., Zhou, M.-F., Gaillard, F., Chauvel, C. (2008). *Interaction of magma with sedimentary wall rock and magnetite ore genesis in the Panzhizhua mafic intrusion*. Mineral. Deposita http://dx.doi.org/10.1007/s00126-008-0191-5.

Gennaro E., Iacono G., Paonita A., Rotolo S., Martel C., Rizzo., A Pichavant M., Liotta M. (2019). *Melt inclusions track melt evolution and degassing of Etnean magmas in the last 15 ka.* Lithos 324-325, 716-732.

Ghiorso, M.S., Sack, R.O. (1995). *Chemical mass transfer in magmatic processes IV. A revised and internally consistent Thermodynamic model for the interpolation and extrapolation of liquid-solid equilibria in magmatic systems at elevated temperatures and pressures.* Contributions to Mineralogy and Petrology 119, 197-212.

Green T. H., Ringwood A. E. (1968). *Genesis of the calc-alkaline igneous rock suite*. Contributions to Mineralogy and Petrology 18, 105–162

Green T. H., Ringwood A. E. (1968). *Origin of garnet phenocrysts in calc-alkaline rocks*. Contributions to Mineralogy and Petrology 18, 163–174.

Green T. H. (1972). *Crystallization of calc-alkaline andesite under controlled high-pressure hydrous conditions.* Contributions to Mineralogy and Petrology 34, 150–166.

Holland, H.D. (2002). *Volcanic gases, black smokers, and the great oxidation event*. Geochimica et Cosmochimica Acta 66, 3811–3826.

Iacono-Marziano, G., Marecal, V., Pirre, M., Gaillard, F., Arteta, J., Scaillet, B., Arndt, N.T. (2012a). *Gas emissions due to magma–sediment interactions during flood magmatism at the Siberian Traps: gas dispersion and environmental consequences*. Earth and Planetary Science Letters 357, 308–318.

Irber W. (1999). *The lanthanide tetrad effect and its correlation with K/Rb, Eu/Eu*, Sr/Eu, Y/Ho, and Zr/Hf of evolving peraluminous granite suites.* Geochimica et Cosmochimica Acta 63, 489-508.

Jagoutz, O., Schmidt, M.W. (2013). *The composition of the founderer complement to the continental crust and a re-evaluation of fluxes in arcs.* Earth and Planetary Science Letters 371-372, 177–190.

Jenner, F.E., O'Neill, H.St.C., Arculus, R.J., Mavrogenes, J.A. (2010). *The magnetite crisis in the evolution of arc-related magmas and the initial concentration of Au, Ag and Cu*. Journal of Petrology 51, 2445–2464.

Johnson, E.R., Wallace, P.J., Delgado Granados, H., Manea, V.C., Kent, A.J.R., Bindeman, I., Donegan, C.S. (2009). *Subduction-related volatile recycling and magma generation beneath Central Mexico: insights from melt inclusions, oxygen isotopes and geodynamic models*. Journal of Petrology 50, 1729–1764.

Jolivet, L., Faccenna, C. & Piromallo, C. (2009). *From mantle to crust: Stretching the Mediterranean*. Earth and Planetary Science Letters 285, 198-209.

Kamenetsky, V.S., Clocchiatti, R. (1996). *Primitive magmatism of Mt. Etna: insights from mineralogy and melt inclusions.* Earth and Planetary Science Letters 142, 3-4.

Kamenetsky, V.S., Pompilio, M., Métrich, N., Sobolev, A.V., Kuzmin, D.V., Thomas, R., (2007). *Arrival of extremely volatile-rich high-Mg magmas changes explosivity of Mount Etna*. Geology 35, 255-258.

Kelley, K.A., & Cottrell, E. (2009). *Water and the oxidation state of subduction zone magmas*. Science 325, 605-607.

Kelley, K.A., & Cottrell, E. (2012). *The influence of magmatic differentiation on the oxidation state of Fe in a basaltic arc magma*. Earth and Planetary Science Letters 329-330, 109-121.

Kilinc, A., Carmichael, I.S.E., Rivers, M.L., Sack, R.O., (1983). *The ferric-ferrous ratio of natural silicate liquids equilibrated in air.* Contributions to Mineralogy and Petrology 83, 136–140.

Kiseeva, E.S., Vasiukov, D.M., Wood, B.J., McCammon, C., Stachel, T., Bykov, M., Bykova, E., Chumakov, A., Cerantola, V., Harris, J.W., Dubrovinsky, L. (2018). *Oxidized iron in garnets from the mantle transition zone*. Nature Geoscience 11, 144–147.

Kress, V.C., Carmichael, I.S.E., (1991). *The compressibility of silicate liquids containing Fe2O3 and the effect of composition, temperature, oxygen fugacity and pressure on their redox states.* Contributions to Mineralogy and Petrology 108, 82–92.

Kushiro, I., Mysen B. (2002). *A possible effect of melt structure on the Mg-Fe^{2+} partitioning between olivine and melt.* Geochimica and Cosmochimica Acta 66:2267-2273.

Langmuir, C. H., Besoz, A., Escrig, S., Parman, S. W. (2006). *Chemical systematics and hydrous melting of the mantle in back-arc basins.* Back-Arc Spreding Systems: Geological, Biological, Chemical, and Physical Interactions, Geophysical Monograph Series, vol. 166, ed. Christie, D. M et al., 87-146.

Laubier, M., Grove, T.L., & Langmuir, C.H. (2014). *Trace element mineral/melt partitioning for basaltic and basaltic andesitic melts: An experimental and laser ICP-MS study with application to the oxidation state of mantle source regions*. Earth and Planetary Science Letters 392, 265-278.

Lecuyer, C., Ricard, Y. (1999). *Long-term fluxes and budget of ferric iron: implication for the redox states of the Earth's mantle and atmosphere.* Earth and Planetary Science Letters 165, 197–211.

Lee, C.-T.A., Leeman, W. P., Canil, D., Li, Z.-X.A. (2005). *Similar V/Sc systematics in MORB and arc basalts: implications for the oxygen fugacities of their mantle source regions*. Journal of Petrology. 46, 2313–2336.

Lee C.-T.A., Luffi P., Le Roux V., Dasgupta R., Albaréde F., Leeman W.P. (2010*). The redox state of arc mantle using Zn/Fe systematics*. Nature Vol 486, 681-685.

Lee, C.-T.A., Luffi, P., Chin, E.J., Bouchet, R., Dasgupta, R., Morton, D.M., Le Roux, V., Yin, Q.-Z., Jin, D. (2012). *Copper systematics in arc magmas and implications for crust–mantle differentiation*. Science 336, 64–68.

Le Bas, Michael J., et al. (1986). *A chemical classification of volcanic rocks based on the total alkali-silica diagram*. Journal of Petrology 27.3, 745-750.

Le Roux, V., Lee, C.-T. A. & Turner, S. J. (2010). *Zn/Fe systematics in mafic and ultramafic systems: implications for detecting major element heterogeneities in the Earth's mantle.* Geochimica et Cosmochimica Acta 74, 2779–2796.

Lentini F (1982). *The geology of the Mt. Etna basement*. Mem. Soc. Geol. Ital. 23:7–25

Li, Z.-X.A., Lee, C.-T.A. (2006). *Geochemical investigation of serpentinized oceanic lithospheric mantle in the Feather River Ophiolite, California: implications for the recycling rate of water by subduction*. Chemical Geology 235, 161–185.

Liotta, M., Rizzo, A., Paonita, A., Caracausi, A., Martelli, M. (2012). *Sulfur isotopic composition of fumarolic and plume gases at Mount Etna (Italy) and inferences on their magmatic source.* Geochemistry Geophysics Geosystems 13:5.

Luth, R.W. (1993). *Diamonds, eclogites, and the oxidation state of the Earth's Mantle*. *Science* 261, 66–68.

Mallmann, G. & O'Neill, H. St.C. (2009). *The crystal/melt partitioning of V during mantle melting as a function of oxygen fugacity compared with some other elements (Al, P, Ca, Sc, Sc, Ti, Cr, Fe, Ga, Y, Zr and Nb)*. Journal of Petrology 50, 1765-1794.

Mallmann, G., and O'Neill, H.St.C. (2013). *Calibration of an empirical thermometer and oxybarometer based on the partitioning of Sc, Y and V between olivine and silicate melt*. Journal of Petrology, 54, 933–949.

Marianelli, P., Sbrana, A., & Proto, M. (2006). *Magma chamber of the Campi Flegrei supervolcano at the time of eruption of the Campanian Ignimbrite*. Geology, 34, 937–940.

Martin, A.M., Médard, E., Righter, K., Lanzirotti, A. (2017). *Intraplate mantle oxidation by volatile-rich silicic magmas.* Lithos 292-293, 320-330.

Métrich, N., Allard, P., Spilliaert, N., Andronico, D., Burton, M. (2004). *2001 flank eruption of the alkali and volatile-rich primitive basalt responsible for Mount Etna's evolution in the last three decades*. Earth and Planetary Science Letters 228, 1-17.

Métrich, N., Berry, A.J., O'Neill, H.S.C., Susini, J. (2009). *The oxidation state of sulfur in synthetic and natural glasses determined by X-ray absorption spectroscopy*. Geochimica et Cosmochimica Acta, 73, 2382–2399,

Miraglia, L., (2002). *Evidence for heterogeneous magmas in the feeding system of the 1763 "La Montagnola" eruption at Mount Etna*. Plinius 27, 108-112.

Mollo, S., Giacomoni, P.P., Andronico, D., Scarlato, P. (2015). *Clinopyroxene and titanomagnetite cation redistribution at Mt. Etna volcano (Sicily, Italy): Footprints of the final solidification history of lava fountains and lava flows.* Chemical Geology 406, 45-54.

Moretti, R., (2005). *Polymerization, basicity, oxidation state and their role in ionic modelling of silicate melts.* Ann. Geophys. 48, 583–608.

Moretti, R., Arienzo, I., Orsi, G., Civetta, L., D'Antonio, M. (2013). *The deep plumbing system of Ischia: a physico-chemical window on the fluid-saturated and CO_2-sustained Neapolitan volcanism (southern Italy).* Journal of Petrology 54, 951-984.

Moussallam, Y., Oppenheimer, C., Scaillet, B., Gaillard, F., Kyle, P., Peters, N., Hartley, M.E., Berlo, K., Donovan, A. (2014). *Tracking the changing oxidation state of Erebus magmas, from mantle to surface, driven by magma ascent and degassing*. Earth and Planetary Science Letters 393, 200–209. http://dx.doi.org/10.1016/j.epsl.2014.02.055.

Mungall, J.E. (2002). *Roasting the mantle: slab melting and the genesis of major Au and Au-rich Cu deposits.* Geology 30, 915–918.

Mungall, J.E., Hanley, J.J., Arndt, N.T., Debecdelievre, A., (2006). *Evidence from meimechites and other low-degree mantle melts for redox controls on mantle–crust fractionation of platinum-group elements*. PNAS 103, 12695–12700.

Mysen B. (2014). *Water-melt interaction in hydrous magmatic systems at high temperature and pressure.* Progress in Earth and Planetary Science 1:4.

Niu Y. (2012). *Earth processes cause Zr-Hf and Nb-Ta fractionations, but why and how?* RSC Advance 2, 3587-3591.

O'Neill, H.St.C., Rubie, D.C., Canil, D., Geiger, C.A., Ross, C.R., Seifert, F., Woodland, A.B. (1993). *Ferric iron in the upper mantle and in Transition Zone assemblages: implications for relative oxygen fugacities in the mantle.* In: Rubie, D.C. (Ed.), Evolution of the Earth and Planets. American Geophysical Union, Geophysical Monograph 74, 7473–7488

Orsi G, Gallo G, Zanchi A (1991). *Simple shearing block resurgence in caldera depressions. A model from Pantelleria and Ischia*. Journal of Volcanology and Geothermal Research 47:1–11

Orsi G, Gallo G, Heiken G, Wohletz K, Yu E, Bonani G (1992). *A comprehensive study of the pumice formation and dispersal: the Cretaio tephra of Ischia (Italy).* Journal of Volcanology and Geothermal Research 53, 329–354

Orsi G, Piochi M, Campajola L, D'Onofrio A, Gialanella L, Terrasi F (1996b). *14C geochronological constraints for the volcanic history of the island of Ischia (Italy) over the last 5,000 years*. Journal of Volcanology and Geothermal Research 71, 249–257

Orsi, G., de Vita, S., Di Vito, M., Isaia, R., Nave, R. & Heiken, G. (2003). *Facing volcanic and related hazards in the Neapolitan area.* In: Heiken, G., Fakundiny, R. & Sutter, J. (eds) Earth Sciences in the Cities: A Reader. American Geophysical Union, Special Publication Series 56, 121-170.

Padron-Navarta, J.A., Sanchez-Vizcaino, V.L., Garrido, C.J., Gomez-Pugnaire, M.T. (2011). *Metamorphic record of high-pressure dehydration of antigorite serpentinite to chlorite harzburgite in a subduction setting (Cerro del Almirez, Nevado-Filabride Complex, Southern Spain)*. Journal of Petrology 52, 2047–2078.

Papike, J.J., Burger, P.V., Bell, A.S., Le, L., Shearer, C.K., Sutton, S.R., Jones, J., & Newville, M. (2013). *Developing vanadium valence state oxybarometers (spinel-melt, olivine-melt, spinel-olivine) and V/(Cr+Al) partitioning (spinel-melt) for martian olivine-phyric basalts*. American Mineralogist 98, 2193-2196.

Parkinson, I.J., & Arculus, R.J. (1999*). The redox state of subduction zones: insights from arc-peridotites*. Chemical Geology 160, 409-423.

Peccerillo, A. (2005). *Plio-Quaternary Volcanism in Italy Petrology, Geochemistry, Geodynamics*. Heidelberg: Springer, 365 p.

Perinelli, C., Sapienza, G.T., Armienti, P., Morten, L. (2008). *Metasomatism of the upper mantle beneath the Hyblean Plateau (Sicily): evidence from pyroxenes and glass in peridotite xenoliths.* London Geological Society, Special Publication 293, 197–221.

Putirka, K. (2008). *Thermometers and Barometers for Volcanic Systems*. In: Putirka, K., Tepley, F. (Eds.), Minerals, Inclusions and Volcanic Processes, Reviews in Mineralogy and Geochemistry, Mineralogical Soc. Am., v. 69, pp. 61-120.

Rittman, A., (1965). *Notizie sull'Etna.* Suppl. Nuovo Cimento, 3(I), 1117-1123.

Rocchi, S., Longaretti, G., Salvadori, M. (1998*). Subsurface Mesozoic and Cenozoic magmatism in south-eastern Sicily: distribution, volume and geochemistry of magmas*. Acta Vulcanologica 10, 395–408.

Rohrbach, A., Schmidt, M.W., (2011*). Redox freezing and melting in the Earth's deep mantle resulting from carbon–iron redox coupling*. Nature 472, 209–212.

Rudnick R. L., Taylor S. R. (1986). *Geochemical constraints on the origin of Archaean tonalitic-trondhjemitic rocks and implications for lower crustal composition*. London Geological Society, Special Publication 24, 179–191.

Sack, R.O., Ghiorso, M.S. (1989). *Importance of consideration of mixing properties in establishing an internally consistent database: Thermochemistry of minerals in the system Mg2SiO4-Fe2SiO4-SiO2.* Contributions to Mineralogy and Petrology 102, 41-68.

Sack, R.O., Ghiorso, M.S. (1991a). *An internally consistent model for the thermodynamic properties of Fe–Mg-titanomagnetite–aluminate spinels*. Contributions to Mineralogy and Petrology 106, 474–505.

Sack, R.O., Ghiorso, M.S. (1991b). Chromian spinels as petrogenic indicators: the thermodynamics and petrological applications. American Mineralogist 76, 827-847.

Sack, R.O., Ghiorso, M.S. (1994a). *Thermodynamics of multicomponent pyroxenes: I. Formulation of a general model.* Contributions to Mineralogy and Petrology 116, 227-286.

Sack, R.O., Ghiorso, M.S. (1994b). *Thermodynamics of multicomponent pyroxenes: II. Phase relations in the quadrilateral.* Contributions to Mineralogy and Petrology 116, 287-300

Sack, R.O., Ghiorso, M.S. (1994c). *Thermodynamics of multicomponent pyroxenes: III. Calibration of Fe2+(Mg)-1, TiAl(MgSi)-1, TiFe3+(MgSi)-1, AlFe3+(MgSi)-1, NaAl(CaMg)-1, Al2(MgSi)-1 and Ca(Mg)-1 exchange reactions between pyroxenes and silicate melts.* Contributions to Mineralogy and Petrology 118, 271-296.

Santacroce, R., Cioni, R., Marianelli, P., Sbrana, A., Sulpizio, R., Zanchetta, G., Donahue, D. J. & Joron, J. L. (2008). *Age and whole rock-glass compositions of proximal pyroclastics from the major explosive eruptions of Somma^Vesuvius: A review as a tool for distal tephrostratigraphy.* Journal of Volcanology and Geothermal Research 177, 1-18.

Sapienza, G., Hilton, D.R., Scribano, V. (2005). *Helium isotopes in peridotite mineral phases from Hyblean Plateau xenoliths (southeastern Sicily, Italy).* Chemical Geology 219, 115–129.

Sbrana, A., Fulignati, P., Marianelli, P., Boyce, A.J., Cecchetti, A. (2009). *Exhumation of an active magmatic–hydrothermal system in a resurgent caldera environment: the example of Ischia (Italy)*. London Geological Society, 1061–1073

Sbrana, A., Marianelli, P., Pasquini, G. (2018). *Volcanology of Ischia (Italy)*. Journal of Maps 14, 494-503.

Schiano, P., (2003). *Primitive mantle magmas recorded as silicate melt inclusions in igneous minerals*. Earth Science Reviews 63, 1-2, 121-144.

Schiavi, F., Roschiglione, A., Kitagawa, H., Kobayashi, K., Nakamura, E., Nuccio, P.M., Ottolini, L., Paonita, A., Vannucci, R. (2009). *Geochemical heterogeneities in magma beneath Mount Etna recorded by 2001-2006 melt inclusions.* Geochemistry Geophysics Geosystems 16, 2109-2126.

Schmidt, M.W., Poli, S. (1998). *Experimentally based water budgets for dehydrating slabs and consequences for arc magma generation*. Earth and Planetary Science Letters 163, 361–379.

Schuth, S., Oeser, M., & Holtz, F. (2018). *Experimental calibration and implications of olivine-melt vanadium oxybarometry for hydrous basaltic arc magmas*. American Mineralogist 103, 369-383.

Shearer, C.K., McKay, G., Papike, J. J. & Karner, J. M. (2006). *Valence state partitioning of vanadium between olivine-liquid: Estimates of the oxygen fugacity of Y980459 and application to other olivine-phyric martian basalts.* American Mineralogist 91, 1657-1663.

Shishkina, T. A., Portnyagin, M. V., Botcharnikov, R. E., Almeev, R. R., Simonyan, A. V., Garbebe-Schonberg, D. (2018). *Experimental calibration and implications of olivine-melt vanadium oxybarometry for hydrous basaltic arc magmas*. American Mineralogist, 103(3), 369–383.

Sifre, D., Gardes, E., Massuyeau, M., Hashim, L., Hier-Majumder, S., Gaillard, F. (2014). *Electrical conductivity during incipient melting in the oceanic low-velocity zone*. Nature 509, 81–85.

Sobolev, A.V., and 19 others. (2007). *The amount of recycled crust in sources of mantle-derived melts.* Science, 316, 412–417.

Song S. and Su L. (1998). *Plastic rheology of the Yushigou mantle peridotite and implications for dynamics of Paleo-Plate movement in the North Qilian Mountains.* Acta. Geol. Sin. 72, 131–141.

Song, S., Su, L., Niu, Y., Lai, Y., Zhang, L. (2009). *CH_4 inclusions in orogenic harzburgite: Evidence for reduced slab fluids and implication for redox melting in mantle wedge.* Geochimica et Cosmochimica Acta 73, 1737-1754.

Spilliaert, N., Allard, P., Métrich, N., Sobolev, A.V. (2006a). *Melt inclusion record of the conditions of ascent, degassing, and extrusion of volatile-rich alkali basalt during the powerful 2002 flank eruption of Mount Etna (Italy).* Journal of Geophysical Research 111, B04203,

Spilliaert, N., Metrich, N. and Allard, P. (2006b*). S-Cl-F degassing pattern of water-rich alkali basalt: modelling and relationship with eruption styles on Mount Etna volcano*. Earth and Planetary Science Letters 248, 772-786.

Stagno, V., Ojwang, D.O., McCammon, C.A., Frost, D.J. (2013). *The oxidation state of the mantle and the extraction of carbon from Earth's interior*. Nature 493, 84–87.

Stagno V., Frost D. J., McCammon C., Mohseni H., Fei Y. (2015). *The oxygen fugacity at which graphite or diamond forms from carbonate-bearing melts in eclogitic rocks*. Contributions to Mineralogy and Petrology 169, 16.

Tang M., McDonough W. F., Ash R. D. (2017). *Europium and strontium anomalies in the MORB source mantle*. Geochimica et Cosmochimica Acta 197, 132–141.

Tang M., Erdman M., Eldridge G., Lee C.-T. A. (2018). *The redox "filter" beneath magmatic orogens and the formation of continental crust*. Science Advances. 4, eaar4444

Tanguy, J.C. (1978). *Tholeiitic basalt magmatism of Mount Etna and its relations with the alkaline series.* Contributions to Mineralogy and Petrology 66, 51–67

Tanguy, J.-C., Condomines, M., Kieffer, G. (1997). *Evolution of the Mount Etna magma: Constraints on the present feeding system and eruptive mechanism.* Journal of Volcanology and Geothermal Research 75, 221–250.

Tonarini, S., Armienti, P., D'Orazio, M., Innocenti, F. (2001). *Subduction-like fluids in the genesis of the Mt. Etna magmas: evidence from boron isotopes and fluid mobile elements*. Earth and Planetary Science Letters 5989, 1–13.

Vezzoli, L. (ed.) (1988*). Island of Ischia.* CNR Quaderni de 'La ricerca scientifica'. 114-10, 122.

Viccaro, M., Ferlito, C., Cristofolini, R. (2007). *Amphibole crystallization in the Etnean feeding system: mineral chemistry and trace element partitioning between Mg-hastingsite and alkali basaltic melt.* European Journal of Mineralogy 19, 499-511

Viccaro, M., Cristofolini, R. (2008). *Nature of mantle heterogeneity and its role in the short-term geochemical and volcanological evolution of Mt. Etna (Italy).* Lithos 105, 272-288.

Wang, J., Xiong, X., Takahashi, E., Zhang, L., Li, L., & Liu, X. (2019). *Oxidation state of arc mantle revealed by partitioning of V, Sc, and Ti between mantle minerals and basaltic melts.* Journal Geophysical Research-Solid Earth, 124, 4617–4638.

White, W.M. (2013). *Geochemistry*. Ed Wiley-Blackwell.

Wood, B. J., Bryndzia, L. T. & Johnson, K.E. (1990) *Mantle oxidation state and its relationship to tectonic environment and fluid speciation*. Science 248, 337–345.

Woodland, A.B., Koch, M. (2003). *Variation in oxygen fugacity with depth in the upper mantle beneath the Kaapvaal craton, Southern Africa*. Earth and Planetary Science Letters 214, 295–310.

Workman, R.K., Hart, S.R. (2005). *Major and trace element composition of the depleted MORB mantle (DMM).* Earth and Planetary Science Letters 231, 53-72.

Yang, X., Gaillard, F., Scaillet, B. (2014). *A relatively reduced Hadean continental crust and implications for the early atmosphere and crustal rheology*. Earth and Planetary Science Letters 393, 210–219.

Yaxley, G.M., Berry, A.J., Kamenetsky, V.S., Woodland, A.B., Golovin, A.V. (2012). *An oxygen fugacity profile through the Siberian Craton — Fe K-edge XANES determinations of Fe3+/ΣFe in garnets in peridotite xenoliths from the Udachnaya East kimberlite*. Lithos 140–141, 142–151.

Yaxley, G.M., Berry, A.J., Rosenthal, A., Woodland, A.B., Paterson, D. (2017). *Redox preconditioning deep cratonic lithosphere for kimberlite genesis - Evidence from the central Slave Craton.* Scientific Reports 7, doi: 10.1038/s41598-017-00049-3.

Zajacz, Z., Candela, P.A., Piccoli, P.M., Sanchez-Valle, C., Walle, M. (2013). Solubility and partitioning behaviour of Au, Cu, Ag and reduced S in magma. Geochimica et Cosmochimica Acta 112, 288–304.

Zhang, H.L., Cottrell, E., Solheid, P.A., Kelley, K.A., Hirschmann, M.M. (2018). *Determination of $Fe^{3+}/\Sigma Fe$ of XANES basaltic glass standards by Mössbauer spectroscopy and its application to the oxidation state of iron in MORB.* Chemical Geology 479, 166-175.

Appendix

A1 Trace element composition

Table A1.1. Trace elements compositions of FS olivine

	FS 01 Oliv	FS 02 Oliv	FS 03 Oliv	FS 04 Oliv	FS 05 Oliv	FS 06 Oliv	FS 08 Oliv	FS 11 Oliv	FS 12 Oliv	FS 13 Oliv
Li7	0.46	0.47	0.45	0.57	0.36	0.48	0.46	0.38	0.55	0.49
Be9						0.03				0.04
B11	0.45	0.49	0.61	0.32	0.30	0.40	0.80	0.52	0.67	
Sc45	1.00	1.10	1.13	1.09	1.11	1.06	1.05	1.11	1.05	1.08
V51	1.90	2.14	1.95	1.86	1.68	1.66	2.01	1.93	1.69	1.69
Cr53	110.25	114.58	116.94	112.29	102.81	107.80	116.01	115.26	105.40	104.88
Co59	89.40	90.27	90.50	86.64	87.64	89.84	91.41	89.97	86.21	85.75
Ni60	800.98	752.21	788.75	775.51	717.36	748.77	755.49	755.11	701.48	713.80
Cu63	0.49	0.53	0.51	0.49	0.48	0.54	0.48	0.48	0.48	0.49
Zn66	30.98	31.94	32.42	31.47	30.11	32.05	30.91	31.71	30.40	30.51
Rb85		0.007					0.005	0.003		
Sr88	0.009	0.636	0.006	0.007	0.011	0.008	0.013	0.008	0.008	0.007
Y89	0.023	0.037	0.027	0.022	0.028	0.021	0.017	0.019	0.019	0.021
Zr90	0.009	0.056	0.014	0.015	0.013	0.007	0.014	0.012	0.013	0.007
Nb93	0.001	0.019	0.001	0.001	0.003	0.001	0.001	0.002	0.002	0.001
Cs133				0.002				0.001		
Ba137		0.240			0.017		0.010	0.005	0.005	
La139		0.022	0.001	0.001			0.000		0.001	
Ce140	0.001	0.058		0.001			0.002		0.001	0.000
Pr141		0.008			0.001			0.000		0.001
Nd146	0.003	0.015					0.002			0.002
Sm147		0.018	0.003		0.002		0.005	0.003		
Eu153		0.003			0.001		0.001			
Gd157		0.005		0.003	0.004			0.006		0.002
Tb159	0.000	0.001	0.001			0.001		0.001		0.000
Dy163	0.002	0.006	0.003	0.005	0.002		0.002	0.002		0.004
Ho165	0.001	0.001	0.003	0.002	0.001	0.001	0.002	0.000	0.001	0.002
Er166	0.003	0.011	0.007	0.006	0.006	0.003	0.002		0.003	0.005
Tm169	0.002	0.001	0.001	0.001	0.001	0.001	0.001	0.001		0.001
Yb172	0.010	0.012	0.006	0.005	0.009		0.004	0.006	0.010	0.007
Lu175	0.002	0.001	0.002	0.002	0.003	0.001	0.001	0.002	0.002	0.001
Hf178				0.003						
Ta181	0.001	0.002		0.001				0.001		
Pb206		0.008		0.005		0.004		0.023		
Pb207	0.005	0.017		0.008			0.008	0.022	0.007	
Pb208	0.005	0.008	0.008	0.004			0.004	0.008		
Th232	0.001	0.005					0.001			
U238		0.002	0.001					0.002		0.001
	FS 14 Oliv	FS 16 Oliv	FS 17 Oliv	FS 18 Oliv	FS 19 Oliv	FS 22 Oliv	FS 24 Oliv	FS 25 Oliv	FS 26 Oliv	FS 28 Oliv
Li7	0.42	0.42	0.51	0.45	0.48	1.56	1.76	1.55	1.57	1.47
Be9		0.05			0.02	0.06		0.03		0.03

B11	0.49		0.46	0.52	0.64		0.84			0.88
Sc45	1.04	1.02	1.07	1.03	1.02	0.73	0.77	0.79	0.89	0.97
V51	1.68	1.71	1.86	1.72	1.73	2.46	2.29	2.36	2.49	2.24
Cr53	100.65	102.36	111.95	85.98	103.51	363.59	360.13	380.67	394.96	384.28
Co59	81.58	85.18	87.14	86.61	85.68	102.66	102.10	105.79	107.09	106.41
Ni60	679.76	694.25	723.64	632.69	723.83	1405.0	1318.0	1379.7	1490.9	1441.9
Cu63	0.46	0.51	0.48	0.48	0.53	0.74	0.77	0.76	0.76	0.72
Zn66	28.33	29.49	30.40	30.22	30.35	48.50	47.56	49.34	49.55	49.21
Rb85	0.005	0.003		0.004			0.004			
Sr88	0.190	0.009	0.009	0.010	0.020	0.147	0.005	0.006	0.006	0.043
Y89	0.023	0.021	0.022	0.025	0.022	0.033	0.028	0.025	0.031	0.030
Zr90	0.008	0.029	0.015	0.013	0.014	0.017	0.012	0.015	0.018	0.010
Nb93	0.001		0.001	0.002	0.001	0.001	0.002		0.001	0.001
Cs133			0.001						0.003	
Ba137	0.005	0.007	0.005	0.011	0.100	0.007				
La139	0.001			0.004	0.003	0.001	0.001			0.001
Ce140		0.000	0.001	0.007		0.002	0.001			0.001
Pr141		0.001		0.002		0.001			0.001	0.001
Nd146	0.003									
Sm147				0.005						
Eu153	0.001			0.001		0.001		0.001		0.001
Gd157	0.004	0.015		0.004		0.004	0.006			0.005
Tb159		0.001	0.000			0.001		0.001	0.001	
Dy163	0.005		0.003	0.005	0.002	0.005		0.003	0.006	0.005
Ho165	0.001	0.001	0.001	0.002	0.002	0.002	0.002	0.001	0.002	0.002
Er166	0.004	0.004	0.005	0.005	0.004	0.008	0.006	0.004	0.010	0.005
Tm169	0.001	0.001	0.001	0.001	0.003	0.002	0.001		0.001	0.003
Yb172	0.005	0.004	0.005	0.006	0.006	0.013	0.013	0.010	0.008	0.013
Lu175	0.002	0.001	0.002	0.002	0.002	0.002	0.002	0.001	0.003	0.002
Hf178	0.003				0.003	0.005				0.005
Ta181			0.001	0.001			0.001			
Pb206	0.029	0.035		0.014	0.005	0.016	0.020		0.007	0.008
Pb207	0.014	0.006		0.009	0.028		0.008			
Pb208	0.012	0.011	0.006	0.008	0.006		0.017	0.006	0.005	
Th232										
U238				0.002			0.002	0.001		

Table A1.2 Trace elements composition of Vateliero olivine

	VAT 01 Oliv	VAT 02 Oliv	VAT 03A Oliv	VAT 03 Oliv	VAT 04 Oliv	VAT 05 Oliv	VAT 06 Oliv	VAT 07A Oliv	VAT 07B Oliv	VAT 08 Oliv	VAT 09 Oliv
Li7	2.62	3.14	2.87	3.26	2.40	2.12	2.51	2.55	2.89	2.79	2.71
Be9									0.04		
B11	0.55	0.28	0.38	0.57	0.35	0.29	0.51	0.33	0.40	0.44	0.59
Sc45	11.49	11.15	10.66	11.60	8.70	9.07	8.61	8.03	7.95	10.73	10.69
V51	3.45	3.42	3.41	3.97	5.77	3.46	2.93	7.35	4.92	4.05	4.45
Cr53	232.17	233.93	231.99	269.31	1.57	103.46	208.21	15.27	7.39	126.00	55.89
Co59	140.25	153.12	146.14	156.31	274.15	132.86	137.32	205.36	207.13	171.99	180.70
Ni60	1551.6	1687.3	1610.7	1734.1	373.0	1318.1	1555.7	581.6	617.0	1568.8	1331.3

Cu63	1.88	1.91	1.98	2.18	0.80	1.63	1.82	0.92	1.18	2.36	3.54
Zn66	59.78	63.78	64.03	67.94	103.23	54.51	59.28	96.20	95.65	67.07	72.17
Rb85		0.014				0.005	0.003	0.007		0.006	0.007
Sr88	0.007	0.025	0.032	0.016	0.006	0.022	0.009	0.025	0.008	0.015	3.569
Y89	0.085	0.090	0.086	0.099	0.157	0.089	0.076	0.169	0.172	0.113	0.129
Zr90	0.022	0.027	0.020	0.035	0.032	0.035	0.018	0.039	0.036	0.023	0.103
Nb93	0.001	0.003		0.002	0.001	0.001		0.002	0.001	0.002	0.002
Cs133					0.002						
Ba137	0.085	0.091	0.063	0.007		0.045		0.065	0.006		1.248
La139	0.001	0.005		0.001		0.001	0.001	0.002		0.001	0.026
Ce140	0.001	0.010	0.001			0.002		0.002	0.002		0.049
Pr141	0.001						0.001	0.002			0.011
Nd146	0.006	0.022	0.005			0.006					0.033
Sm147		0.007				0.007			0.013	0.009	0.014
Eu153	0.001		0.003	0.001	0.002		0.002	0.002	0.002	0.002	0.003
Gd157	0.007	0.007	0.008		0.007			0.010	0.010		0.010
Tb159	0.001	0.001	0.003	0.001	0.002	0.002		0.002	0.002		0.001
Dy163	0.015	0.009	0.012	0.016	0.014	0.007	0.003	0.017	0.018	0.009	0.020
Ho165	0.001	0.005	0.001	0.003	0.004	0.004	0.003	0.008	0.004	0.004	0.004
Er166	0.009	0.014	0.013	0.015	0.015	0.014	0.008	0.024	0.024	0.019	0.012
Tm169	0.003	0.003	0.003	0.004	0.005	0.003	0.003	0.007	0.006	0.003	0.005
Yb172	0.029	0.035	0.031	0.030	0.039	0.034	0.020	0.055	0.060	0.037	0.043
Lu175	0.006	0.007	0.007	0.009	0.007	0.007	0.007	0.014	0.009	0.008	0.009
Hf178	0.004	0.002		0.001	0.006		0.002		0.002		0.006
Ta181	0.001	0.001			0.002		0.001		0.002		0.000
Pb206	0.018	0.038	0.010		0.013			0.018		0.014	
Pb207		0.029					0.014			0.016	0.018
Pb208		0.010	0.013	0.013		0.026			0.008		0.016
Th232		0.004			0.001		0.001	0.001	0.002		0.004
U238			0.001		0.001			0.002		0.001	0.002

	VAT 10 Oliv	VAT 11 Oliv	VAT 12 Oliv	VAT 13 Oliv	VAT 14 Oliv	VAT 15 Oliv	VAT 16 Oliv	VAT 17 Oliv	VAT 18 Oliv	VAT 19 Oliv	VAT 21 Oliv
Li7	2.67	2.41	2.50	1.90	2.12	2.87	1.67	2.18	2.37	1.86	2.31
Be9			0.06	0.07			0.04	0.06		0.07	
B11	0.33	0.42	0.40	0.44	0.35		0.38	0.29	0.37	0.27	0.33
Sc45	7.83	9.55	8.55	9.04	9.09	9.65	9.74	9.10	9.80	9.14	10.20
V51	4.75	4.01	3.33	4.69	4.06	4.48	4.08	3.66	4.05	4.34	3.89
Cr53	12.12	97.40	221.57	49.33	93.66	16.50	48.28	44.26	185.37	43.80	43.77
Co59	210.23	171.80	142.43	204.87	177.24	205.22	165.39	190.34	152.37	177.38	188.32
Ni60	702.2	1339.2	1580.4	912.7	1419.1	584.1	1242.2	1364.5	1591.1	1194.4	1261.3
Cu63	1.03	2.14	1.85	2.13	2.40	1.52	2.71	3.21	2.10	2.45	3.07
Zn66	90.85	65.04	61.60	77.50	74.05	89.44	63.54	69.92	66.14	68.08	68.70
Rb85		0.012					0.271	0.003	0.004	0.005	
Sr88	0.009	0.036	0.009	0.007	0.009	0.011	1.119	0.005	0.009	0.010	0.007
Y89	0.158	0.110	0.080	0.135	0.125	0.162	0.115	0.103	0.097	0.130	0.111
Zr90	0.027	0.034	0.026	0.020	0.024	0.034	0.085	0.029	0.025	0.039	0.026
Nb93	0.001	0.003	0.001	0.002		0.002	0.039	0.001			
Cs133	0.002	0.003				0.002	0.013				

Ba137		0.108	0.007	0.010			2.571				
La139		0.001	0.001	0.001	0.001		0.032	0.002		0.001	
Ce140		0.004	0.002	0.001	0.001	0.001	0.167				
Pr141	0.001	0.001				0.001	0.011		0.001		0.001
Nd146	0.009	0.006				0.003	0.038			0.007	0.008
Sm147	0.008	0.006	0.006	0.008	0.005	0.007	0.013		0.012	0.013	
Eu153	0.002				0.001		0.003	0.001	0.002	0.002	
Gd157	0.011	0.009	0.005	0.012	0.010	0.009	0.012		0.017	0.011	0.007
Tb159	0.001	0.002	0.001		0.002	0.001	0.001		0.002	0.001	0.002
Dy163	0.019	0.017	0.006	0.017	0.012	0.017	0.013	0.013	0.013	0.013	0.016
Ho165	0.006	0.004	0.003	0.004	0.005	0.007	0.005	0.005	0.003	0.005	0.003
Er166	0.022	0.014	0.010	0.020	0.014	0.023	0.020	0.016	0.013	0.028	0.017
Tm169	0.007	0.004	0.003	0.004	0.004	0.004	0.005	0.005	0.004	0.006	0.004
Yb172	0.049	0.030	0.029	0.041	0.038	0.066	0.039	0.028	0.038	0.047	0.027
Lu175	0.010	0.008	0.008	0.009	0.008	0.012	0.011	0.005	0.008	0.011	0.006
Hf178		0.006	0.002	0.005			0.005		0.003		
Ta181	0.001	0.001					0.006	0.001		0.002	
Pb206			0.017				0.027				0.014
Pb207					0.010		0.017				0.016
Pb208	0.008	0.014		0.018	0.007	0.015	0.023				0.011
Th232	0.001		0.001		0.001		0.007		0.001		
U238	0.001						0.009				

Table A1.3 Trace elements composition of FS MIs

	FS 01 melt	FS 02 melt	FS 03 melt	FS 04 melt	FS 05 melt	FS 06 melt	FS 08 melt	FS 22 melt	FS 24 melt	FS 25 melt	FS 26 melt	FS 28 melt
Li7	5.73	5.72	3.97	5.20	5.11	5.20	5.48	6.51	4.90	5.48	5.75	5.98
Be9		1.25	1.19	0.65	0.60	0.93	0.80	0.84	0.97	0.24	0.54	0.98
B11	11.08	5.46	8.07	7.16	7.01	10.00	7.46	7.15	7.99	6.85	5.55	7.96
Sc45	37.81	37.61	33.67	34.73	35.64	33.87	35.37	43.38	42.93	39.11	40.49	39.91
V51	283.45	251.58	249.82	252.88	255.54	250.73	245.94	265.45	305.90	257.07	236.43	249.39
Cr53	578.69	497.52	542.53	710.01	677.15	647.07	560.00	600.96	626.69	533.72	670.36	569.07
Co59	42.95	47.06	41.28	46.42	45.47	43.56	45.11	49.69	60.02	47.73	47.25	51.79
Ni60	142.34	111.86	144.62	158.87	111.15	139.13	105.50	248.18	377.93	267.25	197.52	223.57
Cu63	100.56	109.93	99.82	108.30	105.83	100.96	103.51	85.43	100.24	90.20	97.83	99.04
Zn66	81.07	78.29	80.51	121.80	85.11	90.53	79.53	82.33	95.28	76.65	83.80	86.00
Rb85	31.24	16.02	18.33	15.81	21.37	22.12	22.44	17.75	28.71	21.08	15.97	23.17
Sr88	816.87	935.39	1051.00	998.81	673.83	613.65	941.24	1179.84	1120.70	973.64	945.64	687.40
Y89	14.68	15.52	13.73	14.95	14.89	14.01	16.24	16.21	17.18	13.94	14.55	13.35
Zr90	71.97	95.49	94.34	86.89	63.78	57.08	99.87	102.74	104.14	85.36	93.47	56.65
Nb93	17.22	29.59	22.10	28.33	10.58	9.66	37.90	27.18	39.84	32.21	34.65	9.82
Cs133	0.72	0.33	0.48	0.41	0.44	0.42	0.47	0.42	0.75	0.58	0.36	0.51
Ba137	352.64	487.27	579.54	505.08	268.40	265.54	484.13	511.69	541.23	437.77	408.92	265.05
La139	29.87	41.96	41.18	44.84	19.65	18.03	45.52	45.25	53.04	44.04	44.39	18.57
Ce140	59.24	81.89	79.53	85.03	41.71	39.29	90.13	93.35	106.28	87.01	88.59	39.48
Pr141	6.60	9.19	8.92	9.29	4.95	4.70	10.00	10.06	10.81	9.19	9.55	4.48
Nd146	27.39	35.58	32.36	35.33	20.10	18.28	38.41	38.12	41.37	36.47	36.55	19.01
Sm147	4.93	6.61	5.96	5.86	4.15	3.94	6.54	6.33	7.43	5.62	6.05	3.94
Eu153	1.62	1.91	1.92	1.83	1.39	1.29	1.94	1.85	1.87	1.69	1.77	1.25

Gd157	4.46	5.52	4.89	5.21	4.07	3.60	5.45	5.26	4.99	4.27	4.33	3.20
Tb159	0.57	0.63	0.50	0.61	0.53	0.46	0.64	0.60	0.62	0.52	0.51	0.43
Dy163	3.05	3.48	3.08	3.42	3.03	3.09	3.63	3.52	3.60	3.07	3.16	2.72
Ho165	0.59	0.56	0.55	0.61	0.59	0.60	0.63	0.66	0.58	0.55	0.55	0.53
Er166	1.62	1.58	1.51	1.50	1.48	1.44	1.62	1.64	1.71	1.40	1.40	1.39
Tm169	0.20	0.23	0.16	0.20	0.22	0.19	0.23	0.22	0.21	0.20	0.19	0.18
Yb172	1.30	1.27	1.14	1.47	1.46	1.38	1.45	1.47	1.18	1.45	1.24	1.44
Lu175	0.22	0.20	0.19	0.17	0.21	0.19	0.22	0.21	0.18	0.18	0.21	0.16
Hf178	1.83	2.33	2.12	1.98	1.58	1.66	2.46	2.45	2.38	2.06	2.05	1.37
Ta181	0.80	1.26	1.03	1.20	0.55	0.54	1.90	1.24	1.56	1.47	1.55	0.49
Pb206	5.83	5.39	7.34	6.78	4.43	4.17	6.03	7.17	7.10	6.42	6.15	4.87
Pb207	5.01	5.07	6.47	6.19	3.55	3.81	5.15	6.38	6.22	5.03	5.05	4.18
Pb208	4.95	5.26	7.21	6.44	4.04	3.94	5.41	6.66	6.22	5.43	5.43	4.77
Th232	4.04	5.63	6.78	6.64	2.73	2.55	6.43	5.52	6.42	5.31	5.20	2.65
U238	1.30	1.72	1.85	1.96	0.92	0.87	2.19	1.78	2.12	1.63	1.71	0.99

Table A1.4 Trace element composition of Vateliero MIs

	VAT 01 melt	VAT 02A melt	VAT 02B melt	VAT 03A melt	VAT 03B melt	VAT 04 melt	VAT 05 melt	VAT 06 melt
Li7	8.68	8.60	8.93	9.67	8.72	8.70	8.12	9.15
Be9	3.15	2.63	3.59	3.78	2.75	3.81	3.31	3.81
B11	21.74	13.99	19.83	18.50	17.56	10.43	8.59	24.41
Sc45	40.58	36.16	37.68	41.17	37.85	19.88	38.91	36.00
V51	290.37	291.32	276.80	286.79	258.37	264.35	185.01	226.59
Cr53	155.75	283.88	271.52	130.12	156.58	3.29	125.49	213.04
Co59	36.31	35.16	36.82	40.26	42.91	45.36	33.98	39.46
Ni60	190.40	220.73	261.37	233.75	257.22	29.11	162.27	238.76
Cu63	90.61	83.24	81.81	84.06	78.59	16.85	86.56	63.66
Zn66	78.59	52.69	63.63	65.57	63.86	68.10	56.96	61.13
Rb85	137.04	121.32	119.26	146.88	134.03	101.53	46.62	167.59
Sr88	910.09	661.69	619.44	891.70	832.83	1251.35	868.21	688.24
Y89	23.79	22.50	22.51	24.20	21.89	22.84	24.77	19.20
Zr90	121.03	106.48	102.93	140.60	110.82	196.18	155.62	118.23
Nb93	17.31	16.45	15.15	19.42	16.98	20.55	13.04	16.64
Cs133	8.12	9.73	9.53	8.99	7.83	3.95	1.85	11.42
Ba137	1279.18	1082.31	1054.41	1342.15	1281.65	932.71	441.04	1373.72
La139	38.62	23.11	21.24	38.11	35.96	36.33	21.33	26.72
Ce140	84.26	47.05	48.28	82.51	81.33	88.42	53.53	62.81
Pr141	10.08	6.07	5.97	9.73	9.28	11.95	7.55	7.56
Nd146	41.06	27.24	26.43	40.53	37.77	52.04	35.53	31.49
Sm147	8.47	6.23	6.12	8.42	7.68	10.17	8.38	6.86
Eu153	2.42	1.81	1.83	2.17	2.13	2.56	2.25	1.82
Gd157	6.94	5.94	5.99	7.51	6.47	7.44	6.45	5.79
Tb159	0.88	0.75	0.78	0.97	0.86	0.85	0.84	0.74
Dy163	5.09	4.51	4.73	5.01	4.45	5.08	4.85	3.97
Ho165	0.91	0.90	0.88	0.97	0.80	0.89	0.93	0.76
Er166	2.28	2.39	2.41	2.30	2.10	2.42	2.46	1.95
Tm169	0.32	0.33	0.31	0.32	0.28	0.29	0.34	0.25
Yb172	2.22	2.08	2.03	2.15	1.81	2.02	2.28	1.86

Lu175	0.31	0.30	0.28	0.30	0.28	0.25	0.37	0.27
Hf178	3.08	2.71	2.69	3.62	2.82	5.12	3.65	3.01
Ta181	0.88	0.75	0.70	1.01	0.78	1.21	0.78	0.91
Pb206	28.34	20.15	20.40	27.24	25.10	12.60	6.99	26.30
Pb207	25.38	18.06	18.52	24.63	22.66	10.88	6.13	23.49
Pb208	26.90	19.96	18.74	25.32	24.54	11.43	6.71	24.80
Th232	9.01	7.86	7.89	10.03	8.56	5.68	2.91	8.26
U238	2.66	2.62	2.63	2.84	2.74	1.76	0.96	2.81
	VAT 07A melt	VAT 07B melt	VAT 08 melt	VAT 09 melt	VAT 10 melt	VAT 11 melt	VAT 12 melt	VAT 13 melt
Li7	10.15	8.72	9.50	6.89	7.52	10.34	7.96	7.77
Be9	3.10	3.37	3.27	2.85	3.53	2.37	4.58	2.24
B11	16.36	15.15	7.76	16.33	7.69	9.78	19.87	14.16
Sc45	23.93	21.74	43.11	37.07	21.50	33.82	37.95	28.36
V51	398.23	318.80	232.10	276.98	186.55	200.61	291.63	352.97
Cr53	2.26	6.25	137.70	53.56	7.96	92.23	176.25	68.24
Co59	47.96	40.46	40.42	39.37	41.39	41.67	38.92	53.53
Ni60	70.75	55.43	173.63	137.69	78.27	171.14	209.99	130.93
Cu63	20.72	30.08	91.71	156.02	42.43	96.64	74.32	104.52
Zn66	80.58	76.78	62.60	60.59	65.02	56.53	59.41	74.32
Rb85	179.36	158.25	58.72	134.57	120.47	106.52	140.91	116.30
Sr88	1011.97	955.42	702.99	922.97	716.91	527.46	623.41	917.12
Y89	32.55	31.38	23.69	23.67	26.37	20.61	21.31	21.51
Zr90	141.67	136.18	109.30	113.25	149.60	109.97	106.53	102.13
Nb93	24.28	22.80	12.65	17.67	22.80	24.27	15.99	16.79
Cs133	9.03	7.83	2.48	8.69	5.05	4.49	10.91	7.85
Ba137	1839.37	1650.10	530.06	1324.10	1155.60	809.49	1140.17	1044.53
La139	57.53	49.20	20.98	31.42	37.24	31.40	21.77	24.92
Ce140	125.79	109.67	48.27	67.70	81.87	64.31	48.75	58.67
Pr141	14.78	12.72	5.82	8.64	9.55	7.43	6.22	7.16
Nd146	60.42	52.89	24.10	37.29	41.40	29.24	27.19	29.99
Sm147	11.81	10.23	4.58	7.84	8.61	5.62	6.41	6.83
Eu153	3.24	2.83	1.55	2.23	2.56	1.61	1.72	1.92
Gd157	9.86	8.88	4.71	6.93	7.95	4.97	5.54	5.94
Tb159	1.20	1.16	0.70	0.85	0.94	0.67	0.76	0.76
Dy163	6.92	6.89	4.61	5.32	5.44	4.20	4.67	4.67
Ho165	1.22	1.27	0.93	0.95	1.06	0.78	0.79	0.82
Er166	3.20	3.16	2.42	2.59	2.60	2.09	2.20	2.19
Tm169	0.43	0.41	0.34	0.35	0.34	0.28	0.32	0.30
Yb172	2.91	2.73	2.23	2.20	2.20	1.96	2.08	2.11
Lu175	0.40	0.35	0.33	0.32	0.29	0.26	0.27	0.28
Hf178	3.40	3.43	2.70	2.80	3.45	2.56	2.74	2.75
Ta181	1.30	1.18	0.73	0.94	1.28	1.34	0.80	0.83
Pb206	17.28	20.07	8.40	21.67	13.34	12.37	21.83	18.54
Pb207	15.00	17.64	7.69	19.73	12.47	11.17	19.90	16.97
Pb208	16.20	18.82	7.90	21.15	12.59	11.94	20.63	18.11
Th232	10.29	10.26	3.39	8.15	6.92	6.63	8.09	6.65
U238	3.17	2.89	1.03	2.66	2.01	1.97	2.69	2.24

	VAT 14 melt	VAT 15A melt	VAT 15B melt	VAT 16A melt	VAT 16B melt	VAT 17 melt	VAT 18 melt	VAT 19 melt	VAT 21 melt
Li7	8.45	10.64	11.51	9.72	8.51	8.86	9.21	9.04	9.26
Be9	2.68	3.41	3.03	2.83	3.85	3.54	3.76	2.13	3.04
B11	17.46	16.39	17.20	6.89	18.33	17.69	19.61	18.96	17.25
Sc45	31.54	23.84	24.04	30.01	40.69	34.84	41.85	28.35	31.97
V51	261.11	330.75	311.00	155.73	281.82	279.65	314.29	204.74	285.26
Cr53	102.36	17.24	14.72	41.64	68.11	34.18	115.23	33.46	58.16
Co59	40.27	48.74	48.91	38.11	51.28	50.77	38.94	35.66	37.73
Ni60	151.29	78.08	85.54	138.81	223.04	200.24	175.43	150.26	99.84
Cu63	115.23	38.81	44.44	67.32	124.17	123.21	95.19	102.26	74.89
Zn66	67.51	84.76	89.88	60.27	68.98	70.94	69.37	51.84	72.28
Rb85	133.98	148.17	140.38	59.47	120.85	127.05	150.18	160.15	149.33
Sr88	946.26	1082.79	1094.70	526.27	770.91	856.56	917.56	880.30	1017.73
Y89	23.59	28.49	29.35	17.95	23.71	22.90	24.09	21.60	24.15
Zr90	122.27	136.55	134.10	119.79	104.58	109.47	124.08	140.37	130.77
Nb93	18.11	21.50	21.66	13.28	14.32	15.67	16.97	22.37	20.68
Cs133	7.86	8.29	7.68	2.75	9.42	9.21	10.00	8.13	8.76
Ba137	1312.81	1533.57	1551.79	497.65	1085.86	1155.17	1378.48	1150.84	1357.82
La139	40.45	43.79	46.40	19.44	22.47	24.59	31.98	35.82	40.34
Ce140	86.48	96.71	105.32	46.38	52.48	55.41	73.98	75.01	91.27
Pr141	10.34	11.58	12.20	5.69	6.63	7.08	9.04	8.87	10.47
Nd146	41.72	47.26	50.59	25.37	29.37	32.23	37.75	35.29	41.50
Sm147	8.70	9.88	10.21	5.34	6.53	7.19	7.90	6.83	8.41
Eu153	2.33	2.60	2.57	1.76	1.80	1.97	2.36	1.97	2.23
Gd157	7.52	8.59	8.65	4.51	6.19	6.78	7.25	5.88	7.17
Tb159	0.93	1.05	1.09	0.61	0.82	0.83	0.89	0.73	0.86
Dy163	4.89	5.71	6.88	3.44	5.19	4.93	5.07	4.43	5.06
Ho165	0.95	1.08	1.12	0.67	0.81	0.88	0.96	0.81	0.91
Er166	2.46	2.93	3.11	1.89	2.43	2.27	2.35	2.23	2.42
Tm169	0.32	0.38	0.42	0.26	0.33	0.33	0.32	0.32	0.33
Yb172	2.19	2.56	2.62	1.93	1.82	2.12	2.30	2.13	2.24
Lu175	0.31	0.38	0.34	0.30	0.33	0.28	0.33	0.31	0.29
Hf178	3.13	3.28	3.37	2.86	2.43	3.15	3.45	3.52	3.28
Ta181	0.93	1.16	1.14	0.76	0.61	0.80	0.87	1.19	0.93
Pb206	23.75	22.02	23.91	7.17	20.49	21.04	25.46	18.21	22.64
Pb207	21.28	19.68	21.79	6.48	17.20	18.77	23.88	17.30	21.02
Pb208	22.17	20.83	23.80	6.98	17.89	19.42	24.43	17.73	22.19
Th232	9.29	10.06	9.71	3.46	7.94	7.82	8.94	9.16	9.45
U238	2.76	2.90	2.96	1.15	2.31	2.45	2.97	2.73	3.05

A2 Correction for post-entrapment crystallization.

Silicate MIs are small drops of silicate melt which are entrapped within growing crystals in the depth of the magmatic system.

After trapping, the MIs cooling leads to the crystallization of a variable amount of the melt itself, which produce an olivine rim on the walls of the inclusion. This post-

entrapment crystallization depletes the residual melt in MgO and progressively in FeO, due to the evolution of the entrapped melt while the olivine rim growth. That result in a compositional gradient of the MIs crystallized rim. This evolution gradient is the causes of the "Fe loss" described in chapter 5.3.

In order to consider MIs as the best representative of the depth magma, it is needed to reconstructing the initially trapped MIs composition, through algorithms that simulate the Fe and Mg exchange between the entrapped melt and the olivine, which occur during the equilibration processes.

The method used in this study to reconstructing the pristine chemical composition of MIs is based on the assumption of the equilibrium between the host olivine and the MIs. It consists of a reverse binary mixing, using the first known end-member, which is the olivine, to find the second end-member (the pristine melt). The procedure is adding the olivine to the melt until the equilibrium composition is reached. The equilibrium is defined from the Mg-Fe exchange coefficient, $KD[(FeO/MgO)_{Oliv}/(FeO/MgO)_{melt}] = 0.26$ [Di Carlo et al., 2006].

The quantified post-entrapment crystallization (%) for each FS and Vateliero sample is reported in Table A2.1.

Table A2.1 Computed post-entrapment crystallization (%) for each sample of this study.

melt ID	cristall. (%)	melt ID	cristall. (%)
VAT 01	10	FS 01	14
VAT 02A	11	FS 02	7
VAT 02B	11	FS 03	14
VAT 03A	10	FS 04	7
VAT 03B	12	FS 05	6
VAT 04	4	FS 06	9
VAT 05	11	FS 08	3
VAT 06	11	FS 11	13
VAT 07A	3	FS 12	14
VAT 07B	6	FS 13	7
VAT 08	8	FS 14	6
VAT 09	9	FS 16	10
VAT 10	5	FS 17	13
VAT 11	10	FS 18	9
VAT 12	12	FS 19	7
VAT 13	10	FS 22	9
VAT 14A	6	FS 24	13
VAT 15A	6	FS 25	14
VAT 15B	6	FS 26	4
VAT 16A	9	FS 28	4
VAT 16B	12		
VAT 17	8		
VAT 18	11		
VAT 19	10		
VAT 21	9		

A3 Fractional crystallization and partial melting models

To assume Ba/La ratio as indicative of fluid contamination it should depend only on fluid input. In order to check this assumption, it is needed to understand if magmatic processes can modify this ratio. The two investigated processes are the fractional crystallization of the melt and the partial melting of the mantle source.

Fractional crystallization, which assumes only instantaneous equilibrium between solid and liquid, is a more generally applicable model of crystallization. Crystallization is described by the following equation:

Eq. A1

$$\frac{C_i^l}{C_i^0} = (1 - X)^{(D_{s/l}-1)}$$

Where *i* is the element of interest, X is the crystallized fraction, C^l is the starting concentration in the remaining liquid, C^0 is the concentration in the original liquid, and $D_i^{s/l}$ il the partitioning coefficient of the *i*-element between solid and liquid phase. Used $D_i^{s/l}$ for trace elements are reported in Viccaro et al., 2007, and Viccaro and Cristofolini, 2008.

The re-arranged equation allows us to calculate the concentration of trace elements at different F. Computed crystallization model shows the effect of different crystallization degree on trace element ratio (Fig. A1). Ba/La ratio variation within our Etna and Vateliero samples are bigger than variation given by high crystallization fractions. It allowing us to exclude the effect of crystallization on Ba/La.

Fig. A1. Modelled crystallization curves of La/Sm and Ba/La ratio. It shows that Ba/La is not dependant from crystallization.

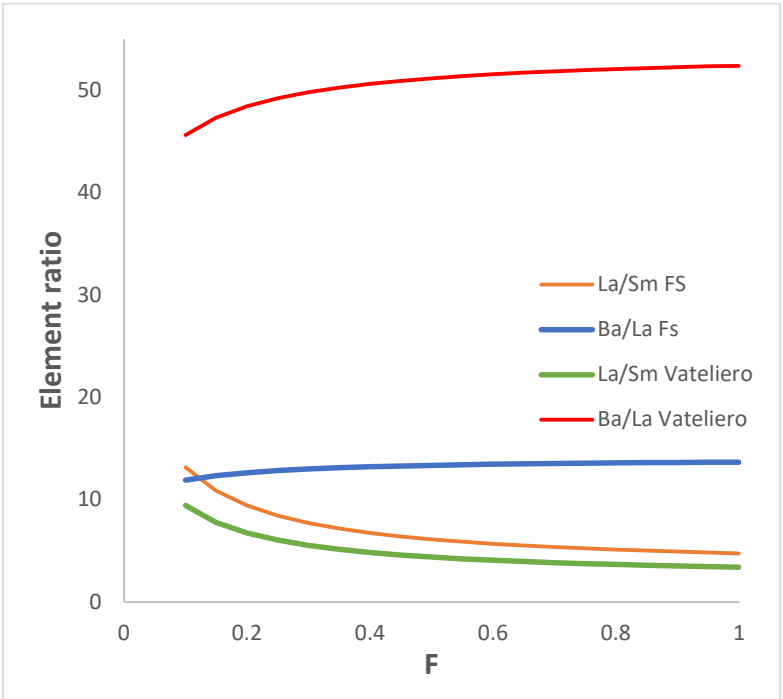

Different degree of the source peridotite partial melting can partition trace elements such as fractional crystallization.

In the hypothesis that the entire batch equilibrates with the residue before it is removed, we used the mass balance:

Eq. A2

$$C_i^0 = C_i^s \cdot (1 - F) + C_i^l \cdot F$$

Where *i* is the element of interest, F is the melt fraction, C^0 is the concentration in the original solid whole phase, C^s is the concentration in remaining solid, and C^l is the concentration in the produced liquid. Since $D^{s/l} = C^s/C^l$ the equation can be rearranged:

Eq. A3

$$C_i^0 = C_i^l \cdot D_i^{s/l} \cdot (1 - F) + C_i^l \cdot F$$

$D_i^{s/l}$ il the partitioning coefficient of the *i*-element between solid and liquid phase. $D_i^{s/l}$ for batch partial melting was computed for Ba, La and Rb. Partition coefficients were calculated using $D^{mineral/melt}$ listed in Geochemistry, William M. White, 2013. Table7.5, and the modal mineral composition of studied products.

Used C^0_s element concentration for partial melting were attributed in order to obtain the elemental starting Ba/La and La/Sm ratios of our samples with the fewest degree of partial melting.